Modulation of Signaling and Intracellular Trafficking Pathways by Surface-Engineered Hydrogel Nanoparticles in Tumor Cells

by

Leshern Karamchand

A dissertation submitted in partial fulfillment
of the requirements for the degree of
Doctor of Philosophy
(Chemical Biology)
in the University of Michigan
2014

Doctoral Committee:

Professor Raoul Kopelman, Chair
Professor Ari Gafni
Professor George A. Garcia
Professor Gary D. Glick

Stand up, be bold, be strong.
Take the whole responsibility on your own shoulders,
and know that you are the creator of your own destiny.

‘It is the coward and the fool who says,
“This is fate” ‘—so says the Sanskrit proverb.
But it is the strong man who stands up and says,
‘I will make my fate’.

Strength is life;
weakness is death.
Strength is felicity, life eternal, immortal;
weakness is constant strain and misery;
weakness is death.

Anything that makes you weak
Physically, intellectually, and spiritually,
Reject as poison;
There is no life in it, it cannot be true.
Truth is strengthening.
Truth is purity,
Truth is all knowledge.

~ Swami Vivekananda

For my beloved parents, Rajendra and Sandhya,
and brother, Sumanth, who have always given me
their unconditional love, encouragement and support.

Acknowledgements

First and foremost, I am sincerely grateful to my advisor, Professor Raoul Kopelman, who accepted me into his lab without reservation. I could not have asked for a better advisor than Professor Kopelman, who was always enthusiastic to listen to, and support the research ideas that I had developed during the course of my doctoral studies. I am most grateful to Professor Kopelman for having confidence in me, and affording me the freedom, especially during the last year of my research, to steer my thesis project in the direction that I believed was both intriguing and exciting. I have indeed developed immensely as a scientist under his mentorship. Also, I am particularly thankful for the patience that Professor Kopelman has had with me during the numerous times I have experienced debilitating setbacks with my health.

I would like to thank my thesis committee composed of Professor Ari Gafni, Professor George Garcia and Professor Gary Glick for their insightful advice and constructive criticisms, which have helped me to stay on track during the course of my doctoral research, and reach this important milestone in my career.

I am especially grateful to the senior members of the Kopelman Group with whom I've worked closely during the first half of my tenure as a graduate student. I would like to thank Dr. Yong-Eun Koo Lee for her mentorship, and her ever willingness to discuss research ideas, proofread my manuscripts and research proposals, and even assist in troubleshooting problems with experiments. I would also like to express my sincere appreciation to Dr. Gwangseong Kim, Dr. Hoe Jin Hah, and Dr. Shouyan Wang who trained me in the core techniques of cell culture, nanoparticle synthesis and confocal microscopy, which have proved indispensable to me for my doctoral research.

I would also like to thank my fellow graduate students who have worked alongside me in the lab, and helped create a positive and friendly environment that was conducive to carrying out

research. They include Teppei Shirakura, Rémy Elbez, Dr. Ming Qin, Dr. Hyung Ki Yoon, Dr. Taeyjuana Curry, Dr. Kristen Simmer, Dr. Ariel Hecht, and Dr. Aniruddha Ray.

I am sincerely grateful to Dr. Aniruddha Ray who has been both a dear friend and brother to me during my time here in Ann Arbor. He has always been a great pillar of support to me during the numerous, difficult times I have experienced with my health over the course of my graduate studies. I am also thankful to Ananya Mukundan for the times she had willingly assisted me with my cell signaling experiments, despite the demands of her undergraduate coursework.

I am also appreciative of the Philbert Lab in the School of Public Health for allowing me to use their confocal microscopy facilities. I would also like to express my gratitude to Dr. Andrea Stoddard and Carol Ann Pitcairn of the Fierke Lab for assisting me with the autoradiography aspect of my cell signaling research. I would not have been able to acquire my crucial phosphoproteomic data without their generous time and assistance.

I would like to acknowledge my sincere appreciation to Dr. Kathleen Nolta for her superb mentorship during the four semesters I worked with her as a Chemistry teaching assistant. It has been both a pleasure and a privilege to work with, and learn from her. Dr. Nolta was also greatly helpful in providing constructive feedback on my nanoparticle intracellular trafficking manuscript, for which I am immensely grateful.

I am immensely appreciative of the administrative support that Laura Howe, the Chemical Biology Doctoral Program Manager, has given me since I first arrived in Ann Arbor. Laura was also influential in arranging a research fellowship for me during my final winter semester such that I would not have to teach during that time, and could therefore concentrate on completing my final experiments in preparation to defend my thesis.

I am sincerely grateful to Mrs. Lakshmi Akella, and my friends Dr. Saurabh Gupta, Dr. Prasanna Amur Varadarajan, Dr. Biju Edamana, and Mahesh Ganesan who helped my get settled in upon my first arrival in Ann Arbor. They were incredible pillars of support during a particularly tumultuous period I experienced in acclimatizing to the new environment in Ann Arbor.

I would also like to express my sincere gratitude to the Fulbright International Science and Technology Program, firstly for granting me the incredible opportunity to pursue my PhD in the USA, and secondly for generously funding the first three years of my doctoral studies at the University of Michigan.

In addition, I acknowledge the generous financial assistance granted to me by the South African National Research Foundation (NRF) in the form of the NRF Free-Standing Doctoral Scholarship for Study Abroad.

Last but not least, I cannot adequately express the immense love and gratitude that I have for my parents and brother, who have unconditionally supported me, from afar, over these past 5 years of my doctoral studies. They have raised me up whenever I felt as though I could not go on any further. They are, without doubt, the wind beneath my wings.

I am also grateful to my aunts, Pranitha and Amashnee, and my nani for having always kept me in their thoughts and prayers during all these years that I've been away from home.

Above all else, I am eternally grateful to the Divine Mother for her divine love and guidance. It is only through Her divine will that I have been able to accomplish my Doctorate despite all the trials and tribulations that I have endured over the last 5 years.

Table of Contents

List of Figures

List of Tables

Abstract

Surface engineering of a polyacrylamide (PAA) hydrogel nanoparticle (NP) with the tumor-targeting ligand, F3 peptide (KDEPQRRSARLSAKPAPPKPEPKPKKAPAKKC), confers binding specificity toward Nucleolin overexpressing tumor cells (9L rat gliosarcoma, and MDA-MB-435 human breast adenocarcinoma). In this study, the endocytic internalization, and intracellular trafficking of the non-targeted PAA-NPs (NTNPs), and F3-targeted PAA-NPs (F3NPs) in the above-mentioned cell lines, was investigated. Caveolae-mediated internalization of both types of PAA-NPs peaked at 2 hours post-delivery, although internalization of the NTNPs was ~2-fold greater than for the F3NPs. In contrast, clathrin-mediated internalization of both types of PAA-NPs was markedly faster; the NTNPs and F3NPs both reached similar peak colocalization levels with early endosome antigen-1 (EEA1, ~32%) at 30 minutes post-delivery. However, at 60 minutes post-delivery, the NTNPs exhibited faster egress from the early endosomes than the F3NPs, with a concomitant, sharp increase in trafficking to the lysosomes (acidic, degradative vesicles), whereas the F3NPs largely evaded trafficking to the lysosomes. Furthermore, the F3 peptides alone exhibited significantly higher accumulation within the lysosomes than both the NTNPs, and the F3NPs.

The p38 Mitogen-Activated Protein Kinases (MAPKs), upon activation, promote (i) internalization of caveolae from the cell membrane, and (ii) rapid trafficking of early endosomes to the lysosomes by directly phosphorylating Caveolin1 and EEA1, respectively. Phospho-

proteomic analyses, in MDA-MB-435 cells, revealed that the peak levels of activated p38β and p38δ MAPKs (at 2 hours post-delivery) elicited by the F3 peptides alone, and the NTNPs was 1.5 – 2-fold greater than by the F3NPs. These data therefore provide compelling evidence that the intracellular trafficking behavior of the F3 peptides, NTNPs and F3NPs are attributable to their differential activation of the p38 MAPKs. Further analysis of the ERK MAPK, JNK MAPK, and Akt pathways revealed that the NTNPs elicit a pro-apoptotic signaling profile, whereas the F3 peptides, and F3NPs elicit proliferative profiles. The findings of this thesis suggest that the design of tumor-targeting nanoparticles also need to consider the MAPK signaling profiles that they elicit on the intended target cell type, due to the influence of the p38 MAPKs, in particular, on endocytic trafficking, and the survival status of the target tumor cell.

Chapter 1: Literature Review

1.1 Introduction

The earliest documented treatment of cancer dates as far back as 3000BC to the ancient Egyptian civilization. The Greek physician, Hippocrates (460-370BC), is accredited with the first scientific description of cancer, whereby he used the terms *carcinos* and *carcinoma* to describe non-ulcerating and ulcerating cancers, respectively. These words refer to a crab, which were likely attributed to the disease due to the finger-like projections that emanate from a cancer, thus evoking the shape of a crab. The recognition of cancer as a *cell-based disease* paved the way for our understanding of cancers at a physiological, genetic and molecular basis, and concomitantly transformed our approaches to its treatment. Whilst tumors originate from apparently normal parental cells, cancer cells clearly evolve unique phenotypic characteristics. As such, cancer tissues are best conceptualized as a collection of traits or hallmarks, such as invasion of normal tissue, immune evasion, autonomous and unrestricted growth, resistance to apoptosis, and deregulated cellular energetics.[1]

Until 30 years ago however, cancer chemotherapies were restricted to cytotoxic drugs that indiscriminately killed rapidly dividing normal and cancer cells. Only in recent decades, has there been a shift away from the 'cytotoxic approach' toward a 'targeted molecular approach' that specifically exploits the unique traits of cancer cells so as to selectively kill them.[2] The advent of nanoparticles (inorganic or organic materials typically ranging from tens to few

hundreds of nanometers (10^{-9} m) in size) has provided versatile multifunctional nanoplatforms[3] upon which various modalities, such as, tumor targeting moieties, synergistic drugs to overcome multiple drug resistance (MDR) transporters, and enzymes that degrade the extracellular matrix, can be integrated in a single package to enhance drug accumulation within the tumor site, while minimizing side effects. Furthermore, nanoparticles (NPs) have a distinct advantage over chemotherapeutic drugs in being able to accumulate within the tumor interstitium.[4] This is largely due to the "physiological barrier" of the tumor that prohibits the diffusion of drug molecules into the tumor interstitium. In particular, the disorganized vascular architecture of solid tumors (discussed further) presents a significant challenge to the ability of chemotherapeutic drugs to infiltrate the tumor tissue from the circulation, which can severely limit the effective amount of drug that accumulates within the tumor. As Sun Tzu expounded in his famous book, *The Art of War*, the key to winning battles lies in the knowledge of one's enemy and oneself. Hence, the development of effective drug-delivery strategies is critically dependent on an understanding of the tumor pathophysiology, and the ability to tailor the drug-delivery system accordingly.

1.2 Pathophysiology of Solid Tumor Vasculature

As normal tissues proliferate and become established, their nascent vasculature is organized into a highly structured and hierarchical network of arterioles, capillaries, venules and lymphatic vessels that function cooperatively to maintain optimal tissue perfusion. By contrast, the physiology of tumors is markedly different to that of normal tissues, in that, it is characterized by hypoxia (oxygen depletion), acidosis and high lactate levels within the extracellular compartment, glucose and energy deprivation, increased interstitial fluid flow, and interstitial hypertension.[5]

This harsh tumor microenvironment is essentially attributed to rapid, unregulated tumor vasculature proliferation that results in immature, structurally and functionally defective microvessels. Due to the highly dysfunctional and defective nature of the tumor vasculature, it has deservedly been described as an "aberrant monster".[6] Briefly, the tumor vasculature is characterized by (i) loss of vessel hierarchy, (ii) excessive and disorganized vessel branching accompanied by sinusoidal (blind) endings, (iii) incomplete, or even absent endothelial cell linings of vasculature, and interrupted basement membranes, (iv) presence of tumor-cell lined vasculature, (v) increased vascular permeability due to enlarged fenestrations (spaces between endothelial cells), and (vi) compressed lymphatic vessels with lumens that are commonly infiltrated by tumor cells.[5] The enlarged vascular fenestrations promote the extravasation of blood plasma, as well as, red blood cells into the tumor interstitium (extracellular space). In normal tissue, the ratio of *Intracellular volume: Interstitial volume: Intravascular volume* is maintained at ~ 0.73: *0.16*: 0.11, whereas in tumor tissue, the interstitial volume is markedly enlarged, thus yielding a ratio of ~ 0.50: *0.45*: 0.05.[5] Subsequently, equilibrium between the hydrostatic and oncotic pressures with the tumor microvasculature, and the tumor interstitial fluid pressure is achieved. This, in conjunction with poor lymphatic drainage of the tumor center,[7] results in a dramatic increase in hydrostatic pressure of the tumor interstitium (interstitial hypertension). The interstitial fluid pressure in normal tissue ranges between slightly sub-atmospheric ("negative"), to just above atmospheric pressure (-3 to 6 mmHg),[8] whereas the interstitial hypertension in tumors reach up to 60-70 mmHg.[9] As such, the overwhelming interstitial fluid pressure of tumors presents a "physiological barrier" to the delivery of therapeutic molecules to the cancer cells, by prohibiting their diffusion into the tumor interstitium from the tumor vasculature.[10] In addition, the poor perfusion of tumor vasculature

further limits the delivery of chemotherapeutic drugs to the tumor interstitium.[11]

1.3 Passive Tumor Targeting of Nanoparticles

Nanoparticles are however, able to accumulate within the tumor interstitium by an effect known as, "enhanced permeability and retention (EPR)", which is exclusive to solid tumors.[12] The "enhanced permeability" of NPs into the tumor interstitium is attributed to the abnormally large fenestrations of the tumor vasculature,[13] while the "enhanced retention" of NPs within the tumor interstitium is due to the compressed lymphatic vessels[14] that prohibit the tumor from clearing away the nanoparticles that enter it. Following administration into the peripheral bloodstream, the NPs distribute indiscriminately throughout the systemic circulation, and over time, a fraction of the administered dose will accumulate within the tumor site by the EPR effect. This is known as *passive tumor targeting*. The reason for a fraction of the administered nanoparticle dose reaching the tumor site is as follows. Upon contact with the blood stream, NPs acquire a corona consisting of serum proteins, adsorbed to their surface, which is known as opsonization. Furthermore, the composition of the protein corona is dependent on the size and surface charge of the NP.[15] The opsonized NPs are then recognized, and subsequently removed from the circulation by phagocytic macrophages located in the liver and spleen that comprise the mononuclear phagocytic system (MPS).[16] The surface-modification of NPs with the polyethylene glycol (PEG; a biocompatible, neutral-charged, hydrophilic, linear synthetic polymer),[17] a process known as PEGylation, confers "stealth" capability to the NPs by reducing the protein opsonization, as well as the self-aggregation of the NPs. This reduces their recognition and removal by the MPS macrophages,[18] and markedly extends their circulating lifetime, up to 40-fold longer than uncoated NPs.[19]

However, long-circulating lifetimes, and the EPR effect alone, do not guarantee efficient accumulation of the NPs within tumor site for two reasons. First, solid tumors typically grow to only a few centimeters in diameter, a small fraction of the total size of a patient.[20] Second, not all tumors exhibit the EPR effect, since the degree of vascularization and porosity of tumor vessels can vary with the type and status of the tumor.[21,4] Furthermore, metastasized colonies that have not yet established microvasculature will likely evade circulating NPs, thus also rendering the passive targeting of NPs based on the EPR effect, ineffective.

1.4 Active Targeting of Tumor Microvasculature and Vascular Zip Codes

An alternative approach is to functionalize the surface of the NP with targeting ligands (known as, *active tumor targeting*), which bind specifically to markers expressed exclusively on the luminal surface of tumor endothelial cells, but not by resting blood vessels of normal tissues (Table 1).[22] These tumor endothelial markers have been eloquently referred to as "vascular zip codes".[23] However, targeting ligands that recognize only tumor endothelial cells will accumulate within the tumor vessels, but their penetration into the tumor tissue itself still relies on passive mechanisms.[24] On the other hand, targeting ligands that recognize tumor cells solely, provide little improvement in the accumulation of the targeted NP over the non-targeted NP, as their entry into the tumor tissue still depends on the degree to which the target tumor exhibits the EPR effect. Employing targeting a ligand that targets receptors expressed by both tumor vessels and tumor cells presents is highly-advantageous, in that it combines the limited efficiency of the two above-mentioned targeting mechanisms to enhance accumulation of the targeted nanoparticle within the tumor tissue.[24] One such receptor is Nucleolin (Table 1), which is a ubiquitous nuclear and cytoplasmic protein,[25] but also *overexpressed at the cell surface* of tumor cells and tumor

endothelial cells.[26]

Table 1.1 List of cell surface expressed receptors in tumor blood vessels

Receptor
RGD-directed integrins ($\alpha v\beta 3$ and $\alpha v\beta 5$)[27,28]
Aminopeptidase N[29]
Tumor Endothelial Markers (TEMs)[30]
Endosialin[31]
Cell surface Nucleolin[26]
Cell surface Annexin-1[32]
Cell surface p32/gC1q receptor[33]
Cell surface plectin-1[34]
Fibronectin ED-B[35]
Fibrin-fibronectin complexes[36,37]
Interleukin-11 receptor α[38]
Protease-cleaved collagen IV[39,40]

1.4.1 Targeting Surface-Expressed Nucleolin Receptors

A 31-amino acid fragment (KDEPQRRSARLSAKPAPPKPEPKPKKAPAKK) of the N-terminal region of the high mobility group nucleosomal 2 (HMGN2) protein, known as F3 peptide, was shown to home to the nuclei of tumor cells and tumor endothelial cells (human HL-60 leukemia, and human MDA-MB-435 breast carcinoma) *in vivo*.[41] This effect was later attributed to the direct binding of F3 peptide to surface-expressed nucleolin receptors in MDA-MB-435 cells that mediate the internalization of the F3 peptide.[26] It was recently reported that several tumor cell lines constantly induce the expression of nucleolin receptors at their cell surface to mediate calcium-dependent ligand internalization from the extracellular environment.[42]

Furthermore, surface-expressed nucleolin has been shown to mediate the internalization of several physiological extracellular ligands. These include the carcinogenic ligands, midkine,[43] pleiotrophin,[44] and P-Selectin,[45] as well as the anti-carcinogenic ligands, lactoferrin,[46] and endostatin.[47] In addition, nucleolin has been shown to exist in cell surface complexes with the

urokinase plasminogen activator receptor (uPAR),[47] and the α5β1 integrin, whereby nucleolin physically interacts, via its C-terminal glycine-arginine-rich domain (GAR domain, 646-707 aa) with uPAR (Fig. 1.1). Furthermore, the C-terminal 212 amino acids (the fourth RNA-binding domain (RBD) and GAR domain) of *cytoplasmically-localized Nucleolin* interacts with the cytoplasmic domain of HER/ERbB receptors. Overexpression, of both nucleolin and ErbB/HER receptors leads to ErbB/HER phosphorylation, dimerization and enhanced cell proliferation (Fig. 1.1).[48,49] Importantly, the uPAR/α5β1 integrin complex has been shown to activate the ErbB1/HER1 receptor, which potentiates the mitogenic signaling of ErbB1/HER1.[50,51] Hence, nucleolin's involvement with these cell surface mitogenic receptors is to potentiate cellular proliferation. This is further supported by the observations that nucleolin-specific antagonists suppress both tumor growth and angiogenesis (development of new blood vessels).[52,53]

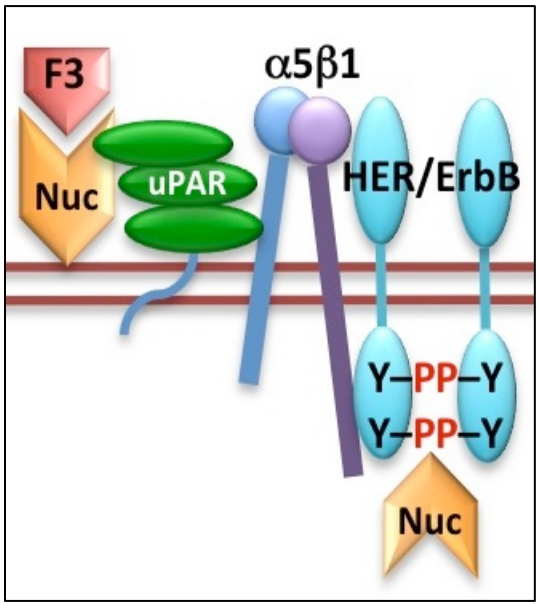

Fig 1.1 Interaction of surface-expressed and cytoplasmic nucleolin with cell surface receptors to potentiate mitogenic cell signaling. F3 (F3 peptide), Nuc (Nucleolin receptor), uPAR (urokinase plasminogen activator receptor), P-Y (phosphorylated Tyrosine residue), α5β1 (α5β1 integrin: fibronectin receptor).

Hence, the ability of nucleolin to readily internalize extracellular ligands, together with the crucial role that it plays in supporting cellular proliferation, renders it an ideal receptor target for mediating intracellular delivery of nanotherapeutics to tumor cells. Consequently, the F3 peptide has been exploited successfully for the *in vivo* delivery of various therapeutics to tumor cells that overexpress cell surface nucleolin receptors.[54–56] Also, the overexpression of nucleolin at the surface of highly proliferating, and metastatic cells, such as MDA-MB-435 breast carcinoma cells,[57] permits the targeting of NPs with nucleolin-specific ligands, such as F3 peptide, to metastatic tumor colonies that do not have established vasculature.

It is important to note at this point that, despite the use of the term "active tumor targeting" to denote the surface functionalization of nanoparticles with tumor targeting ligands, such as F3 peptide, the ligand-targeted NP does not "actively" seek out the tumor, but is still subjected to the same systemic distribution as the non-targeted NP. It is therefore advantageous to combine the surface targeting of NPs with surface PEGylation,[54] so as to enhance the circulating half-life of the NPs, and thus increase the likelihood of the NPs encountering the tumor site before their removal from the systemic circulation by the MPS macrophages. Furthermore, the large surface area of nanoparticles allows the attachment of multiple targeting ligands to the surface of a single nanoparticle, thus conferring multivalency (ability to simultaneously bind multiple receptors) and high avidity to each nanoparticle. The high avidity of multivalent, ligand-targeted NPs is usually due to an unaffected binding rate (on rate [k_{on}]), but a reduction in the dissociation rate (off rate [k_{off}]).[24] The multivalency effect is therefore especially important when functionalizing NPs with ligands, such as peptides, that bind to their targets with modest binding affinities (micromolar to low millimolar range). Enhancements in the binding affinities due to the multivalency effect are typically 10-10^4 fold.[24]

1.5 Multifunctional Hydrogel Nanoparticles in Cancer Therapy

In recent years, hydrogel nanoparticles (10-1000 nm) have received considerable attention as promising nanoparticulate drug delivery systems, which is primarily owed to their (i) hydrophilicity, (ii) extremely high water content, and (iii) their ability to swell in aqueous environments, that can be modulated by environmental changes. Hydrogels are three-dimensional polymeric networks that can be either physically, or covalently cross-linked, and can be synthesized from both natural and synthetic polymers (Table 1.2).

Table 1.2 List of natural and synthetic polymers from which hydrogel nanoparticles have been synthesized for cancer therapy applications *(adapted from Koo Lee and Kopelman)*[3]

Natural polymers	**Polysaccharides** • *Anionic:* alignate, hyaluronate, xanthene gum • *Cationic: chitosan* • *Neutral: agarose, cellulose, dextran, pullalan* **Proteins/polypeptides** • Albumin, collagen, gelatin, polylysine, elastin-like polypeptide
Synthetic polymers	• Poly(acrylic acid) • Poly(acylamide), poly(*N*-isopropylacrylamide), poly(2-hydroxyethyl methacrylate), poly[2-(*N,N*-diethylammo)ethyl methacrylate] • Poly(ethylene oxide) (PEO), poly(propylene oxide) (PPO), PEO-PPO-PEO block copolymers (or Pluronics®), poly(oligo(ethylene oxide) monomethyl ether methacrylate) • Poly(vinyl alcohol) • Poly(vinyl pyrrolidone) • Poly(*N*-vinylformamide) • Poly(ethyleneimine) • Poly(*N*-vinyl caprolactam), block copolymer of methoxy poly(ethylene glycol)-poly(caprolactone)

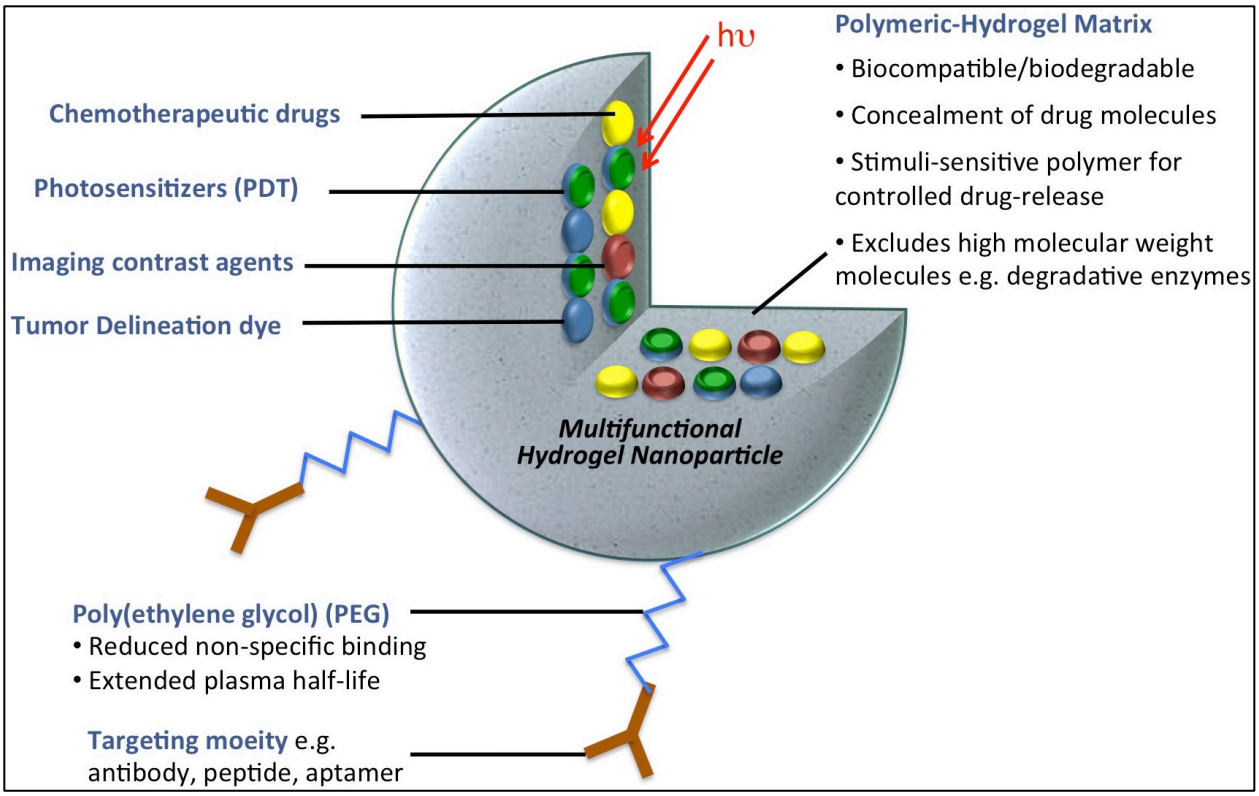

Fig 1.2 Schematic diagram of a multifunctional hydrogel nanoparticle for cancer therapy. In reality, no more than 2-3 modalities would be incorporated into each nanoplatform, in addition to the surface modifications (PEGylation and tumor ligand targeting).

Their ability to swell in water is attributed to the presence of hydrophilic groups in the polymers that form hydrogel structures.[58] Furthermore, hydrogels contain several chemical functional groups, such as amine, carboxyl, hydroxyl, and aldehyde, which can be exploited for the covalent linkage of additional molecules, such as drugs, contrast agents, PEG and targeting moieties. In addition to their ability to exploit the EPR effect, and their amenability to surface modifications (PEGylation and ligand functionalizations), hydrogel nanoparticles possess additional attractive properties that permit their application in cancer therapy. First, hydrogel NPs are biocompatible and biodegradable,[59–62] which is crucial to reducing the immunogenicity of the NP drug delivery system. Second, due to their ability to swell immensely in water, hydrogel NPs possess the capacity for high-density co-encapsulation of various types of payloads, including (i) a broad range of drugs,[63] (ii) contrast agents for biomedical imaging,[64–66] (iii)

biosensing probes,[67–69] and (iv) photosensitizers to facilitate photodynamic therapy (Fig. 1.2).[70–72] Third, hydrogel NPs can significantly enhance the intracellular accumulation of chemotherapeutic drugs by circumventing the multidrug resistance (MDR) transporter pumps (located in the cell membranes of tumor cells), which pump out chemotherapeutic drugs that diffuse across the cell membrane into tumor cells. This is achieved by the endocytosis (internalization) of the hydrogel nanoparticle and its drug payload, upon contact with the cell membrane, and its subsequent containment within the cell by an endosomal membrane. Perhaps the most attractive property of hydrogel nanoparticles, however, is the potential to engineer them for controlled-drug release in response a variety of stimuli. Depending on the type of polymer/functional moieties/crosslinkers used in the synthesis of a hydrogel nanoparticle, it can be stimulated to release its drug payload in response to either (i) a change in pH,[73] (ii) lysosomal enzymes,[74] (iii) glutathione concentration,[75,76] or (iv) temperature.[77] Furthermore, designing hydrogel nanoparticles to release their drug payload only after internalization by the tumor/endothelial cell, serves to further enhance the accumulation of drug within the target cell. The ability to incorporate such a diverse array of functionalities into a single hydrogel polymer at the nanometer level has permitted the evolution of multifunctional nanoparticles that can facilitate cancer theranostics (combination of therapy and diagnostics) (Fig. 1.2).

1.6 Endocytosis and Intracellular Trafficking of Hydrogel Nanoparticles

Upon contact with the cell membrane, both non-targeted and targeted hydrogel nanoparticles are internalized by endocytosis. The major endocytic pathways implicated in mediating the internalization of nanoparticles include, (i) clathrin-mediated endocytosis, (ii) caveolae-mediated endocytosis, and (iii) macropinocytosis (Fig. 1.3).[78] In clathrin-mediated endocytosis, the

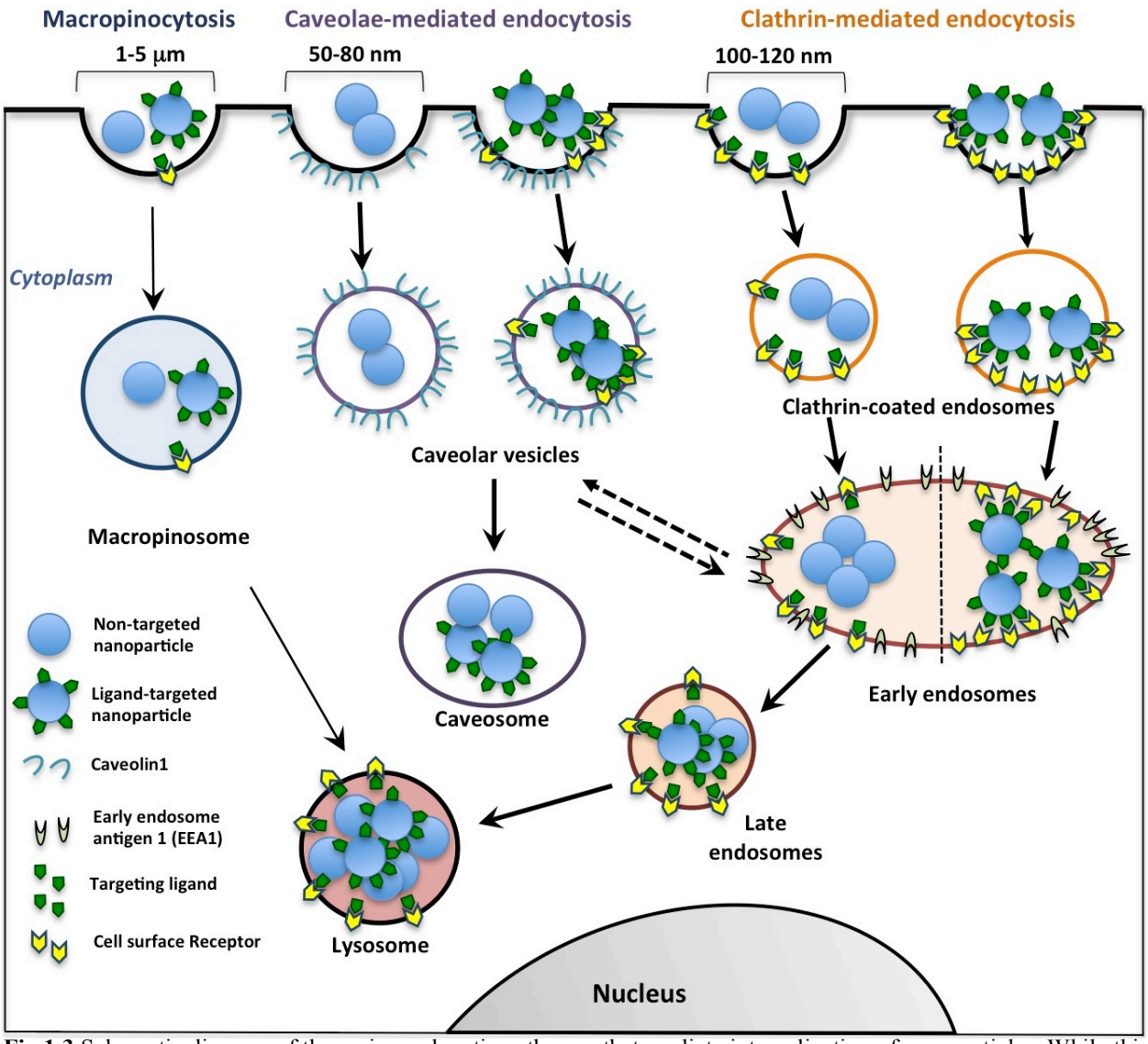

Fig 1.3 Schematic diagram of the major endocytic pathways that mediate internalization of nanoparticles. While this schematic diagram is not drawn to scale, it is important to note that the vesicles that emanate from each of these endocytic mechanisms are of different sizes.

nanoparticles are internalized via clathrin-coated pits, which form by the assembly of clathrin triskelia (three-legged protein structures) into a basket-like, polyhedral lattice on the cytoplasmic surface of the cell membrane.[79] This process deforms the cell membrane into a coated pit of ~150 nm, and formation of the clathrin lattice continues until fission of the invaginating membrane from the cell surface is achieved. Fission of the clathrin-coated vesicle requires the GTPase enzyme, dynamin, and the size of the resulting endocytic vesicle is typically 100 – 120 nm.[80,81] The NP-laden vesicle is then trafficked to the "early" (or "sorting") endosomes, which are characterized by the presence of the early endosome antigen 1 (EEA1) located in their membranes. In addition, the early endosomes are acidified by ATP-dependent proton pumps to ~ pH 6. The early endosomes then mature into late endosomes, with continued acidification of the endosomal lumen to ~pH 5. The late endosomes subsequently fuse with lysosomes (pH 4.5 - 5.5), which are the terminal, degradative subcellular compartments in this pathway (Fig. 1.3).

Caveolae are flask-shaped membrane invaginations, lined by the dimeric protein caveolin, and are characterized by a lipid content enriched in cholesterol and sphingolipids. Caveolae typically range between 50 – 80 nm in size. Upon binding to the cell membrane, NPs may be translocated to the caveolae invaginations, and maintained by receptor-ligand interactions.[80] The GTPase dynamin is also necessary for the fission of caveolae from the cell membrane however, the internalization kinetics of caveolae-mediated endocytosis are much slower than that of clathrin-mediated endocytosis.[81] The caveolae-derived vesicle then fuses with the caveosome, which is devoid of degradative enzymes, and has a pH ~7. Nonetheless, caveolae-derived vesicles have been shown to be trafficked into EEA1-postive early endosomes, and *vice versa* (Fig. 1.3).[82,83] Importantly, clathrin-mediated, and caveolae-mediated endocytosis are energy dependent processes due to their requirement for the GTPase dynamin to facilitate fission of their

respective budding vesicles from the cell membrane.

Macropinocytosis is a non-specific endocytic process that occurs independently of clathrin- and caveolae-mediated endocytosis.[84] It is driven by actin-potentiated membrane protrusions that collapse back onto and fuse with the cell membrane.[81] In the process, "large" volumes of extracellular fluid, along with suspended solutes, are internalized by the generated endocytic vesicles, which are typically 1 – 5 μm in size.[85,81] Unlike, caveolae and clathrin-coated vesicles, macropinosomes are devoid of specific coatings, and do not concentrate receptors.[86] However, macropinosomes do eventually fuse with the lysosomes.[84]

Importantly, recent studies have shown that the physicochemical properties of nanoparticles influence their internalization, namely: (i) size,[87–89] (ii) surface charge,[90–92] (iii) morphology,[93,94] and with respect to hydrogel nanoparticles specifically, (iv) elasticity of the hydrogel matrix.[95] With respect to NP surface charge, positively charged NPs exhibit a higher internalization rate than neutral, or negatively charged NPs.[96] This is attributed to the anchoring effect that the negatively charged cell membrane exerts on positively charged NPs, thus favoring endocytosis. However, negatively charged NPs also exhibit enhanced internalization with respect to neutral NPs, possibly due to their interaction with serum proteins. Accordingly, non-functionalized polyacrylamide hydrogel NPs, similar to those employed in the research reported in this thesis, were shown to acquire a corona of plasma proteins when incubated with human plasma.[97,98] The corona of surface-adsorbed proteins can, in turn, influence the cell surface receptor(s) with which a non-functionalized NP interacts, and thus its mechanism of internalization. A similar effect is also likely to occur with ligand-targeted NPs that are engineered to bind a specific cell surface receptor.

1.7 Effects of Nanoparticles on Cell Signaling

A further implication of the interaction of NPs with cell surface receptors is the activation of cell signaling pathways, particularly the kinase cascades of the mitogen activated protein kinase (MAPK) signaling system. The MAPK system consists of the (i) extracellular signal-regulated kinase (ERK) pathways, (ii) c-Jun N-terminal kinase pathway, and (iii) the p38 MAPK pathway. The ERK pathway mediates mitogenic (proliferative) signaling, whereas the JNK and p38

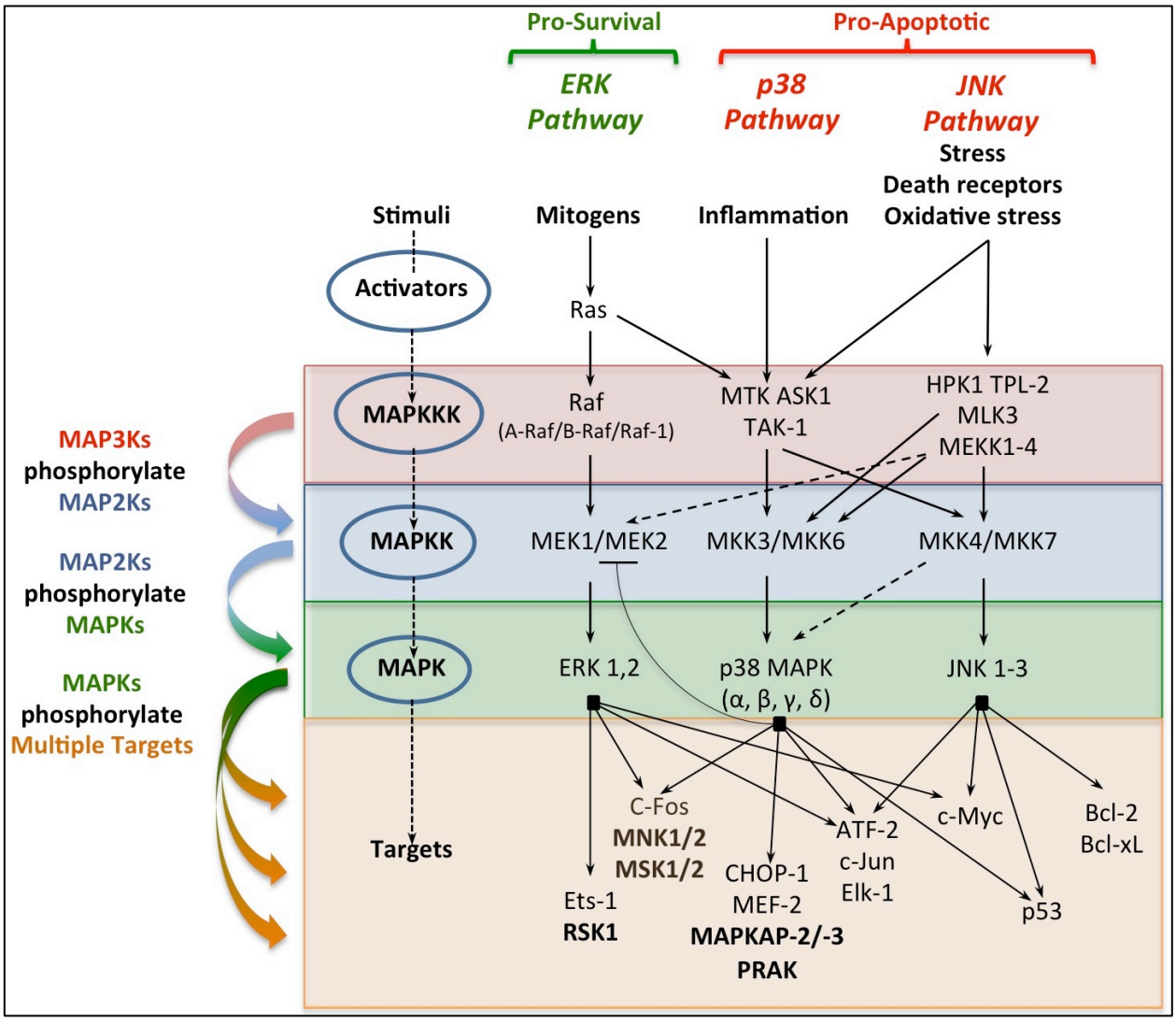

Fig 1.4 Schematic diagram depicting the ERK, JNK and p38 mitogen activated protein kinase (MAPK) signaling pathways and their integration

MAPK pathways are activated in response to stress signals, and essentially induce apoptosis (growth arrest).[99] Briefly, each pathway is activated upon phosphorylation of its respective MAP kinase kinase kinase (or MAP3K) enzymes by activation of cell surface receptors. The activated MAP3K enzymes, then phosphorylate their downstream MAP kinase kinase (or MAP2K) enzymes, which in turn mediate dual-phosphorylation of their downstream MAP kinase (or MAPK) enzymes. Fig. 1.4 illustrates the MAPK pathways that are most well characterized to date, and the downstream factors that they phosphorylate to either promote cell survival (ERK1/2), or growth arrest (JNK1-3 and p38α,β,γ,δ). Furthermore, the activated p38 MAPKs are known to enhance the rate of caveolae-mediated endocytosis, and intracellular trafficking along the clathrin-mediated pathway through direct phosphorylation of Caveolin1 at its Tyrosine-14 residue,[100] and direct phosphorylation of EEA1 at its Threonine-1392 residue.[101]

Studies have demonstrated that carbon NPs induce cell proliferation of lung epithelial cells via interaction with, and activation of the epidermal growth factor receptor (EGFR/ErbB1/HER1), and β1 integrins, which lead to activation of the ERK, as well as the Akt survival pathway.[102,103] Importantly, both the surface-associated and cytoplasmic nucleolin receptors are known to potentiate the signaling of ErbB/HER receptors and the α5β1 integrins to promote cellular proliferation (Fig. 1.1). Further studies with inorganic NPs have also reported the activation of MAPK pathways, however via the induction of reactive oxygen species.[104–106] However, to date, there are no documented studies on how non-targeted, or ligand-targeted hydrogel nanoparticles modulate the MAPK signaling pathways upon interaction with tumor cells. This represents a crucial void in the mechanistic understanding of how hydrogel nanoparticles can influence the survival status of their target cells. This urgently needs to be addressed so as develop more efficient nanoparticle drug delivery systems, since hydrogel

nanoparticles, in particular, show promising potential for targeted and controlled drug release.

1.8 Outline of the Dissertation

This dissertation documents the study into how the surface functionalization of polyacrylamide (PAA) hydrogel nanoparticles with the nucleolin-targeting F3 peptide modulates the internalization, and intracellular trafficking of PAA-NPs in tumor cells (MDA-MB-435 and 9L) that overexpress Nucleolin at their surfaces. In addition, the effects of the non-targeted PAA-NPs (NTNPs), F3-targeted PAA-NPs (F3NPs), and F3 peptide on the activation status of the MAPK (ERK, JNK and p38) and Akt signaling pathways were subsequently studied.

In Chapter 2, the surface PEGylation of the PAA-NPs was first optimized so as to reduce their potential for non-specific interaction with, and uptake by tumor cells. Subsequently, the surface functionalization of the PEGylated PAA-NPs with F3 peptides was optimized via cell-based assays (using the 9L, MDA-MB-435, and MCF7 cell lines) to achieve optimal Nucleolin-mediated internalization of the F3NPs. Based on these experiments, an F3NP-formulation that exhibited saturated cellular sequestration (binding and uptake) in both 9L and MDA-MB-435 cells was selected, and used to perform subsequent studies. Furthermore, only the 9L and MDA-MB-435 cell lines exhibited distinct correlations in cellular sequestration of the F3NPs as the F3 surface ligand density on the PAA-NPs was increased. The 9L and MDA-MB-435 cell lines were therefore selected as the optimal cell models in which to study the endocytosis and intracellular trafficking of the NTNPs and F3NPs.

In Chapter 3, the endocytic pathways responsible for mediating the internalization of the F3 peptide, NTNPs and optimized F3NPs were studied in the 9L and MDA-MB-435 cell lines, using endocytic inhibitors against the major endocytic pathways discussed earlier in Chapter 1.

Notably, the F3NPs exhibited considerably lower trafficking to the lysosomes than the NTNPs (based on colocalization with Lysotracker Red) in the MDA-MB-435 cells. The intracellular trafficking of the NTNPs and F3NPs in MDA-MB-435 cells were further dissected by immunocytochemistry. The immunocytochemistry studies revealed that while both the F3NPs and NTNPs were trafficked into early endosomes (EEA1-positive endosomes) to similar levels at 30 minutes post-delivery, the NTNPs were trafficked out of the early endosomes faster than the F3NPs, and concomitantly exhibited markedly higher colocalization with lysosome associated membrane protein 1 (LAMP1), a lysosome marker than the F3NPs. Furthermore, both the NTNPs and F3NPs exhibited peak colocalization with caveolin1 at 2 hours post-delivery, albeit the level of F3NP-caveolin1 colocalization was lower than that of the NTNP-caveolin1 colocalization.

In Chapter 4, the phosphorylation (activation) status of the p38 α,β,γ and δ MAPK isoforms, in MDA-MB-435 cells, were studied in response to treatment with the F3 peptide, NTNPs and F3NPs by ELISA, and phosphoproteomic arrays. The rationale behind these studies was that the NTNPs induce higher levels of phosphorylated (activated) p38 MAPKs than the F3NPs. Indeed, we observed that the NTNPs, as well as the F3 peptide alone, elicited significantly higher levels of phosphorylated p38β and p38δ MAPK isoforms than the F3NPs. Given that the p38 MAPKs directly phosphorylate EEA1 and caveolin1, we therefore present compelling evidence that the differential intracellular trafficking of the NTNPs and F3NPs (observed in Chapter 3) can be attributed to their differential activation of the p38 MAPKs. Furthermore, we studied the phosphorylation status of several other signaling proteins in the ERK, JNK, and Akt pathways along with key their downstream target proteins. Based on the collective analyses of these signaling phosphoproteins, the F3NPs induce a *pro-survival* signaling profile in MDA-MB-435

cells, while the NTNPs induce a *pro-apoptotic* signaling profile. We conclude this chapter by presenting plausible NP-receptor interactions to explain the observed signaling profiles elicited by the NTNPs and F3NPs.

References

1. D. M. Hockenbery, M. Tom, C. Abikoff, and D. Margineantu, ed. D. E. Johnson, Springer New York, New York, NY, 2013, pp. 35–51.
2. A. Cravo and R. Mrsny, in *Cancer Targeted Drug Delivery*, eds. Y. H. Bae, R. J. Mrsny, and K. Park, Springer New York, New York, NY, 2013, pp. 3–36.
3. Y.-E. Koo Lee and R. Kopelman, in *Multifunctional Nanoparticles for Drug Delivery Applications: Imaging, Targeting, and Delivery*, eds. S. Svenson and R. K. Prud'homme, Springer US, Boston, MA, 2012, pp. 225–255.
4. A. K. Iyer, G. Khaled, J. Fang, and H. Maeda, *Drug Discov. Today*, 2006, **11**, 812–8.
5. P. Vaupel, eds. M. Molls, P. Vaupel, C. Nieder, and M. S. Anscher, Springer Berlin Heidelberg, Berlin, Heidelberg, 2009, pp. 51–92.
6. K. Shchors and G. Evan, *Cancer Res.*, 2007, **67**, 7059–61.
7. D. Fukumura and R. K. Jain, *J. Cell. Biochem.*, 2007, **101**, 937–49.
8. A. Guyton and J. Hall, *Textbook of medical physiology*, Elsevier Inc., Philadelphia, 11th edn., 2006.
9. S. J. Lunt, T. M. Kalliomaki, A. Brown, V. X. Yang, M. Milosevic, and R. P. Hill, *BMC Cancer*, 2008, **8**, 2.
10. C.-H. Heldin, K. Rubin, K. Pietras, and A. Ostman, *Nat. Rev. Cancer*, 2004, **4**, 806–13.
11. R. K. Jain, *Annu. Rev. Biomed. Eng.*, 1999, **1**, 241–63.
12. Y. Matsumura and H. Maeda, *Cancer Res.*, 1986, **46**, 6387–92.
13. D. Fukumura, D. G. Duda, L. L. Munn, and R. K. Jain, *Microcirculation*, 2010, **17**, 206–25.
14. Y. Boucher and R. K. Jain, *Cancer Res.*, 1992, **52**, 5110–4.
15. M. Lundqvist, J. Stigler, G. Elia, I. Lynch, T. Cedervall, and K. a Dawson, *Proc. Natl. Acad. Sci. U. S. A.*, 2008, **105**, 14265–70.
16. S. M. Moghimi and H. M. Patel, *Biochim. Biophys. Acta*, 1989, **984**, 379–83.
17. A. Abuchowski, T. van Es, N. C. Palczuk, and F. F. Davis, *J. Biol. Chem.*, 1977, **252**, 3578–81.
18. S. M. Moghimi, a C. Hunter, and J. C. Murray, *Pharmacol. Rev.*, 2001, **53**, 283–318.
19. J. S. Tan, D. E. Butterfield, C. L. Voycheck, K. D. Caldwell, and J. T. Li, *Biomaterials*, 1993, **14**, 823–33.
20. C. L. Carter, C. Allen, and D. E. Henson, *Cancer*, 1989, **63**, 181–7.
21. H. Maeda, J. Wu, T. Sawa, Y. Matsumura, and K. Hori, *J. Control. Release*, 2000, **65**, 271–84.
22. E. Ruoslahti, *Nat. Rev. Cancer*, 2002, **2**, 83–90.
23. E. Ruoslahti, *Biochem. Soc. Trans.*, 2004, **32**, 397–402.

24. E. Ruoslahti, S. N. Bhatia, and M. J. Sailor, *J. Cell Biol.*, 2010, **188**, 759–68.
25. M. Srivastava and H. B. Pollard, *FASEB J.*, 1999, **13**, 1911–22.
26. S. Christian, J. Pilch, M. E. Akerman, K. Porkka, P. Laakkonen, and E. Ruoslahti, *J. Cell Biol.*, 2003, **163**, 871–8.
27. E. Ruoslahti, *Nat. Rev. Cancer*, 2002, **2**, 83–90.
28. J. S. Desgrosellier and D. A. Cheresh, *Nat. Rev. Cancer*, 2010, **10**, 9–22.
29. R. Pasqualini, E. Koivunen, R. Kain, J. Lahdenranta, M. Sakamoto, A. Stryhn, R. A. Ashmun, L. H. Shapiro, W. Arap, and E. Ruoslahti, *Cancer Res.*, 2000, **60**, 722–7.
30. E. B. Carson-Walter, D. N. Watkins, A. Nanda, B. Vogelstein, K. W. Kinzler, and B. St Croix, *Cancer Res.*, 2001, **61**, 6649–55.
31. S. Christian, H. Ahorn, A. Koehler, F. Eisenhaber, H. P. Rodi, P. Garin-Chesa, J. E. Park, W. J. Rettig, and M. C. Lenter, *J. Biol. Chem.*, 2001, **276**, 7408–14.
32. P. Oh, Y. Li, J. Yu, E. Durr, K. M. Krasinska, L. A. Carver, J. E. Testa, and J. E. Schnitzer, *Nature*, 2004, **429**, 629–35.
33. V. Fogal, L. Zhang, S. Krajewski, and E. Ruoslahti, *Cancer Res.*, 2008, **68**, 7210–8.
34. K. A. Kelly, N. Bardeesy, R. Anbazhagan, S. Gurumurthy, J. Berger, H. Alencar, R. A. Depinho, U. Mahmood, and R. Weissleder, *PLoS Med.*, 2008, **5**, e85.
35. F. Nilsson, H. Kosmehl, L. Zardi, and D. Neri, *Cancer Res.*, 2001, **61**, 711–6.
36. J. Pilch, D. M. Brown, M. Komatsu, T. A. H. Järvinen, M. Yang, D. Peters, R. M. Hoffman, and E. Ruoslahti, *Proc. Natl. Acad. Sci. U. S. A.*, 2006, **103**, 2800–4.
37. D. Simberg, T. Duza, J. H. Park, M. Essler, J. Pilch, L. Zhang, A. M. Derfus, M. Yang, R. M. Hoffman, S. Bhatia, M. J. Sailor, and E. Ruoslahti, *Proc. Natl. Acad. Sci. U. S. A.*, 2007, **104**, 932–6.
38. V. O. Lewis, M. G. Ozawa, M. T. Deavers, G. Wang, T. Shintani, W. Arap, and R. Pasqualini, *Cancer Res.*, 2009, **69**, 1995–9.
39. J. Xu, D. Rodriguez, E. Petitclerc, J. J. Kim, M. Hangai, Y. S. Moon, G. E. Davis, P. C. Brooks, and S. M. Yuen, *J. Cell Biol.*, 2001, **154**, 1069–79.
40. J. Mueller, F. C. Gaertner, B. Blechert, K.-P. Janssen, and M. Essler, *Mol. Cancer Res.*, 2009, **7**, 1078–85.
41. K. Porkka, P. Laakkonen, J. A. Hoffman, M. Bernasconi, and E. Ruoslahti, *Proc. Natl. Acad. Sci. U. S. A.*, 2002, **99**, 7444–9.
42. A. G. Hovanessian, C. Soundaramourty, D. El Khoury, I. Nondier, J. Svab, and B. Krust, *PLoS One*, 2010, **5**, e15787.
43. E. a Said, B. Krust, S. Nisole, J. Svab, J.-P. Briand, and A. G. Hovanessian, *J. Biol. Chem.*, 2002, **277**, 37492–502.
44. E. a Said, J. Courty, J. Svab, J. Delbé, B. Krust, and A. G. Hovanessian, *FEBS J.*, 2005, **272**, 4646–59.
45. E. M. Reyes-Reyes and S. K. Akiyama, *Exp. Cell Res.*, 2008, **314**, 2212–23.
46. D. Legrand, K. Vigie, E. a. Said, E. Elass, M. Masson, M.-C. Slomianny, M. Carpentier, J.-P. Briand, J. Mazurier, and A. G. Hovanessian, *Eur. J. Biochem.*, 2004, **271**, 303–317.
47. N. Song, Y. Ding, W. Zhuo, T. He, Z. Fu, Y. Chen, X. Song, Y. Fu, and Y. Luo, *Angiogenesis*, 2012, **15**, 697–711.
48. A. Di Segni, K. Farin, and R. Pinkas-Kramarski, *PLoS One*, 2008, **3**, e2310.
49. K. Farin, A. Di Segni, A. Mor, and R. Pinkas-Kramarski, *PLoS One*, 2009, **4**, e6128.
50. J. A. Aguirre Ghiso, D. Liu, A. Mignatti, K. Kovalski, and L. Ossowski, *Mol. Biol. Cell*, 2001, **12**, 863–79.

51. D. Liu, J. Aguirre Ghiso, Y. Estrada, and L. Ossowski, *Cancer Cell*, 2002, **1**, 445–57.
52. D. Destouches, D. El Khoury, Y. Hamma-Kourbali, B. Krust, P. Albanese, P. Katsoris, G. Guichard, J. P. Briand, J. Courty, and A. G. Hovanessian, *PLoS One*, 2008, **3**, e2518.
53. V. Fogal, K. N. Sugahara, E. Ruoslahti, and S. Christian, *Angiogenesis*, 2009, **12**, 91–100.
54. G. R. Reddy, M. S. Bhojani, P. McConville, J. Moody, B. a Moffat, D. E. Hall, G. Kim, Y.-E. L. Koo, M. J. Woolliscroft, J. V Sugai, T. D. Johnson, M. a Philbert, R. Kopelman, A. Rehemtulla, and B. D. Ross, *Clin. Cancer Res.*, 2006, **12**, 6677–86.
55. I. Winer, S. Wang, Y.-E. K. Lee, W. Fan, Y. Gong, D. Burgos-Ojeda, G. Spahlinger, R. Kopelman, and R. J. Buckanovich, *Cancer Res.*, 2010, **70**, 8674–83.
56. M. S. Bhojani, R. Ranga, G. D. Luker, A. Rehemtulla, B. D. Ross, and M. E. Van Dort, *PLoS One*, 2011, **6**, e22418.
57. S. K. Khaldoyanidi, V. V Glinsky, L. Sikora, A. B. Glinskii, V. V Mossine, T. P. Quinn, G. V Glinsky, and P. Sriramarao, *J. Biol. Chem.*, 2003, **278**, 4127–34.
58. M. Hamidi, A. Azadi, and P. Rafiei, *Adv. Drug Deliv. Rev.*, 2008, **60**, 1638–49.
59. K. S. Soppimath, T. M. Aminabhavi, A. R. Kulkarni, and W. E. Rudzinski, *J. Control. Release*, 2001, **70**, 1–20.
60. D. Gao, H. Xu, M. A. Philbert, and R. Kopelman, *Nano Lett.*, 2008, **8**, 3320–4.
61. S. Wang, G. Kim, Y.-E. K. Lee, H. J. Hah, M. Ethirajan, R. K. Pandey, and R. Kopelman, *ACS Nano*, 2012, **6**, 6843–51.
62. M. A. M. Oliveira, C. Boyer, M. Nele, J. C. Pinto, P. B. Zetterlund, and T. P. Davis, *Macromolecules*, 2011, **44**, 7167–7175.
63. C. Pinto Reis, R. J. Neufeld, A. J. Ribeiro, and F. Veiga, *Nanomedicine*, 2006, **2**, 8–21.
64. B. A. Moffat, G. R. Reddy, P. McConville, D. E. Hall, T. L. Chenevert, R. R. Kopelman, M. Philbert, R. Weissleder, A. Rehemtulla, and B. D. Ross, *Mol. Imaging*, 2003, **2**, 324–32.
65. P. Sharma, S. Brown, G. Walter, S. Santra, and B. Moudgil, *Adv. Colloid Interface Sci.*, 2006, **123-126**, 471–85.
66. S. T. Selvan, T. T. Y. Tan, D. K. Yi, and N. R. Jana, *Langmuir*, 2010, **26**, 11631–41.
67. S. M. Buck, Y.-E. L. Koo, E. Park, H. Xu, M. A. Philbert, M. A. Brasuel, and R. Kopelman, *Curr. Opin. Chem. Biol.*, 2004, **8**, 540–6.
68. S. M. Buck, H. Xu, M. Brasuel, M. A. Philbert, and R. Kopelman, *Talanta*, 2004, **63**, 41–59.
69. Y.-E. Koo Lee and R. Kopelman, in *Imaging and Spectroscopic Analysis of Living Cells Optical and Spectroscopic Techniques Methods in enzymology*, ed. P. M. Conn, UK Academic Press, First., 2012, vol. 504, pp. 419–70.
70. M. J. Moreno, E. Monson, R. G. Reddy, A. Rehemtulla, B. D. Ross, M. Philbert, R. J. Schneider, and R. Kopelman, *Sensors Actuators B Chem.*, 2003, **90**, 82–89.
71. W. Tang, H. Xu, R. Kopelman, and M. A. Philbert, *Photochem. Photobiol.*, 2005, **81**, 242–9.
72. S. Wang, W. Fan, G. Kim, H. J. Hah, Y.-E. K. Lee, R. Kopelman, M. Ethirajan, A. Gupta, L. N. Goswami, P. Pera, J. Morgan, and R. K. Pandey, *Lasers Surg. Med.*, 2011, **43**, 686–95.
73. M. Oishi, H. Hayashi, M. Iijima, and Y. Nagasaki, *J. Mater. Chem.*, 2007, **17**, 3720–3725.
74. D. Putnam and J. Kopecek, *Bioconjug. Chem.*, 1995, **6**, 483–92.
75. F. Meng, W. E. Hennink, and Z. Zhong, *Biomaterials*, 2009, **30**, 2180–98.

76. R. Cheng, F. Feng, F. Meng, C. Deng, J. Feijen, and Z. Zhong, *J. Control. Release*, 2011, **152**, 2–12.
77. S. Shah, A. Pal, R. Gude, and S. Devi, *Eur. Polym. J.*, 2010, **46**, 958–967.
78. H. Hillaireau and P. Couvreur, *Cell. Mol. Life Sci.*, 2009, **66**, 2873–96.
79. T. Kanaseki and K. Kadota, *J. Cell Biol.*, 1969, **42**, 202–20.
80. L. M. Bareford and P. W. Swaan, *Adv. Drug Deliv. Rev.*, 2007, **59**, 748–58.
81. S. D. Conner and S. L. Schmid, *Nature*, 2003, **422**, 37–44.
82. L. Pelkmans, T. Bürli, M. Zerial, and A. Helenius, *Cell*, 2004, **118**, 767–80.
83. W. Querbes, B. a O'Hara, G. Williams, and W. J. Atwood, *J. Virol.*, 2006, **80**, 9402–13.
84. J. A. Swanson and C. Watts, *Trends Cell Biol.*, 1995, **5**, 424–8.
85. S. Mukherjee, R. N. Ghosh, and F. R. Maxfield, *Physiol. Rev.*, 1997, **77**, 759.
86. E. L. Racoosin and J. A. Swanson, *J. Cell Sci.*, 1992, **102 (Pt 4**, 867–80.
87. J. Rejman, V. Oberle, I. S. Zuhorn, and D. Hoekstra, *Biochem. J.*, 2004, **377**, 159–69.
88. S. Zhang, J. Li, G. Lykotrafitis, G. Bao, and S. Suresh, *Adv. Mater.*, 2009, **21**, 419–424.
89. H. Yuan and S. Zhang, *Appl. Phys. Lett.*, 2010, **96**, 033704.
90. O. Harush-Frenkel, E. Rozentur, S. Benita, and Y. Altschuler, *Biomacromolecules*, 2008, **9**, 435–43.
91. O. P. Perumal, R. Inapagolla, S. Kannan, and R. M. Kannan, *Biomaterials*, 2008, **29**, 3469–3476.
92. Y. Zhang, M. Yang, J.-H. Park, J. Singelyn, H. Ma, M. J. Sailor, E. Ruoslahti, M. Ozkan, and C. Ozkan, *Small*, 2009, **5**, 1990–6.
93. Y. Geng, P. Dalhaimer, S. Cai, R. Tsai, M. Tewari, T. Minko, and D. E. Discher, *Nat. Nanotechnol.*, 2007, **2**, 249–55.
94. J.-H. Park, G. von Maltzahn, L. Zhang, M. P. Schwartz, E. Ruoslahti, S. N. Bhatia, and M. J. Sailor, *Adv. Mater.*, 2008, **20**, 1630–1635.
95. X. Banquy, F. Suarez, A. Argaw, J.-M. Rabanel, P. Grutter, J.-F. Bouchard, P. Hildgen, and S. Giasson, *Soft Matter*, 2009, **5**, 3984–3991.
96. S. Lerch, M. Dass, A. Musyanovych, K. Landfester, and V. Mailänder, *Eur. J. Pharm. Biopharm.*, 2013, **84**, 265–74.
97. T. Cedervall, I. Lynch, M. Foy, T. Berggård, S. C. Donnelly, G. Cagney, S. Linse, and K. a Dawson, *Angew. Chem. Int. Ed. Engl.*, 2007, **46**, 5754–6.
98. T. Cedervall, I. Lynch, S. Lindman, T. Berggård, E. Thulin, H. Nilsson, K. a Dawson, and S. Linse, *Proc. Natl. Acad. Sci. U. S. A.*, 2007, **104**, 2050–5.
99. P. P. Roux and J. Blenis, *Microbiol. Mol. Biol. Rev.*, 2004, **68**, 320–44.
100. D. Volonté, F. Galbiati, R. G. Pestell, and M. P. Lisanti, *J. Biol. Chem.*, 2001, **276**, 8094–103.
101. G. Macé, M. Miaczynska, M. Zerial, and A. R. Nebreda, *EMBO J.*, 2005, **24**, 3235–46.
102. U. Sydlik, K. Bierhals, M. Soufi, J. Abel, R. P. F. Schins, and K. Unfried, *Am. J. Physiol. Lung Cell. Mol. Physiol.*, 2006, **291**, L725–33.
103. K. Unfried, U. Sydlik, K. Bierhals, A. Weissenberg, and J. Abel, *Am. J. Physiol. Lung Cell. Mol. Physiol.*, 2008, **294**, L358–67.
104. F. Marano, S. Hussain, F. Rodrigues-Lima, A. Baeza-Squiban, and S. Boland, *Arch. Toxicol.*, 2011, **85**, 733–41.
105. J. Rauch, W. Kolch, S. Laurent, and M. Mahmoudi, *Chem. Rev.*, 2013, **113**, 3391–406.
106. Y. Son, Y.-K. Cheong, N.-H. Kim, H.-T. Chung, D. G. Kang, and H.-O. Pae, *J. Signal Transduct.*, 2011, **2011**, 792639.

Chapter 2

Surface Engineering of Polyacrylamide Hydrogel Nanoparticles:

Surface PEGylation and Functionalization with F3 peptides

This chapter has been adapted with minor modification from the following published article:

L. Karamchand *et al.,* Modulation of Hydrogel Nanoparticle Intracellular Trafficking by Surface Engineering with Tumor Targeting Peptide. Nanoscale, 2013; 5(21): 10327-44

2.1 Introduction

Polyethylene glycol (PEG; H-(O-CH_2-CH_2)$_n$ -OH) is a biocompatible, linear synthetic polymer that can be prepared in a range of molecular weights, and with a variety of terminal functional groups that permit their bioconjugation to various biomolecules and/or chemically functionalized surfaces. The surface modification of nanoparticles (NPs) with PEG molecules, otherwise known as PEGylation, is commonly used to confer *"stealth capability"* to the NPs for *in vivo* applications, specifically to evade their recognition, and removal from the circulation by the macrophages of the mononuclear phagocytic system (MPS). The properties of PEG that permit its use as a stealth barrier include its hydrophilicity, flexibility, and neutral charge at physiological pH in biological fluids. Specifically, surface conjugated PEG molecules reduce the opsonization of NPs with serum proteins in the blood stream (adhesion of serum proteins to the NP surface in a charge-dependent manner),[1] and hence their recognition, and phagocytic removal

by the MPS macrophages.[2] Furthermore, bare NPs tend to aggregate either via hydrophobic interactions, or attractive van der Waals forces, which renders them susceptible to removal from the circulation by the MPS macrophages. Surface PEGylation also reduces NP aggregate formation in biological fluids, and thus reduces the phagocytic recognition, and elimination of the NPs from the circulation. Evading the MPS macrophages is therefore necessary for prolonging the circulating half-life of the NPs, so as to increase their likelihood of accumulating within the tumor site.[3] Since solid tumors typically grow to only a few centimeters in diameter, which constitutes only a small fraction of the total size of the patient, the probability of systemically injected NPs encountering the tumor site is rather small. This is further compounded by the fact that the NPs have to overcome physiological barriers, such as the MPS macrophages, in order to reach the tumor site. Hence, the surface PEGylation of NPs has become an important NP surface engineering strategy for extending their circulating half-life, so that a greater fraction of the systemically administered PEGylated-NP dose accumulates within the tumor site over time and delivers its cytotoxic payload, as compared to the non-PEGylated NP counterpart.

The surface PEGylation of polyacrylamide (PAA) NPs for *in vivo* applications has previously been reported by the Kopelman group.[4] In addition to functioning as a stealth barrier, the PEG molecules also serve as crosslinkers via which tumor-targeting ligands, such as the Nucleolin-specific F3 peptide (KDEPQRRSARLSAKPAPPKPEPKPKKAPAKKC), can be attached to the NP surface. Given the inherent flexibility of the PEG molecules, the PEG-crosslinked targeting ligands in turn have a greater range of conformational flexibility, relative to the NP surface, thus increasing the probability of the targeting ligands to locate, and bind, their target receptors upon contact with the cell membrane. Hence, for the purpose of this *in vitro* study, the surface

PEGylation of the PAA-NPs was important, so as to (i) accurately mimic the surface physicochemical behavior of the F3-targeted PAA-NPs (F3NPs) designed for *in vivo* applications, and (ii) minimize the opsonization of the PAA-NPs with culture medium serum proteins, which would otherwise prevent exclusive F3 peptide/Nucleolin (ligand/receptor)-mediated interactions of the F3NPs with the tumor cell surfaces. Furthermore, the surface PEGylation of the amine-functionalized, positively-charged PAA-NPs also permitted a concomitant reduction in the PAA-NP surface charge, which was necessary for prohibiting non-specific electrostatic interactions of the F3NPs with the negatively-charged cell membrane. The underlying chemistry of this phenomenon, and the optimization of the PAA-NP surface PEGylation will be discussed further.

Last, the optimization of the F3 peptide density on the PAA-NP surface is necessary so as to maximize the multivalency effect of the F3NPs, i.e., to maximize the number of Nucleolin surface receptors that a single F3NP can simultaneously engage. Considering the reaction:

F3NP + Nucleolin ⇌ Nucleolin-F3NP complex

with k_{on} (association rate) denoting the forward reaction rate, and k_{off} (dissociation rate) denoting the reverse reaction rate, a higher number of F3 peptides per PAA-NP has the effect of lowering the k_{off} (dissociation rate), while the k_{on} (association rate) typically remains unchanged.[5] Hence, an F3NP engineered with the ability to simultaneously bind multiple Nucleolin receptors, with a low k_{off} rate, effectively acts as a cross-linking agent, which induces localized clustering of Nucleolin receptors at the cell surface. This process produces a thermodynamically favorable localized decrease in the Gibbs free energy at the membrane site to which the F3NP is bound, which in turn induces the cell membrane to wrap around the nanoparticle, and form a membrane-bound endosome around the F3NP.[6]

In this chapter, the reaction scheme for the synthesis of the PAA-NPs is first presented, followed by a systematic description of the step-wise optimization of the (i) surface PEGylation of the PAA-NPs, and (ii) surface functionalization of the PEGylated PAA-NPs with F3 peptides.

2.2 Synthesis and characterization of FITC-labeled hydrogel polyacrylamide nanoparticles

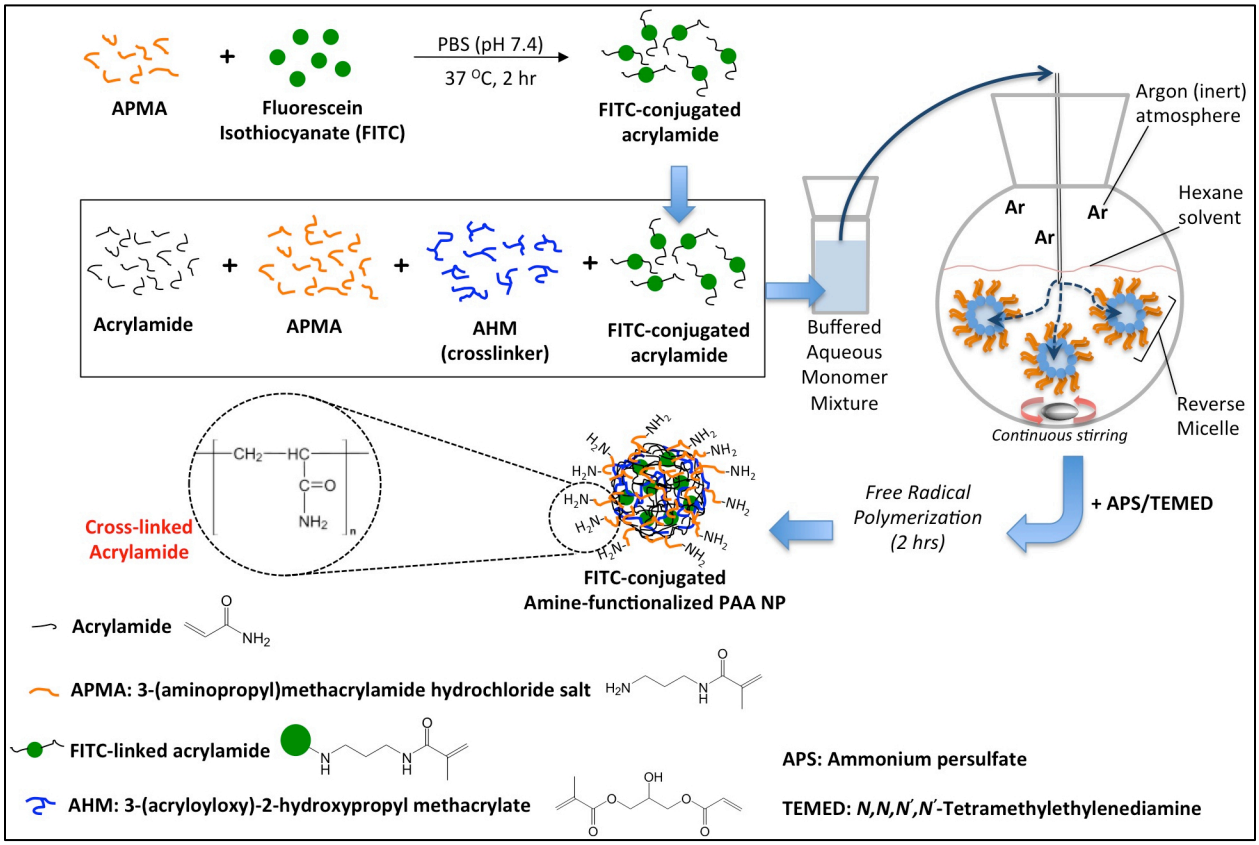

Fig. 2.1 Reaction scheme for the synthesis of FITC fluorophore-labeled, amine-functionalized polyacrylamide nanoparticles. First, covalent coupling of FITC to APMA was achieved through the reactivity between the isothiocyanate (-CNS) group of fluorescein, and the amine (-NH_2 group) of APMA. Second, the FITC-conjugated APMA, was combined with additional APMA, Acrylamide monomer, and AHM crosslinker in an aqueous mixture. This aqueous monomer mixture was then injected into a stirred reverse micelle system, comprising the detergents Brij-30 and sodium dioctyl sulfosuccinate in hexane. The aqueous monomer mixture incorporates into the hydrophilic core of the reverse micelles, which essentially serve as 'nanoscale' vessels within which the acrylamide monomer mixture can be polymerized into polyacrylamide nanoparticles. Third, the addition of the radical initiators APS and TEMED to the reaction vessel initiates free radical polymerization of the acrylamide, APMA and AHM molecules into hydrogel nanoparticles. Polymerization occurs under an inert (Argon) atmosphere that has been purged of oxygen, which would otherwise quench the radicals generated by APS and TEMED. Note that the APMA monomer confers amine-functionality to the PAA hydrogel nanoparticles, and that the presence of free amine groups at the surface of the PAA hydrogel nanoparticle confers to it a positive zeta potential (surface charge).

Amine surface-functionalized hydrogel PAA-NPs were prepared by water-in-oil (reverse micelle) microemulsion radical polymerization, as previously reported by our lab.[7] Figure 2.1 illustrates the reaction scheme by which the PAA-NPs were synthesized. Fluorescein isothiocyanate (FITC) fluorophore was conjugated to the NP matrix backbone by covalent linkage to the co-monomer, 3-aminopropylmethacrylamide (APMA), prior to nanoparticle formation, to facilitate fluorescent imaging of the NPs in subsequent cellular binding affinity, and endocytosis experiments. The diameter of the spherical hydrogel PAA-NPs was determined to be 21 ± 5 nm by scanning electron microscopy (SEM), which is based on the analysis of 50 individual nanoparticle structures (Fig. 2.2.1). In aqueous solution, however, the amine-functionalized hydrogel PAA-NPs exhibited a median hydrodynamic diameter of approximately 60 nm, as determined by dynamic light scattering (DLS) (Fig. 2.2.2). DLS measurements indicated narrow size distributions for the amine-functionalized hydrogel PAA-NPs, which confirms that the nanoparticles do not aggregate in solution. The larger NP diameter obtained by DLS characterization is attributed to the characteristic ability of hydrogels to swell in aqueous solution. We note that this size may vary with salinity.[8] Furthermore, the sample preparation procedure for SEM requires dehydration, which indeed causes the hydrogel nanoparticles to shrink and accounts for the discrepancy in size measurements between SEM and DLS methods.

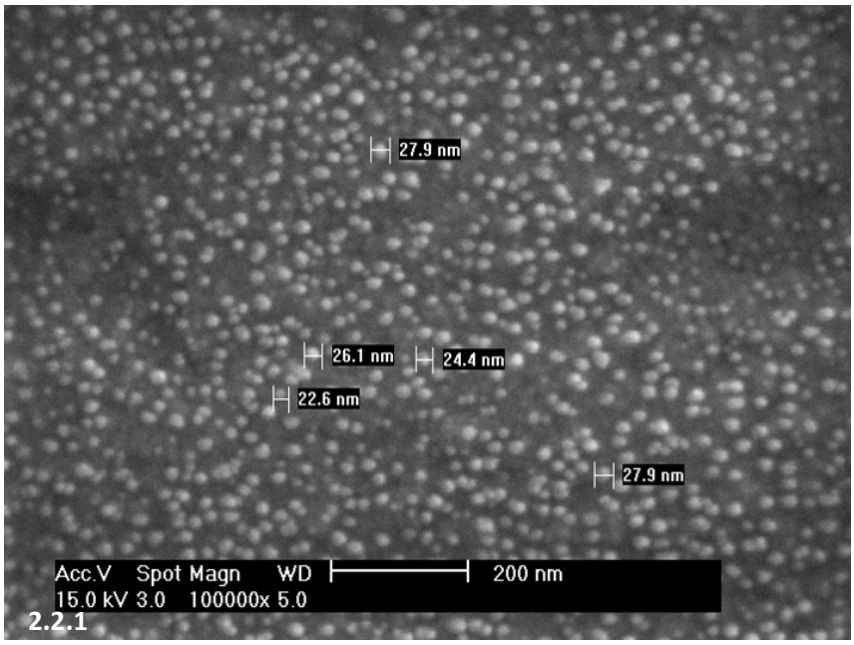

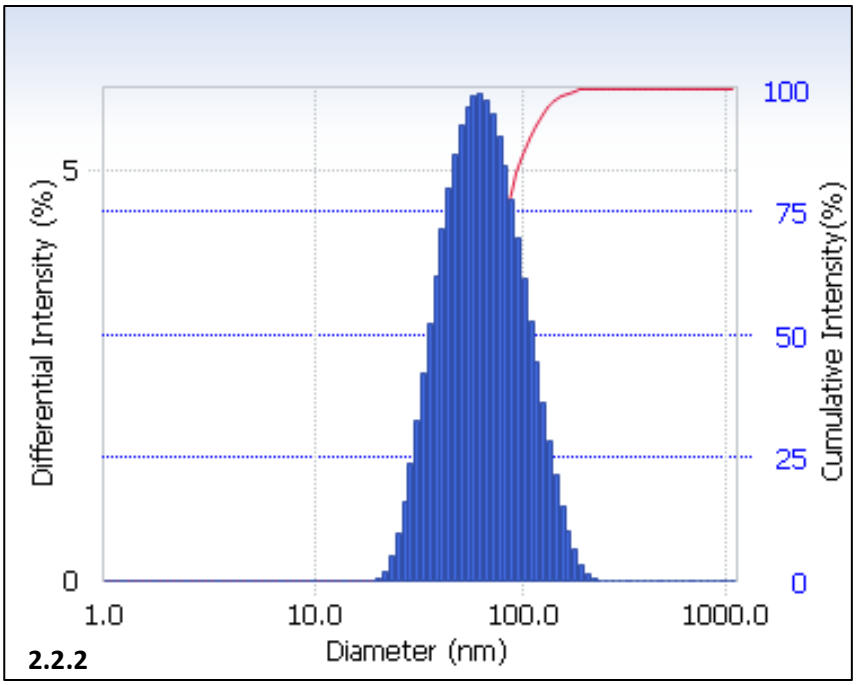

Fig. 2.2.1 Scanning electron micrograph of the amine-functionalized, non-targeted PAA-NPs (NTNPs). The nanoparticles exhibited spherical morphology with a mean diameter of 21 ± 5 nm. Magnification: 100,000x.
Fig. 2.2.2 Dynamic light scattering data for amine-functionalized, non-targeted PAA-NPs (NTNPs) suspended to a final concentration of (1mg.mL^{-1}) in 10 mM PBS buffer. Average diameter: 63.6 nm, Polydispersity index: 0.222

2.3 Optimization of polyacrylamide nanoparticle surface PEGylation

Positively charged NPs have a propensity to bind non-specifically to the negatively charged cell membranes through electrostatic interactions. Furthermore, the formation of a corona of serum proteins around the NP (opsonization) in cell culture media can potentially interfere with the ligand-receptor mediated interactions between the ligand-functionalized NP, and its target tumor cell. We therefore, first optimized the PEGylation of the amine surface-functionalized PAA-NPs in order to attenuate their non-specific cell binding, and opsonization with serum proteins, prior to optimizing the surface coverage of the PAA-NPs with F3 peptide. Following synthesis, the surfaces of the amine-functionalized FITC-labeled PAA-NPs were modified with heterobifunctional succinimidyl ester – Polyethylene glycol – maleimidyl ester (SCM-PEG-MAL) molecules. Briefly, the reaction was achieved in a two-step process; (i) initial conjugation of heterobifunctional PEG molecules via their SCM termini to the primary amine groups ($-NH_2$) on the PAA-NP surface (Fig. 2.3), followed by, (ii) conjugation of L-cysteine to the MAL termini of the PEG crosslinkers (Cys-capping). The quantity of PEG required to completely neutralize the positive surface charge of amine-functionalized PAA-NPs (~ +16 mV) (Fig. 2.4) was determined by treating increasing masses of SCM-PEG-MAL (0.4, 2.0 and 4.0 mg) with a fixed mass (50 mg) of PAA-NPs, followed by measurement of the zeta potential (surface charge) of the resultant PEGylated PAA-NPs (Fig. 2.4). The positive surface charge of the unmodified PAA-NPs is attributed to the presence of protonated amine groups ($-NH_3^+$) on the PAA-NP surface. Figure 2.4 illustrates the concentration dependent reduction in the positive surface charge of the PAA-NPs by PEG; a ratio of 4 mg PEG: 50 mg lyophilized PAA-NP achieved a reduction in zeta potential from + 16 ± 2.89 mV to – 0.4 ± 0.82 mV without any observable non-specific binding of these PEGylated PAA-NPs to MDA-MB-435 cells. Figure 2.4 (inset images)

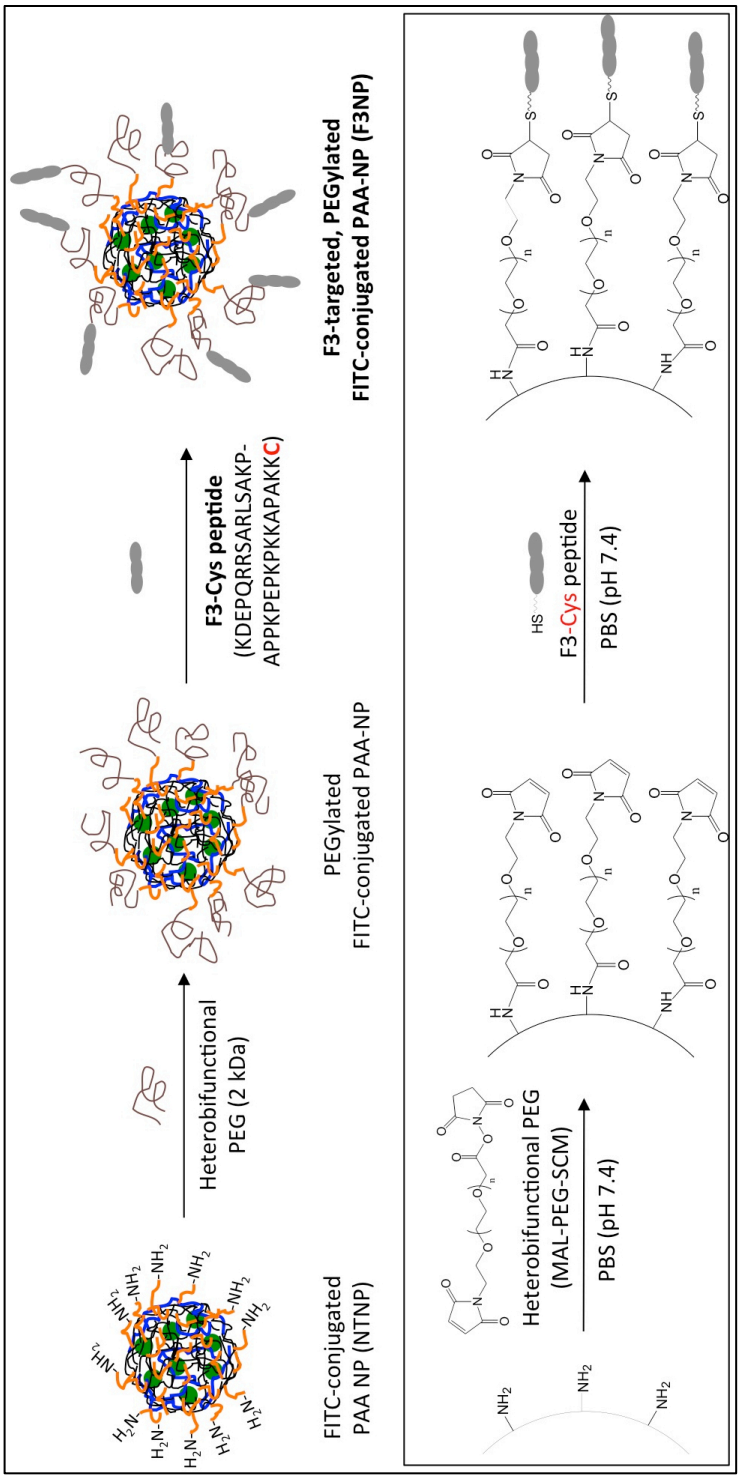

Fig. 2.3 Reaction scheme for the surface PEGylation of the amine-functionalized PAA-NPs with heterobifunctional maleimidyl ester – Polyethylene Glycol – succinimidyl ester (SCM-PEG-MAL) molecules, and subsequent surface functionalization of the PEGylated PAA-NPs with F3-Cys peptide using SCM-PEG-MAL as surface cross-linkers. The succinimidyl ester group on the PEG molecule reacts directly with a single surface amine group (-NH_2) on the PAA-NPs, which results in a stable amide bond between the PAA-NP and the PEG molecule. The maleimidyl ester group located on the opposite end of the PEG molecule reacts exclusively with the thiol (-SH) group on the side chain of L-Cysteine, located on the C-terminal of F3-Cys peptide.

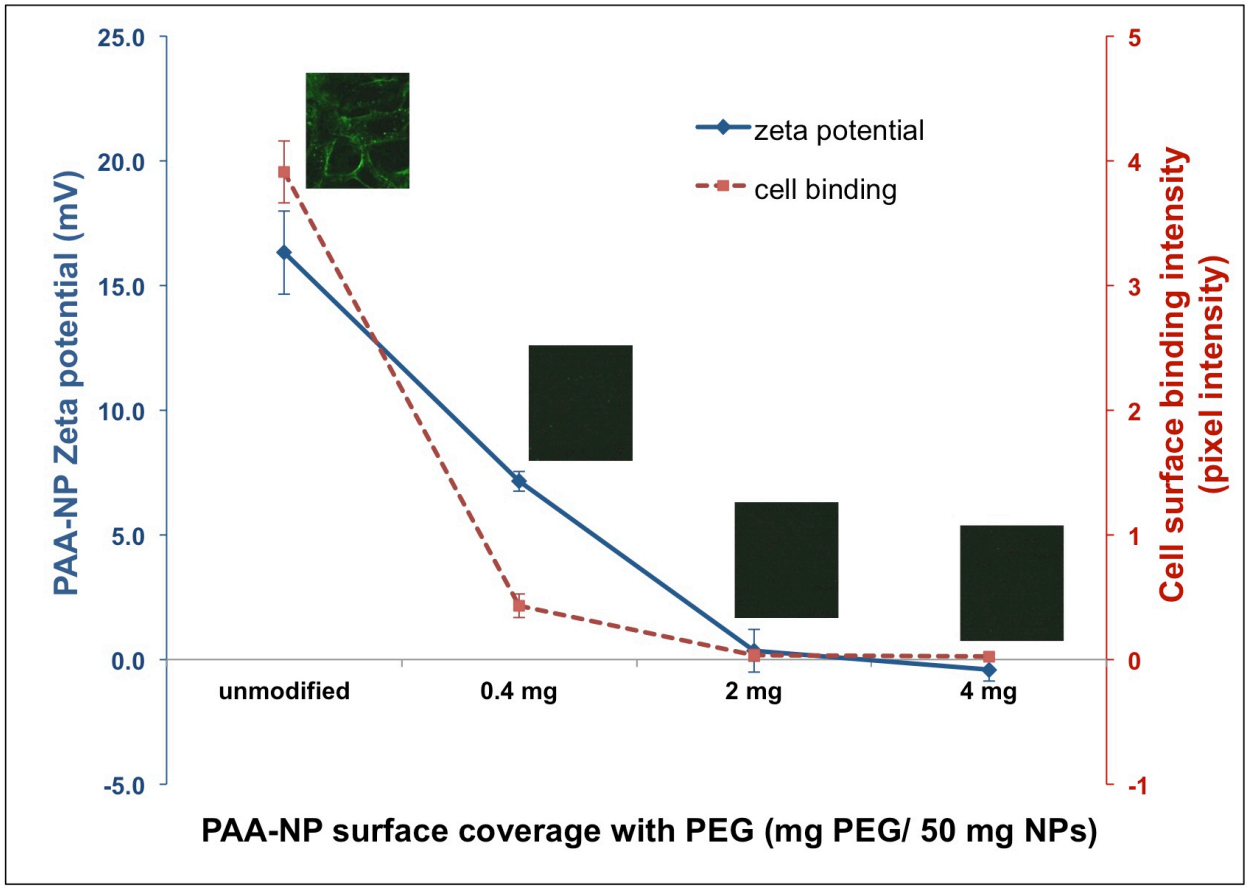

Fig. 2.4 Optimization of PAA nanoparticle surface PEGylation to minimize non-specific cell surface binding. The zeta potential (surface charge) of the various PEGylated PAA nanoparticle formulations were measured by electrophoretic light scattering, and compared to their potential for non-specific cell binding to MDA-MB-435 cells. The increase in PAA nanoparticle surface coverage with PEG results in a corresponding decrease in the zeta potential of the PAA nanoparticle along with its potential for non-specific binding to the negatively-charged cell membranes (inset images). Since the ratio of 4 mg PEG: 50 mg PAA nanoparticles effectively reduced the zeta potential of the PAA nanoparticles to approximately 0 mV, this formulation was selected for further synthesis of the F3-targeted PEGylated PAA nanoparticles.

illustrates the direct correlation between the zeta potential of the non-PEGylated/PEGylated PAA-NPs, and their degree of non-specific binding to MDA-MB-435 cells. All subsequent PAA-NP PEGylations were performed according to the above optimal PEG: PAA-NP ratio (4 mg PEG: 50 mg lyophilized PAA-NP) to facilitate further surface functionalization with F3 peptide.

2.4 Optimization of the F3 peptide surface functionalization

The engineering of NP surfaces with multiple targeting ligands (multivalency) has been shown to increase both their cell binding avidity, and rate of internalization by the target cells.[9,10] In addition, the density and availability of cell surface receptors[5] and targeting ligand density on the NP surface[11–13] regulates the internalization of the NP. This underscores the importance of optimizing the physicochemical properties of a hydrogel NP, relative to the receptor profile of the target cell, and the desired intracellular trafficking pathway, so as to maximize therapeutic efficacy. Given the influence that the degree of ligand coverage on a NP surface exerts on its cell binding and internalization, we optimized the surface coverage of the PEGylated PAA-NPs with F3 peptide (F3NPs) based on their interaction (in terms of cell surface binding and internalization) with three different nucleolin-expressing cell lines.

Briefly, following surface PEGylation of the PAA-NPs, separate batches of F3NPs, each bearing different degrees of F3 peptide surface coverage, were prepared (Fig. 2.3). Thereafter, each F3NP batch underwent Cys-capping of their PEG crosslinker MAL termini to ensure that the cellular binding of these NPs are governed solely by the interaction between the surface conjugated F3 peptides, and cell surface nucleolin receptors. A linear relationship was observed between the quantity of F3-Cys peptide conjugated to the PEGylated PAA-NP surfaces, and the increase in their zeta potential (surface charge) (Fig. 2.5). This observation is attributed to the multiple arginine and lysine residues of F3 peptide whose side-chain amines are positively charged at neutral pH. Also, DLS-based size characterization of the F3-targeted PEGylated PAA-NPs revealed that their hydrodynamic diameters were not significantly different from that of the amine-functionalized, non-targeted PAA-NPs (Figs. 2.6.1 and 2.6.2).

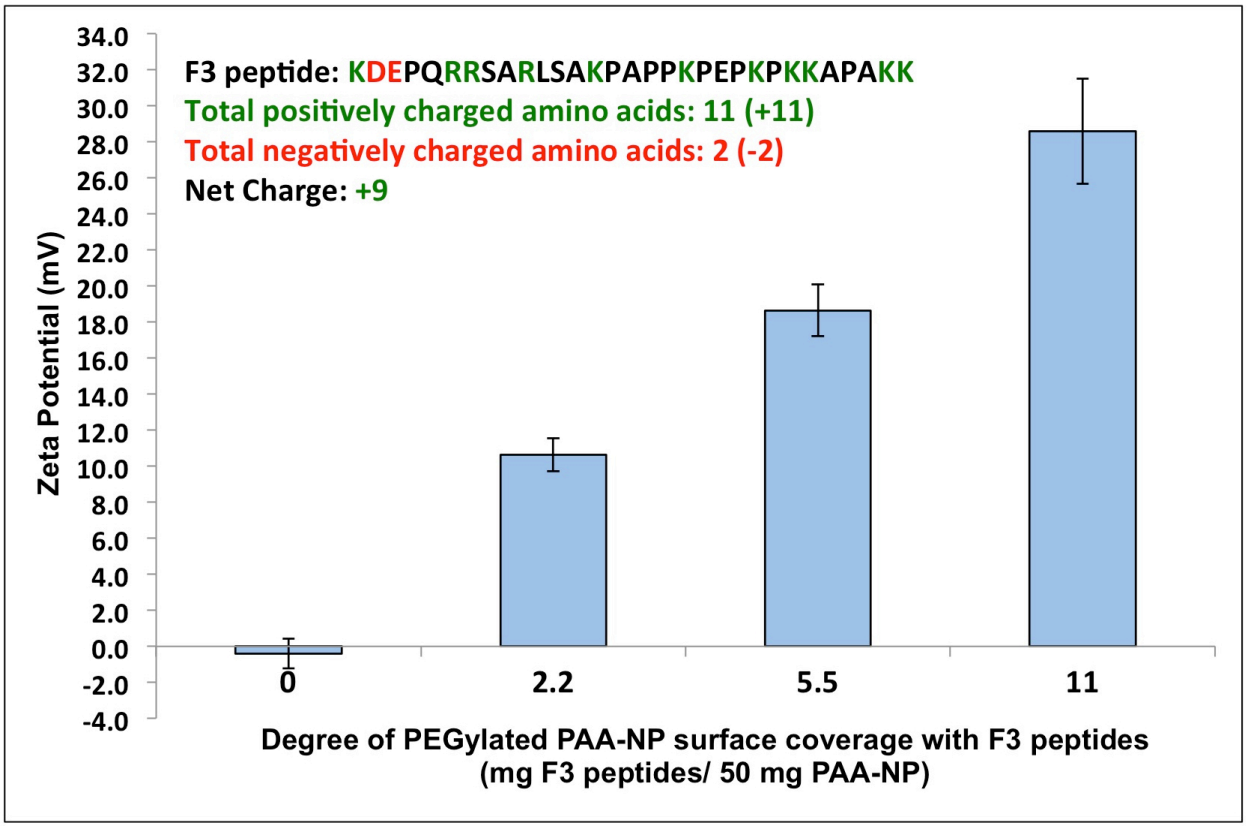

Fig. 2.5 Linear relationship between the degree of surface coverage of the PEGylated PAA-NPs with F3 peptide and their corresponding zeta potentials (surface charge). Each F3 peptide has a net charge of +9 at physiological pH 7.4 due to the protonation of the side chains of its Lysine (K) and Arginine (R) residues.

Thereafter, the 'cellular sequestration' (NP binding + uptake) profiles of the amine-functionalized, non-targeted PAA-NPs (NTNPs), and the various F3-targeted PEGylated PAA-NP (F3NP) formulations was studied in three different nucleolin surface-overexpressing live cell lines; MDA-MB-435 human breast adenocarcinoma, 9L rat gliosarcoma, and MCF-7 human breast adenocarcinoma, using confocal fluorescence microscopy. Here, we define the 'cellular sequestration' of a NP as the combination of (i) the degree of NP-binding to the cell membrane, which is related to the cell binding avidity of that specific NP and, (ii) the degree to which the NP is internalized by a particular cell line within a specific period of time. The results are summarized in Fig. 2.7, and Table 2.1.

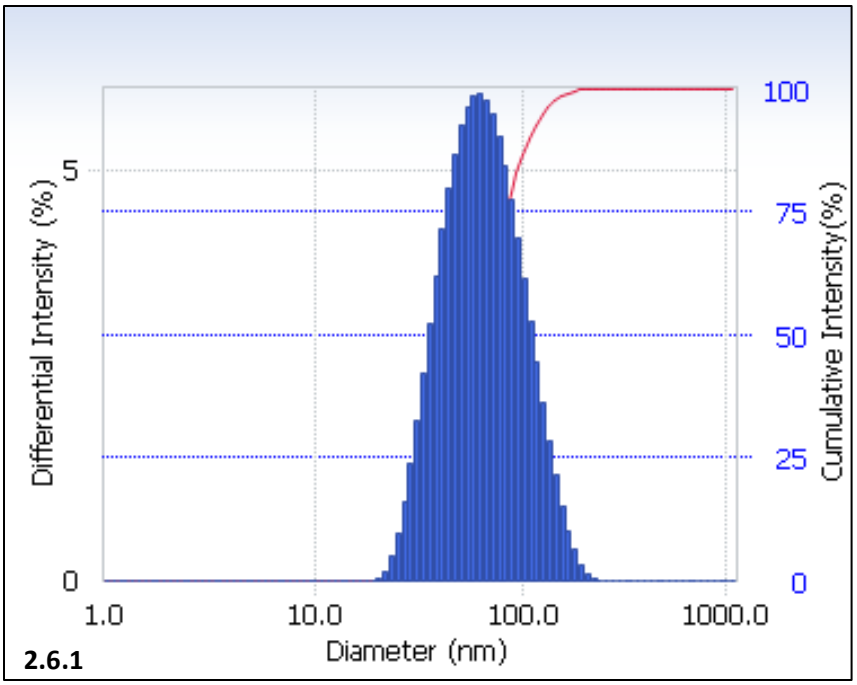

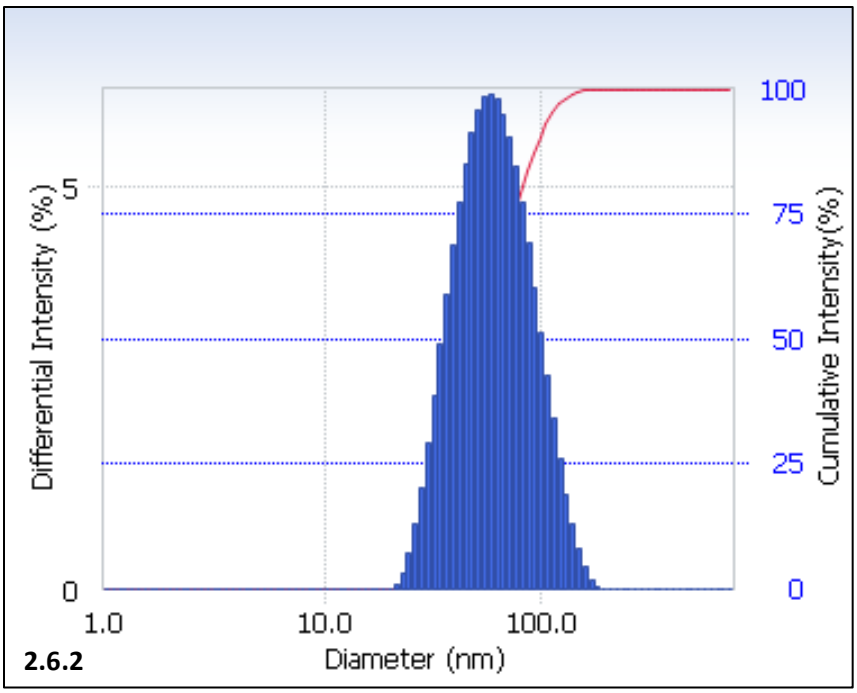

Fig. 2.6.1 Dynamic light scattering data for the amine-functionalized, non-targeted PAA-NPs (NTNPs) suspended to a final concentration of (1 mg.mL^{-1}) in 10 mM PBS buffer. Average diameter: 63.6 nm, Polydispersity index: 0.222
Fig. 2.6.2 Dynamic light scattering data for F3-targeted, PEGylated PAA-NPs (F3NPs) suspended to a final concentration of (1 mg.mL^{-1}) in 10 mM PBS buffer. Average diameter: 58.5 nm, Polydispersity index: 0.126

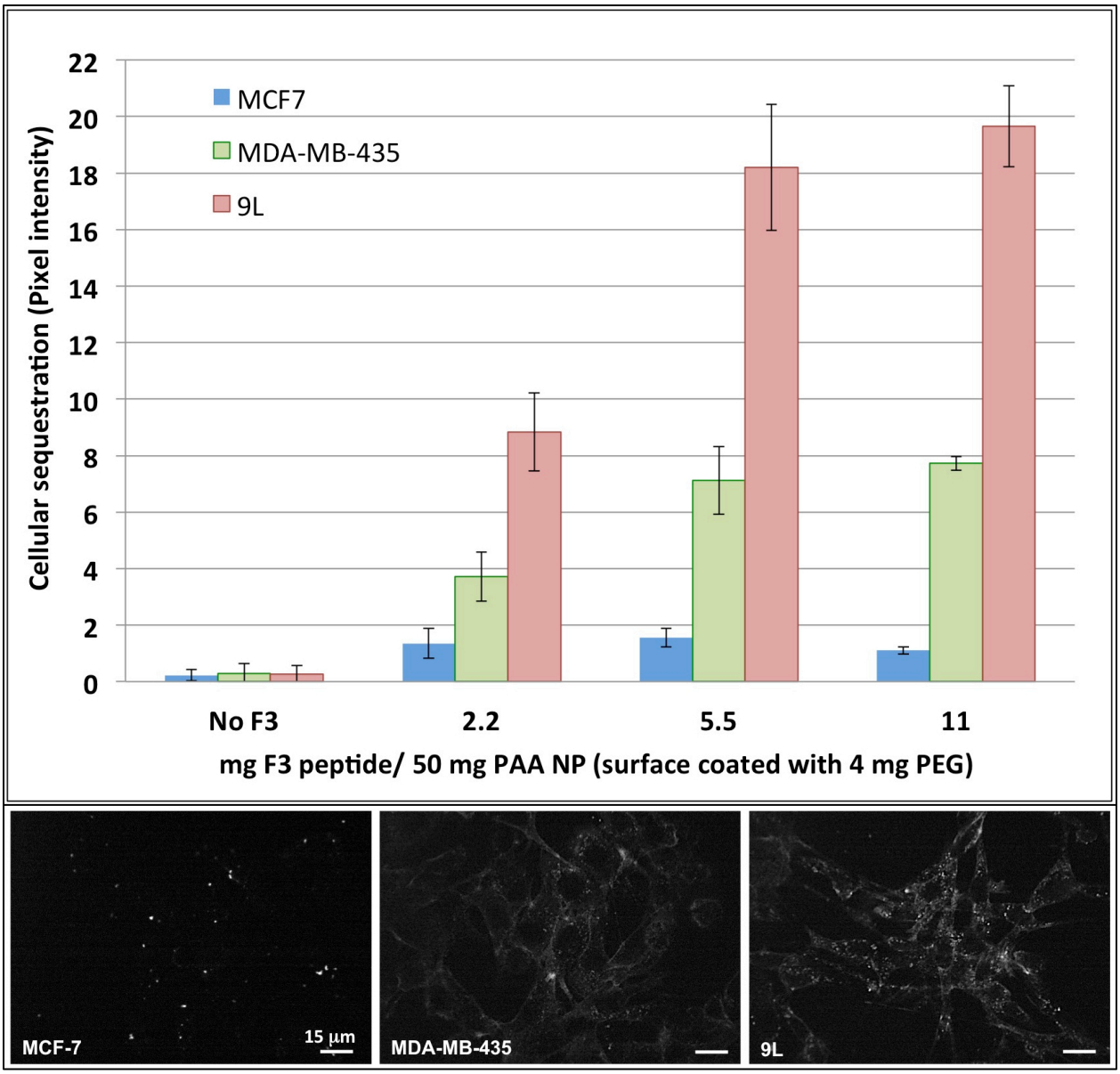

Fig. 2.7 Trend of cellular sequestration versus F3 peptide surface coverage of the PEGylated PAA nanoparticles for the MCF-7, MDA-MB-435 and 9L cell lines. In both the MDA-MB-435 and 9L cell lines, cellular sequestration reached saturation at a ratio of 11 mg F3 peptide: 50 mg PAA-NC, whereas saturation occurred at a ratio of 2.2 mg F3 peptide: 50 mg PAA-NC in the MCF-7 cell line. ***Inset images:*** Representative confocal fluorescence images depicting varying degrees of cellular sequestration of the F3NPs (11 mg F3: 4mg PEG: 50 mg PAA-NP formulation) by the MCF-7, MDA-MB-435 and 9L cell lines. Scale bar: 15 µm.

Several important observations were noted as follows. First, the cellular sequestration of the F3NPS increased linearly relative to the degree of surface coverage with F3 peptide up to 5.5 mg F3: 50 mg PAA-NPs, with saturation occurring at the 11 mg F3: 50 mg PAA-NP formulation in

Table 2.1 Relative cellular sequestration values for the NTNPs and F3NPs in the MCF7, MDA-MB-435 and 9L cell lines (derived from Fig. 2.7). Cellular sequestration values for the F3NPs were normalized relative to that of the unmodified, non-targeted PAA-NPs for each cell line. The 9L cell line consistently exhibited an approximately 2.7 times higher cellular sequestration for the F3NPs than the MDA-MB-435 cell line.

F3 peptide mass (mg)/ 50 mg PEGylated PAA-NPs	**0**	**2.2**	**5.5**	**11**
	Relative cellular sequestration values			
MCF-7	1.00	6.07	6.93	4.92
MDA-MB-435	1.00	13.23	25.34	27.49
9L	1.00	34.60	71.25	76.92

both the MDA-MB-435 and 9L cell lines. In contrast, the cellular sequestration profile of the F3NPs in the MCF-7 cell line reached saturation at a 5-fold lower F3 peptide surface coverage (2.2 mg F3: 50 mg PAA-NP formulation), although a slight decrease was observed at the 11 mg F3: 50 mg PAA-NP formulation (Fig. 2.7). This suggests that the MCF-7 cells express surface nucleolin at a markedly lower level and/or internalize the F3NPs at a slower rate than both the 9L and MDA-MB-435 cell lines. Second, significant differences in cellular sequestration were observed across the three different cell lines for each F3NP formulation; the order of cellular sequestration, from highest to lowest, was 9L > MDA-MB-435 > MCF-7 (Fig. 2.7). However, all cell lines exhibited similar cellular sequestration values for the NTNPs (Fig. 2.7). Third, at the highest surface coverage with F3 peptide (11 mg F3 peptide: 50 mg PAA-NP), approximately 28-fold and 77-fold enhancements in F3NP cellular sequestration were observed for the MDA-MB-435 cell and 9L cell lines respectively, whereas a relatively weak 5-fold enhancement for the MCF-7 cell line was observed relative to the cellular sequestration of the NTNPs for these cell lines (Table 2.1). Notably, the difference in cellular sequestrations between the 9L and MDA-MB-435 cells remained nearly constant, i.e., ~ 2.7:1, over the entire range of nanoparticle surface coverage with F3 peptide. In contrast, the ratio of F3NP cellular sequestrations for both

9L and MDA-MB-435 cells relative to MCF-7 cells (9L: MCF-7 and MDA-MB-435: MCF-7) increased with each increment in the degree of nanoparticle surface coverage with F3 peptide (Table 2.1).

Since the above assays were performed in live cells, we anticipated that the rates at which the F3NPs were endocytosed by each cell line, following binding to the cell membranes, likely exerted a significant influence on the observed cellular sequestrations. Therefore, in order to eliminate the potential influence of endocytosis, and thus determine the cellular sequestration based only on the surface binding of the F3NPs to each cell type, the experiments were repeated in both live ATP-depleted and paraformaldehyde-fixed cells (Fig. 2.8) using the '11 mg F3: 50 mg PEGylated PAA-NP' formulation that exhibited saturation in the cellular sequestration assay with live 9L and MDA-MB-435 cells. The F3NP cellular sequestration ratios in fixed and ATP-depleted cells (9L: MDA-MB-435: MCF-7) were 2.64: 2.82: 1 and 4.36: 4.92: 1, respectively (Figure 2.8, Table 2.2). Importantly, both ATP-depletion and paraformaldehyde fixation elicited a marked reduction in the difference in magnitude of F3NP cellular sequestration observed between 9L and MDA-MB-435 cells, as well as between the MCF-7 cells and 9L/MDA-MB-435 cells. Most notably, under both cytostatic conditions, the F3NP cellular sequestration was slightly weaker in 9L cells than in MDA-MB-435 cells, albeit not statistically significant (Table 2.2).

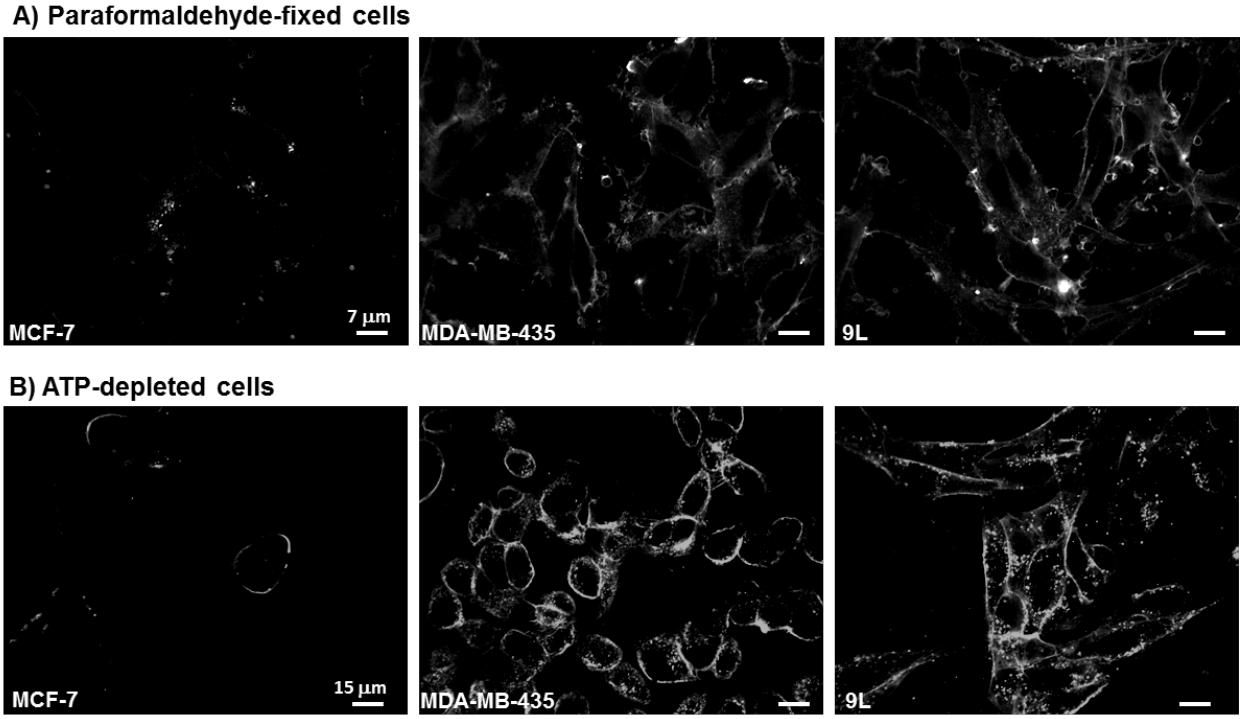

Fig. 2.8 Influence of endocytosis on the cellular sequestration of the F3-targeted PAA nanoparticles. Internalization of the F3NPs by the 9L, MDA-MB-435 and MCF-7 cell lines were blocked by either (A) paraformaldehyde-fixation (Scale bar: 7 μm), or (B) treatment with 2,4-dinitrophenol in order to deplete cellular ATP production (Scale bar: 15 μm).

Table 2.2 Cellular sequestration ratios of F3NPs in paraformaldehyde-fixed and ATP-depleted cells. The F3NP cellular sequestration for the MCF-7 cells remained negligible under both conditions. Therefore, the cellular sequestration values for the 9L and MDA-MB-435 cell lines were normalized relative to that of the MCF-7 cells. Under both conditions, the 9L cell line exhibited a slightly lower cellular sequestration of the F3NPs than the MDA-MB-435 cell line, whereas the cellular sequestration by the MCF-7 cell line, relative to the 9L and MDA-MB-435 cell lines, remained negligible. Therefore, the 9L and MDA-MB-435 cell lines likely have comparable cell surface densities of nucleolin receptors, however the 9L cells internalize the F3NPs at a faster rate than the MDA-MB-435 cells.

	MCF-7	**MDA-MB-435**	**9L**
Paraformaldehyde-fixed cells	1.00	2.82 ± 0.23	2.64 ± 0.34
ATP-depleted cells	1.00	4.92 ± 0.59	4.36 ± 0.39

2.5 Discussion

The versatility of the PAA nanoparticle is underscored by its compatibility with various bioconjugation chemistries that can be employed to incorporate a broad range of functionalities, both within the nanoparticle matrix and on its surface. The PAA hydrogel matrix employed in this study contained primary amine groups — originating from an amine-functionalized monomer, 3-aminopropylmethacrylamide (APMA) — both within the interior and on the surface of the nanoparticle. These amine groups can be easily functionalized, using diverse chemical modifications. Specifically, this permitted both labeling of the hydrogel matrix interior with fluorescein isothiocyanate (FITC), and functionalization of the hydrogel nanoparticle surface with heterobifunctional SCM-PEG-MAL molecules, by exploiting the reactivity of amines with isothiocyanate and succinimidyl ester groups, respectively.

We now discuss, specifically, the rationale for the hydrogel nanoparticle surface engineering. Surface PEGylation improves the colloidal stability of nanoparticles, reduces their surface charge, and, more importantly, provides a neutral, hydrophilic steric barrier around the nanoparticle. This steric (stealth) barrier reduces both undesirable non-specific binding to, and uptake by, non-target cells, *in vivo*, as well as opsonization of the nanoparticle surface by serum proteins, which promotes elimination of the nanoparticle from the circulation by the mononuclear phagocyte system (MPS).[14] These crucial factors must be taken into account when designing a nanoparticle system for *in vivo* application, as failure to optimize surface PEGylation can adversely affect the biodistribution, and targeting efficacy of the nanoparticle by the above-mentioned factors. However, for the purpose of the present *in vitro* study, we optimized the surface PEGylation of our PAA-NPs with 2 kDa PEG – the minimum molecular weight of PEG required to evade elimination by the MPS *in vivo*[14] – in order to (i) accurately replicate the physicochemical

properties of the targeted nanoparticle that would be employed for *in vivo* applications, and (ii) eliminate their potential for non-specific cell binding, which would otherwise be a confounding factor in elucidating which endocytic pathway(s) mediate(s) internalization of the F3-targeted PAA-NPs. Direct conjugation of the heterobifunctional PEG molecules to the PAA-NP surface amine groups facilitated simultaneous reduction of the positive surface charge conferred by these amine groups, a positive charge that would otherwise inherently confer to the PAA-NPs a high non-specific binding affinity for the negatively-charged cell membranes. Following the reaction between a succinimidyl ester group of the heterobifunctional PEG molecule, and a surface amine group of the PAA-NP, the PEG chain is covalently linked, via a stable amide bond, to the nitrogen atom of the former amine group that participated in the reaction (Fig. 2.3). Hence, the reaction of PEG molecules with the surface amine groups concomitantly reduces the number of ionizable surface nitrogen atoms present on the surface of the PAA-NPs, thus leading to a reduction in positive charge of the PAA-NPs. Furthermore, as the flexible PEG molecules fold and adopt various conformations, they may also trap counter-anions close to the surface of the PAA-NPs, thus effectively "neutralizing" the positive charge of the protonated amine ($-NH_3^+$) groups. Figure 2.4 depicts the efficacy of our approach; we observed a progressive decrease in zeta potential of the PAA-NPs, from positive toward neutral, as the PAA-NP surface functionalization with heterobifunctional PEG increased, concomitant with a progressive and substantial reduction in non-specific cell binding to live MDA-MB-435 cells of the PEGylated PAA-NPs.

Once the surface PAA-NP PEGylation was optimized, the F3-targeted PAA-NPs were then synthesized from a fresh batch of PEGylated PAA-NPs that did not undergo Cys-capping, by covalently coupling the F3-Cys peptides, via their thiol groups, to the MAL termini of the PEG

crosslinkers. The coupling of the F3 peptides to the MAL termini of the highly flexible, 2 kDa PEG molecules places the targeting peptides further from the nanoparticle surface, thereby permitting a greater range of conformations that can be adopted by the targeting peptides, compared to the use of shorter, less-flexible crosslinkers, such as succinimidyl-4-(*N*-maleimidomethyl)-cyclohexane-1-carboxylate (SMCC), thus enhancing their ability to locate nucleolin receptors on the cell surfaces.[15] Interestingly, our recent two-photon microscopy study of subcellular pH in 9L glioma cells, using pH-sensitive F3-targeted and non-targeted, non-PEGylated PAA nanoparticles, revealed that the F3NPs, formulated with the crosslinker SMCC, evaded accumulation within lysosomes, while the NTNP counterparts were trafficked into lysosomes, under similar experimental conditions to those reported in the current study.[16] Taking into consideration that our PEGylated F3NPs similarly evaded trafficking to lysosomes in this current study, we deduce that the use of PEG as a crosslinker, which confers a greater conformational 'flexibility' to the surface conjugated F3 peptides, does not exert any observable influence on the subcellular localization of the F3NPs.

Importantly, as the surface functionalization of the PEGylated PAA-NPs with F3 peptides was increased, we observed a concomitant re-increase in NP zeta potential from ~0 mV (0 mg F3 peptide) to ~29 mV (11 mg F3 peptide/ 50 mg PEGylated PAA-NPs) (Fig. 2.5). This observation is indeed attributed to the multiple arginine and lysine residues of F3 peptide whose side-chain amines are positively charged at neutral pH. This re-increase in zeta potential was necessary such that the F3-targeted PAA-NPs have the same surface charge polarity as the non-targeted PAA-NPs, i.e. cationic, as the surface polarity of a NP, in addition to its hydrodynamic radius, is known to influence the endocytic mechanism via which it is internalized by a tumor cell, as discussed in further detail in Chapter 3. Hence, maintaining consistent physicochemical

properties (hydrodynamic radius and surface charge) between the NTNPs and F3NPs, as was done in this study, was crucial to accurately determining which endocytic pathway(s) were responsible for mediating the internalization of each type of NP (as performed in Chapter 3).

In the cellular sequestration assays performed with live 9L, MDA-MB-435, and MCF-7 cell lines, with the aim of optimizing the level of F3 peptide conjugated to the PEG steric barrier, in order to achieve maximal binding, a significant linear increase in cellular sequestration was observed up to 5.5 mg F3: 50 mg PAA-NP, with binding saturation occurring at 11 mg F3: 50 mg PAA-NP in both the 9L and MDA-MB-435 cell lines. The only exception was the MCF-7 cell line, in which F3NP cellular sequestration saturation was observed at 5.5 mg F3: 50 mg PAA-NP. These observations are consistent with the 'multivalency effect', whereby an increase in the number of cognate ligands on the surface of a nanoparticle, for a particular receptor, increases the avidity of the nanoparticle for its target cell. The saturation in cellular sequestration observed with the increase in surface coverage with F3 peptide, from 5.5 mg to 11 mg, is likely due to the fact that the number of F3 peptide ligands on the surface of the F3NP exceed the number of cell surface nucleolin receptors available within the contact surface area, between a single F3NP and the cell membrane to which they can bind.[17] An approximate 2.7: 1 cellular sequestration ratio (9L: MDA-MB-435) was maintained at each increment in PAA-NP surface coverage with F3 peptide (Fig. 2.7, Table 2.1). In contrast, the F3NP cellular sequestration ratios of both 9L: MCF-7 and MDA-MB-435: MCF-7 increased with each increment in the PAA-NP surface coverage with F3 peptide (Fig. 2.7, Table 2.1). These findings suggest that either (i) both 9L and MDA-MB-435 cells overexpress higher levels of cell surface nucleolin receptors, compared to MCF-7 cells, and/or (ii) 9L cells endocytose the F3NPs at a faster rate than that of both MDA-MB-435 and MCF-7 cells.

In view of the above, so as to exclude the influence of endocytosis on the observed F3NP cellular sequestrations, the experiments were repeated on paraformaldehyde-fixed and ATP-depleted cell lines, using the F3NP formulation that elicited cellular sequestration saturation under live cell conditions (11 mg F3: 50 mg PAA-NP) (Fig. 2.8, Table 2.2). These experiments revealed that endocytosis did indeed elevate the observed cellular sequestrations of the F3NPs in the live 9L and MDA-MB-435 cells. In fact, under both paraformaldehyde-fixed and ATP depleted conditions, slightly lower F3NP cellular sequestrations were observed for the 9L cells than that for the MDA-MB-435 cells although not statistically significant, while the MCF-7 cells still exhibited negligible F3NP cellular sequestrations, under both cytostatic treatments (Fig. 2.8, Table 2.2). Slightly higher F3NP cellular sequestrations were observed in ATP-depleted cells relative to paraformaldehyde-fixed cells (approximately 1.7 fold difference), which can be attributed to the fact that 2,4-dinitrophenol inhibits only the mitochondrial production of ATP, and not the production of ATP by the glycolysis pathway. Hence, there remains a basal level of ATP production by glycolysis, which can support a residual level of endocytosis, whereas paraformaldehyde fixation completely arrests all cellular activity, including endocytosis. Nonetheless, these cytostatic treatments indicate that, although the 9L and MDA-MB-435 cells do not have significantly different cell surface nucleolin expression levels from each other, they both express significantly higher cell surface nucleolin levels than MCF-7 cells. The similarity between nucleolin surface expression levels in the 9L and MDA-MB-435 cell lines therefore explains why saturation of F3NP cellular sequestration was achieved for both the 9L and MDA-MB-435 cell lines at about the same level of surface PAA-NP coverage with F3 peptide. In addition, this supports our premise that the 9L cells *endocytose* the F3NPs at considerably higher rates than both the MDA-MB-435 and MCF-7 cell lines.

According to Hovanessian *et al.*, surface expressed nucleolin is constantly induced in tumor cells, to mediate the internalization of ligands that promote tumorigenesis.[18] In turn, the rate of nucleolin-mediated internalization is dictated by the metabolic rate of the specific tumor cell type. Based on our cell culture experiments, 9L cells replicate considerably faster than MDA-MB-435 and MCF-7 cells, which in turn has to be supported by a higher metabolic rate. Given that endocytosis is an ATP-dependent process, as well as the dramatic reduction in the cellular sequestration of the F3NPs for 9L cells elicited by both cytostatic treatments, it is therefore reasonable to deduce that the more metabolically active 9L cells endocytose cell membrane-bound F3NPs faster than either MDA-MB-435 and MCF-7 cells. We therefore deduce that the consistent 2.7-fold greater cellular sequestration of the F3NPs for the 9L cells, relative to the MDA-MB-435 cells in the live cellular sequestration assay (Fig. 2.7, Table 2.1), can be accounted for by the higher endocytic rate of the 9L cells. This result reaffirms that the cell surface receptors are inextricably linked to the endocytic machinery of the cell, and underscores the importance of tailoring a nanoparticle to the target cell type, in order to maximize the efficacy of chemotherapy (or activated imaging). Furthermore, the implication of this observation is that, by using an appropriately targeted nanoparticle, one could achieve higher intracellular concentrations of a chemotherapeutic drug within a given period of time, in highly aggressive malignant cells, by exploiting their faster endocytic rates, relative to the ordinary diffusion of free drug across the cell membranes of malignant cells from the bloodstream.

2.6 Conclusion

Collectively, these findings reveal that while there is negligible difference in the surface nucleolin receptor density between the 9L and MDA-MB-435 cell lines, the former endocytoses F3NPs at a faster rate than that of MDA-MB-435 cells. In contrast, the MCF-7 cells demonstrated consistently weaker F3NP cellular sequestrations, relative to the 9L and MDA-MB-435 cell lines, under both paraformaldehyde-fixed and ATP-depleted conditions, indicating that MCF-7 cells express a lower surface density of nucleolin receptors and/or exhibit a slower rate of endocytosis (Fig. 2.8). In light of the above findings, the MCF-7 cell line was omitted from the endocytosis inhibition and immunocytochemistry experiments, as discussed in Chapter 3. Furthermore, the 11 mg F3 peptide: 4 mg PEG: 50 mg PAA-NP formulation, which exhibited saturated cellular sequestration (binding + uptake) in both the 9L and MDA-MB-435 cell lines, was selected for studying the intracellular trafficking of the F3-targeted PAA-NPs in these cell lines.

2.7 Experimental Section

2.7.1 Optimization of PAA-NP Surface PEGylation

Amine-surface functionalized FITC-labeled PAA nanoparticles were synthesized as described in Chapter 3. Thereafter, 50 mg lyophilized FITC-labeled PAA-NP was dissolved in 2.5 mL PBS buffer (pH 7.4) and sonicated until the solution turned transparent, to which either 0.4, 2 or 4 mg heterobifunctional PEG crosslinker (SCM-PEG-MAL) was added, and the mixture stirred continuously for 30 min at room temperature. Following washing using an Amicon centrifugal filter (Millipore, 100 kDa molecular weight cut-off), the various PEGylated PAA-NP formulations were reacted with L-cysteine (62.5 μL, 10 $mg.mL^{-1}$) for 2 hours at room

temperature to cap the maleimidyl ester groups of the PEG crosslinkers so as to prevent their reaction with cell surface thiols in subsequent cell-based assays aimed at determining their potential for non-specific cell binding. The PEGylated PAA-NPs were then washed five times with PBS (pH 7.4) using an Amicon centrifugal filter (100 kDa molecular weight cut-off) at 5000 *xg* for 20 minutes, and the various PEGylated PAA-NP formulations resuspended in PBS (pH 7.4) to a final volume of 5 mL. The zeta potentials of the non-PEGylated and various PEGylated PAA-NP formulations were determined as described in the experimental section of Chapter 3. Thereafter, the non-PEGylated and various PEGylated PAA-NP formulations were incubated with MDA-MB-435 cells (seeded in 8-chambered multiwell microscopy coverslides; ~100, 000 cells per well) to a final concentration of 0.1 $mg.mL^{-1}$ in DMEM supplemented with 10% Fetal Bovine Serum and 1% PSG for 1 hour at 37 °C in 5% CO_2 atmosphere. After incubation, the culture media containing unbound non-PEGylated or PEGylated PAA-NPs were aspirated from the wells and the cells washed three times with warm DPBS (pH 7.4). The wells were replenished with colorless DMEM medium, and the cells imaged on an Olympus inverted confocal microscope using a 40x objective lens with 488 nm excitation. All images were captured under identical exposure times based on the fluorescence emission of the FITC-labeled PAA-NPs. The degree of non-specific cell binding and internalization of the non-PEGylated and PEGylated PAA-NP formulations was determined by measuring the FITC fluorescence emission intensity from multiple cells in each confocal plane using Metamorph software (Molecular Devices). All values are reported as means from three independent experiments.

2.7.2 Optimization of Surface Functionalization of PEGylated PAA-NPs with F3 peptide

Fresh batches of PEGylated PAA-NPs (4 mg SCM-PEG-MAL: 50 mg FITC-PAA-NPs) were prepared as described above, however with omission of the Cys-capping stepping of the MAL groups on the PEG crosslinkers. After washing to remove unbound PEG crosslinkers, separate batches of surface PEGylated PAA-NPs were reacted with different quantities of F3-Cys peptide (2.2, 5.5 or 11 mg), and the conjugation reaction allowed to run overnight at room temperature. The reaction between the thiol group of the carboxy terminal cysteine of the F3 peptide moieties, and the maleimidyl ester terminus of the PEG crosslinkers facilitated covalent conjugation of the F3 peptide moieties to the PEG crosslinkers already conjugated to the PAA-NP surfaces. The F3 surface functionalized PEGylated PAA-NPs (F3NPs) were subsequently incubated with 1.74 mg (10 mg.mL^{-}1) of L-cysteine for 2 hours at room temperature to cap any unreacted maleimidyl ester groups. Thereafter, the different F3NP batches were washed five times with PBS (pH 7.4) using an Amicon centrifugal filter (100 kDa molecular weight cut-off) at 4000 x*g* for 20 minutes and the final volume adjusted to 5 mL with PBS (pH 7.4). The zeta potentials of the various F3NP formulations were determined as described in the experimental section of Chapter 3. The filtered nanoparticles were kept frozen at -20 °C until use.

Live cell assays: The MCF-7, MDA-MB-435 and 9L cell lines were seeded in separate 8-chambered multiwell microscopy coverslides (~ 140, 000 cells per well) in their respective complete culture media, and allowed to attached overnight at 37 °C. The following day, the cells were treated with the various F3NP formulations at a final concentration of 0.1 mg.mL^{-1} for 1 hour at 37 °C. Thereafter, any unbound F3NPs were rinsed away by three changes of culture medium. The wells were replenished with colorless culture media, and confocal imaging of the F3NP-treated cell lines was performed directly from the multi-well coverslides on an Olympus

inverted confocal microscope using a 40x objective lens with 488 nm excitation. Images were captured under identical exposure times based on the fluorescence emission of the FITC-labeled F3NPs. The F3NP cellular sequestrations were quantified by measuring the pixel intensity of each cell from the obtained confocal images using Metamorph software (Molecular Devices). All values are reported as means from three independent experiments.

Fixed and ATP-depleted cell assays: The above experiments were repeated on paraformaldehyde (PFA)-fixed and ATP-depleted cells in order to obviate the influence of endocytosis on the cellular sequestration of the F3NPs in each cell line. This involved either (1) fixing the cells with 4 % (v/v) phosphate-buffered paraformaldehyde (pH 7.4) for 10 minutes at room temperature or (2) pre-treating the cells with 2,4-dinitrophenol (2,4-DNP, 1 mM) for 30 minutes at 37 °C to inhibit mitochondrial ATP-production, prior to incubating the cells with the F3NPs. The 11 mg F3: 50 mg PAA-NP F3NP formulation, at which cellular sequestration reached saturation in the live cell assays under above incubation conditions, was used for the fixed and ATP-depleted cell assays. Confocal imaging of the F3NP-treated cell lines in both assays was performed as for the live cells assays. These assays were repeated three times.

References

1. M. Lundqvist, J. Stigler, G. Elia, I. Lynch, T. Cedervall, and K. A. Dawson, *Proc. Natl. Acad. Sci. U. S. A.*, 2008, **105**, 14265–70.
2. S. M. Moghimi and H. M. Patel, *Biochim. Biophys. Acta*, 1989, **984**, 379–83.
3. S. M. Moghimi, A. C. Hunter, and J. C. Murray, *Pharmacol. Rev.*, 2001, **53**, 283–318.
4. G. R. Reddy, M. S. Bhojani, P. McConville, J. Moody, B. A. Moffat, D. E. Hall, G. Kim, Y.-E. L. Koo, M. J. Woolliscroft, J. V Sugai, T. D. Johnson, M. a Philbert, R. Kopelman, A. Rehemtulla, and B. D. Ross, *Clin. Cancer Res.*, 2006, **12**, 6677–86.
5. E. Ruoslahti, S. N. Bhatia, and M. J. Sailor, *J. Cell Biol.*, 2010, **188**, 759–68.
6. H. Gao, W. Shi, and L. B. Freund, *Proc. Natl. Acad. Sci. U. S. A.*, 2005, **102**, 9469–74.
7. H. J. Hah, G. Kim, Y.-E. K. Lee, D. A. Orringer, O. Sagher, M. A. Philbert, and R. Kopelman, *Macromol. Biosci.*, 2011, **11**, 90–9.

8. H. H. Hooper, J. P. Baker, H. W. Blanch, and J. M. Prausnitz, *Macromolecules*, 1990, **23**, 1096–1104.
9. F. Gu, L. Zhang, B. a Teply, N. Mann, A. Wang, A. F. Radovic-Moreno, R. Langer, and O. C. Farokhzad, *Proc. Natl. Acad. Sci. U. S. A.*, 2008, **105**, 2586–91.
10. D. R. Elias, A. Poloukhtine, V. Popik, and A. Tsourkas, *Nanomedicine*, 2012, 1–8.
11. H. Yuan and S. Zhang, *Appl. Phys. Lett.*, 2010, **96**, 033704.
12. H. Yuan, C. Huang, and S. Zhang, *PLoS One*, 2010, **5**, e13495.
13. A. Fakhari, A. Baoum, T. J. Siahaan, K. B. Le, and C. Berkland, *J. Pharm. Sci.*, 2011, **100**, 1045–56.
14. D. E. Owens and N. a Peppas, *Int. J. Pharm.*, 2006, **307**, 93–102.
15. J.-H. Park, G. von Maltzahn, L. Zhang, A. M. Derfus, D. Simberg, T. J. Harris, E. Ruoslahti, S. N. Bhatia, and M. J. Sailor, *Small*, 2009, **5**, 694–700.
16. A. Ray, Y.-E. Koo Lee, T. Epstein, G. Kim, and R. Kopelman, *Analyst*, 2011, **136**, 3616–22.
17. H. Yuan, J. Li, G. Bao, and S. Zhang, *Phys. Rev. Lett.*, 2010, **105**, 1–4.
18. A. G. Hovanessian, C. Soundaramourty, D. El Khoury, I. Nondier, J. Svab, and B. Krust, *PLoS One*, 2010, **5**, e15787.

Chapter 3

Modulation of Hydrogel Nanoparticle Intracellular Trafficking by Multivalent Surface Engineering with Tumor Targeting Peptide

This chapter has been adapted with minor modification from the following published article:

L. Karamchand *et al.,* Modulation of Hydrogel Nanoparticle Intracellular Trafficking by Surface Engineering with Tumor Targeting Peptide. Nanoscale, 2013; 5(21): 10327-44

3.1 Introduction

Targeted multifunctional nanocarriers are generally nanoparticles with integrated, multivalent tumor-targeting moieties, diagnostic-imaging agents and therapeutic components, which, in combination, facilitate *in vivo* theranostics, with the aim of overcoming the specificity and efficacy limitations of conventional cancer diagnostic and therapeutic approaches.[1,2] Successful integration of these chemically diverse entities within a single nanoparticle, while retaining their respective biochemical/biophysical properties, requires a highly versatile, yet stable and biocompatible matrix. The first described multifunctional, multivalent nanocarriers were based on the synthetic polymeric hydrogel matrix, polyacrylamide (PAA), which easily facilitates multifunctionality due to its chemical flexibility.[3–7] In the last decade, both natural and synthetic polymeric hydrogels have emerged as promising nanoplatforms for the development of biocompatible targeted multifunctional nanocarriers.[8] This is enabled by the special properties of

hydrogels, *namely,* hydrophilicity,[9] low cytotoxicity,[10] biodegradability,[11–14] capacity for high-density co-encapsulation of multiple payload types, including a broad range of drugs,[15] contrast agents for biomedical imaging,[3–8,16–18] biosensing probes, [19–21] and photosensitizer chemicals for photodynamic therapy,[4–8,22–24] while simultaneously protecting their payloads against chemical/enzymatic degradation.[25] Another attractive feature of polymeric hydrogel nanocarriers is their engineerability for controlled release in response to a broad range of stimuli,[26] which permits their 'tuning' to the physiological environment of tumors, for optimal drug release. A question underlying this work is whether nano-drugs with their multiple targeting ligands can overcome cellular multi-drug resistance (MDR) faced by single molecule drugs using the very same targeting ligands.

Optimal drug release from chemically-responsive, controlled-release hydrogel nanocarriers, in particular, which are engineered to liberate their therapeutic payloads in response to a specific intracellular stimulus, such as pH,[27] glutathione[28,29] or lysosomal enzymes,[30] is predicated on their 'directive targeting' to the appropriate subcellular compartment. This is dependent on the endocytic pathway via which the target cell initially internalizes the hydrogel nanocarrier, and in turn, has direct bearing on the efficacy of the drug in its target tumor cell. In non-phagocytic cells, the major endocytic pathways that mediate the internalization of nanocarriers include the clathrin-mediated, caveolae-mediated and macropinocytosis pathways.[31] Nanocarriers that are internalized via either the clathrin-mediated or macropinocytosis pathways ultimately accumulate within lysosomes (degradative, acidic vesicles), whereas those internalized via caveolae-mediated endocytosis typically accumulate within non-degradative vesicles of neutral pH, known as caveosomes. Recent studies have demonstrated that the internalization and intracellular trafficking of a hydrogel nanocarrier is influenced by its ensemble of unique

physicochemical properties, namely; size,[32–34] morphology,[35,36] elasticity of the hydrogel matrix,[37] and surface charge.[38–40] In addition to these physicochemical parameters, the surface engineering of a hydrogel nanocarrier with targeting ligands that bind selectively to specific receptors, which are overexpressed exclusively on the cell membrane of tumor and/or tumor endothelial cells, also influences the internalization and, subsequently, the intracellular trafficking of the nanocarrier. This strategy of nanocarrier 'molecular addressing' serves to enhance the nanocarrier's binding affinity for, and internalization by, the target tumor/endothelial cell, while relying on the assumption that the ligand-bearing nanocarrier will be internalized and trafficked along the same endocytic pathway as the ligand alone.

Targeting of drug-laden nanocarriers to cell surface receptors that are overexpressed on the surface of tumor and/or tumor endothelial cells, with the specific capacity of translocation into the nucleus, is especially crucial to the efficacy of chemotherapeutic drugs whose site of action is in the nucleus. Nucleolin, a nucleolar phosphoprotein that possesses a bipartite nuclear localization signal (NLS),[41] is such a receptor that is overexpressed on the surface of tumor endothelial cells, as well as on some other types of tumor cells.[42] Nucleolin has already been exploited for the targeted *in vivo* delivery of multifunctional PAA hydrogel nanocarriers to tumors in which it is overexpressed.[7,43] This has been achieved using the F3 peptide, a 32 amino acid sequence (KDEPQRRSARLSAKPAPPKPEPKPKKAPAKKC),[44] as the nucleolin-targeting ligand. However, an important consideration in the NLS receptor-mediated transport of nanocarriers/nanoparticles into the nucleus is the size-restriction imposed by the nuclear pore complexes (~40 nm) on the entry into the nucleus of cargo that exceeds this size-restriction,[45] as well as the intracellular fate of such ligand-targeted nanocarriers/nanoparticles. Recent studies in our lab on nucleolin-overexpressing cell lines, involving two-photon microscopy analysis of F3-

targeted and non-targeted, pH-sensing PAA nanocarriers (68 nm) and silver core/PAA shell nanocarriers (90 nm and 130 nm), revealed that, although the F3-targeted PAA nanocarriers were not transported into the nuclei, they were instead sequestered within membrane-bound vesicles, but did not accumulate within lysosomes, whereas non-targeted PAA nanocarriers accumulated within lysosomes.[46,47] This observation led us to pose the question, which forms the basis of this present study: *How transferable is the intracellular targeting property of the F3 peptide to a hydrogel nanocarrier surface functionalized with this ligand?* Remarkably, we observed that while the inhibition of clathrin-mediated endocytosis promoted the internalization of the untethered, monovalent F3 peptides and their translocation into the nucleus, the inhibition of this pathway instead strongly inhibited the internalization of the F3-targeted PAA nanocarriers. Furthermore, in the absence of inhibitors of the clathrin endocytic pathway, the untethered, monovalent F3 peptides normally accumulate within lysosomes without translocation to the nuclei, whereas the F3-targeted PAA nanocarriers accumulate within endosome-type vesicles, *but evades trafficking to the lysosomes*. This novel finding suggests that the coupling of multiple F3 peptides to the surface of the PAA nanocarrier, i.e. its multivalency, significantly alters the intracellular trafficking property of the peptide, and underscores the importance of not assuming that a ligand-bearing nanocarrier will follow the same intracellular trafficking pathway as that of the ligand alone. To the best of our knowledge, this study constitutes the first attempt at *elucidating the influence exerted by the F3 peptide surface functionalization of a nanocarrier/nanoparticle on both its internalization and intracellular trafficking in tumor cells.* Furthermore, we believe that the approach presented here will also be applicable to elucidate the endocytosis and intracellular trafficking pathways employed by nanocarriers functionalized with other targeting moieties, aimed at other cell surface-expressed proteins, with the goal of

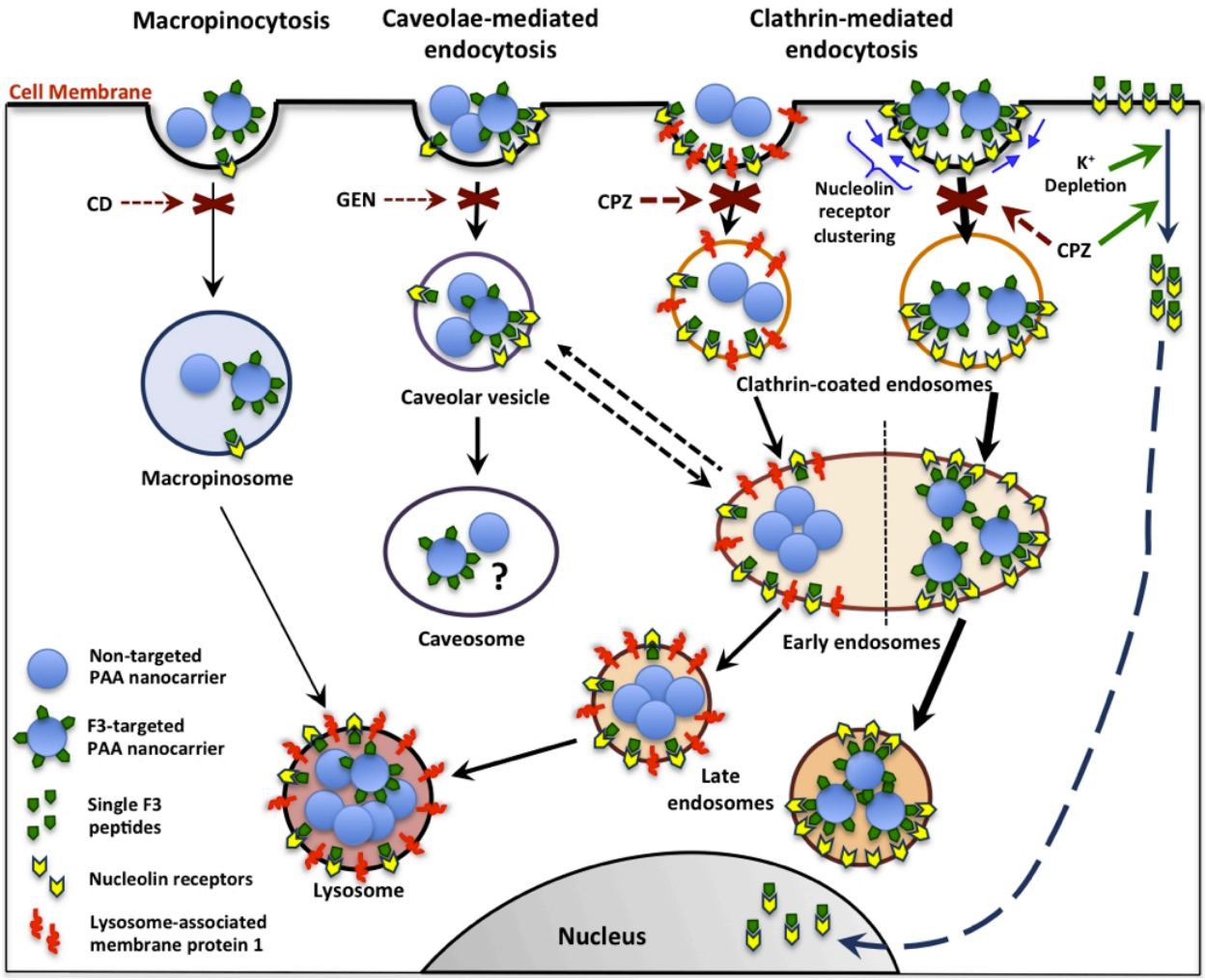

Fig. 3.1 Schematic summary of the endocytic pathways of internalization for F3 peptide, non-targeted and F3-targeted PAA nanocarriers (NTNCs and F3NCs) in the nucleolin-overexpressing MDA-MB-435 cell line. The F3NCs are predominantly internalized via the clathrin-mediated endocytic pathway, denoted by the potent inhibition of their internalization by Chlorpromazine (CPZ). In addition, the F3NCs employ a mechanism that circumvents their trapping within the degradative lysosomes; rather they accumulate within vesicles devoid of LAMP1 protein (Lysosome-associated membrane protein 1) in the perinuclear space. The caveolae-mediated and macropinocytosis endocytic pathways also contribute to the internalization of the F3NCs, but to a lesser extent than the clathrin-mediated pathway. In contrast, single, monovalent F3 peptides are normally trafficked to lysosomes following internalization. However, inhibition of the clathrin-mediated endocytic pathway, by both CPZ and Potassium depletion, promotes the direct translocation of F3 peptides into the nucleus. The clathrin-mediated and caveolae-mediated endocytic pathways contribute approximately equally to the internalization of the NTNCs, while macropinocytosis mediates their internalization to a lesser extent. Notably, the NTNCs co-internalize with LAMP1 proteins from the cell surface following which they are trafficked to lysosomes, as denoted by the intense colocalization between the NTNCs and LAMP1 proteins (~50%) compared to the significantly lower colocalization between the F3NCs and LAMP1 (~8%). Given the similarities observed between the MDA-MB-435 and 9L cell lines with respect to the endocytosis inhibition and Lysotracker Red colocalization profiles of the F3 peptides, NTNCs and F3NCs, this scheme also applies to the 9L cell line, and, presumably, to other cell types expressing high levels of Nucleolin on their cell membranes.

overcoming the multidrug resistance of cancer cells. We present here the overall result in schematic form (as suggested by a reviewer), so as to assist the reader with following the details of the study that lead to this conclusion (see Fig. 3.1).

3.2 Results and Discussion

3.2.1 Endocytic Inhibition of Nanocarrier Internalization in Nucleolin-overexpressing cell lines

Different endocytic pathways, particularly clathrin-mediated and caveolae-mediated endocytosis and macropinocytosis, have been implicated in the cellular internalization of nanocarriers, depending on the physicochemical properties of the nanocarrier.[31] Given the influence of a hydrogel nanocarrier's physicochemical properties on its cellular internalization, we employed an F3-targeted PAA hydrogel nanocarrier (F3NC), which is similar to that of an unmodified, *non-targeted* PAA hydrogel nanocarrier (NTNC) in terms of physicochemical properties, i.e. size and surface charge (see Chapter 2). We employed the inhibitors, chlorpromazine (CPZ), genistein (GEN) and cytochalasin D (CD), which specifically disrupt the above-mentioned endocytic pathways, respectively, and compared the behavior of the multivalent FITC-labeled F3NCs, under the same conditions, with that of the FITC-labeled NTNCs and FITC-labeled monovalent, molecular F3 peptides (molecular-F3 peptides), in separate cultures of live 9L and MDA-MB-435 cells. These cells are known to overexpress nucleolin receptors at their surfaces. The additional labeling of the lysosomes with a pH-sensitive fluorophore, Lysotracker Red DND-99, permitted simultaneous assessment of whether the fluorescent F3NCs, NTNCs and molecular-F3 peptides accumulate within lysosomes, in the absence or presence of any of the

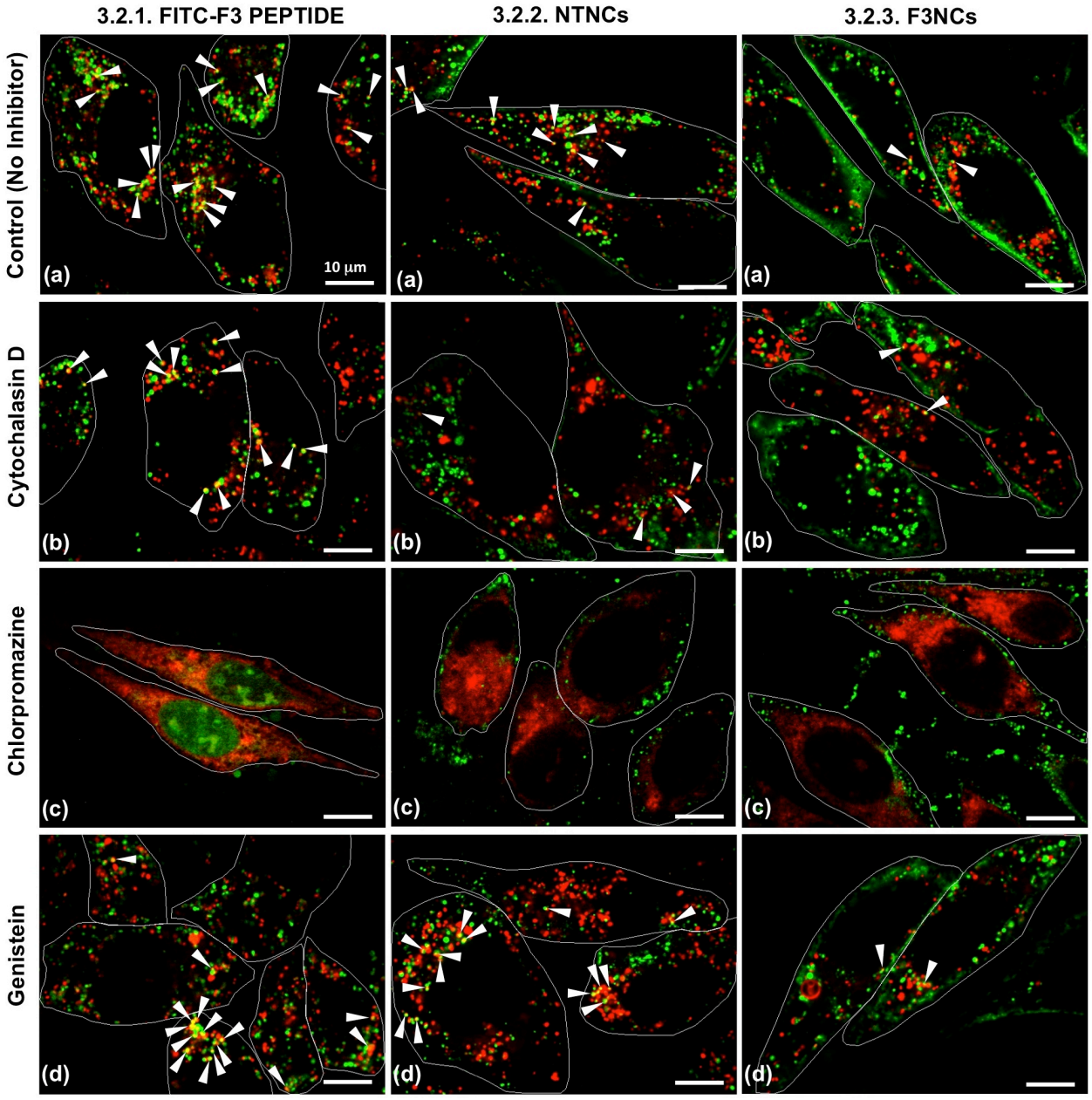

Fig 3.2 Identification of the endocytic pathway(s) that mediate internalization of single F3 peptides **(green; 3.2.1.a-d),** non-targeted PAA nanocarriers **(NTNCs; green; 3.2.2.a-d),** and F3-targeted PAA nanocarriers **(F3NCs; green; 3.2.3.a-d)** in the 9L rat gliosarcoma cell line with the endocytic inhibitors Cytochalasin D (macropinocytosis inhibitor), Chlorpromazine (clathrin-mediated endocytosis inhibitor), and Genistein (caveolae-mediated endocytosis inhibitor). Controls constituted 9L cell cultures that received either F3 peptides, NTNCs or F3NCs in the absence of endocytic inhibitors **(3.2.1.a, 3.2.2.a and 3.2.3.a).** Lysosomes (red) were labeled with the pH-sensitive fluorophore Lysotracker DND-99. Regions of yellow/orange fluorescence denote colocalization between lysosomes and either F3 peptides, NTNCs or F3NCs, as indicated by white arrowheads. Scale bar: 10 µm

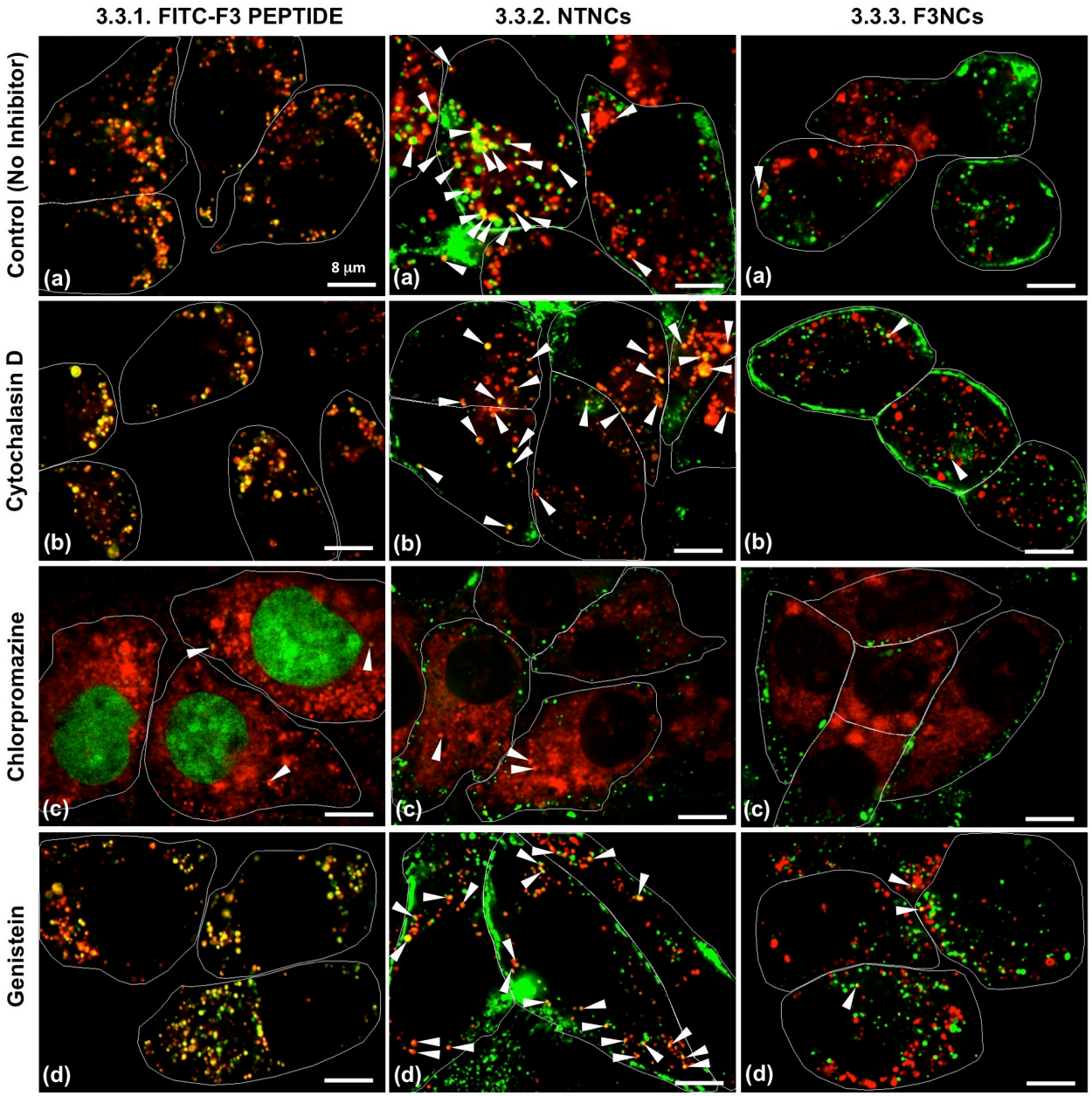

Fig 3.3 Identification of the endocytic pathway(s) that mediate internalization of single F3 peptides **(green; 3.3.1.a-d),** NTNCs **(green; 3.3.2.a-d)**, and F3NCs; **(green; 3.3.3.a-d)** in the MDA-MB-435 human breast adenocarcinoma cell line with the endocytic inhibitors Cytochalasin D, Chlorpromazine, and Genistein. Controls constituted MDA-MB-435 cell cultures that received either F3 peptides, NTNCs or F3NCs in the absence of endocytic inhibitors **(3.3.1.a, 3.3.2.a and 3.3.3.a).** Lysosomes (red) were labeled with the pH-sensitive fluorophore Lysotracker DND-99. Regions of yellow/orange fluorescence denote colocalization between lysosomes and either F3 peptides, NTNCs or F3NCs, as indicated by white arrowheads. Scale bar: 8 μm

endocytosis inhibitors. All confocal images were analyzed according to three criteria, namely, (i) the degree of cellular uptake, (ii) the degree of colocalization with Lysotracker Red and, (iii) the absence or presence of nuclear accumulation of molecular-F3 peptides/ NTNCs/ F3NCs.

Interestingly, neither of the inhibitors completely blocked the endocytosis of molecular-F3 peptide, in both 9L and MDA-MB-435 cell lines. While both CD and GEN elicited comparably low levels of inhibition (~20-30%) on the internalization of molecular-F3 peptide, CPZ instead enhanced the internalization of molecular-F3 peptide in both cell lines, relative to the untreated controls (Figs. 3.4.1 and 3.4.2). Furthermore, CPZ promoted prominent accumulation of molecular-F3 peptide in the nuclei of both 9L (Fig. 3.2.1.c) and MDA-MB-435 (Fig.3.3.1.c) cells, with the accumulation of molecular-F3 peptide being highest in the nucleolar regions of the nuclei. Potassium depletion, a potent non-pharmacological inhibitor of clathrin-mediated endocytosis, also promoted prominent nuclear accumulation of molecular-F3 peptide, in both the 9L and MDA-MB-435 cells (Appendix A3.1). However, molecular-F3 peptide was not observed in the nuclei of the control, CD- or GEN-treated 9L (Figs. 3.2.1.a, b, d) and MDA-MB-435 cells (Figs. 3.3.1.a, b, d). Colocalization (yellow/orange fluorescent punctate foci) between molecular-F3 peptide (green) and Lysotracker Red was observed in the control (no inhibitors), CD- and GEN-treated 9L (Figs. 3.2.1.a, b, d) and MDA-MB-435 (Figs. 3.3.1.a, b, d) cells, although the degree of colocalization in MDA-MB-435 cells (~90%, Fig. 3.5.2) was markedly greater than that in 9L cells (~35%, Fig. 3.5.1). However, in both CPZ-treated 9L and MDA-MB-435 cells (Figs. 3.2.1.c and 3.3.1.c), the degree of colocalization between molecular-F3 peptide and Lysotracker Red was markedly lower (7.2 % and 3.5 % respectively) than in the control, CD- and GEN-treated cells (Figs. 3.5.1. and 3.5.2.).

In contrast to the observations for the molecular-F3 peptide, both CPZ and GEN elicited

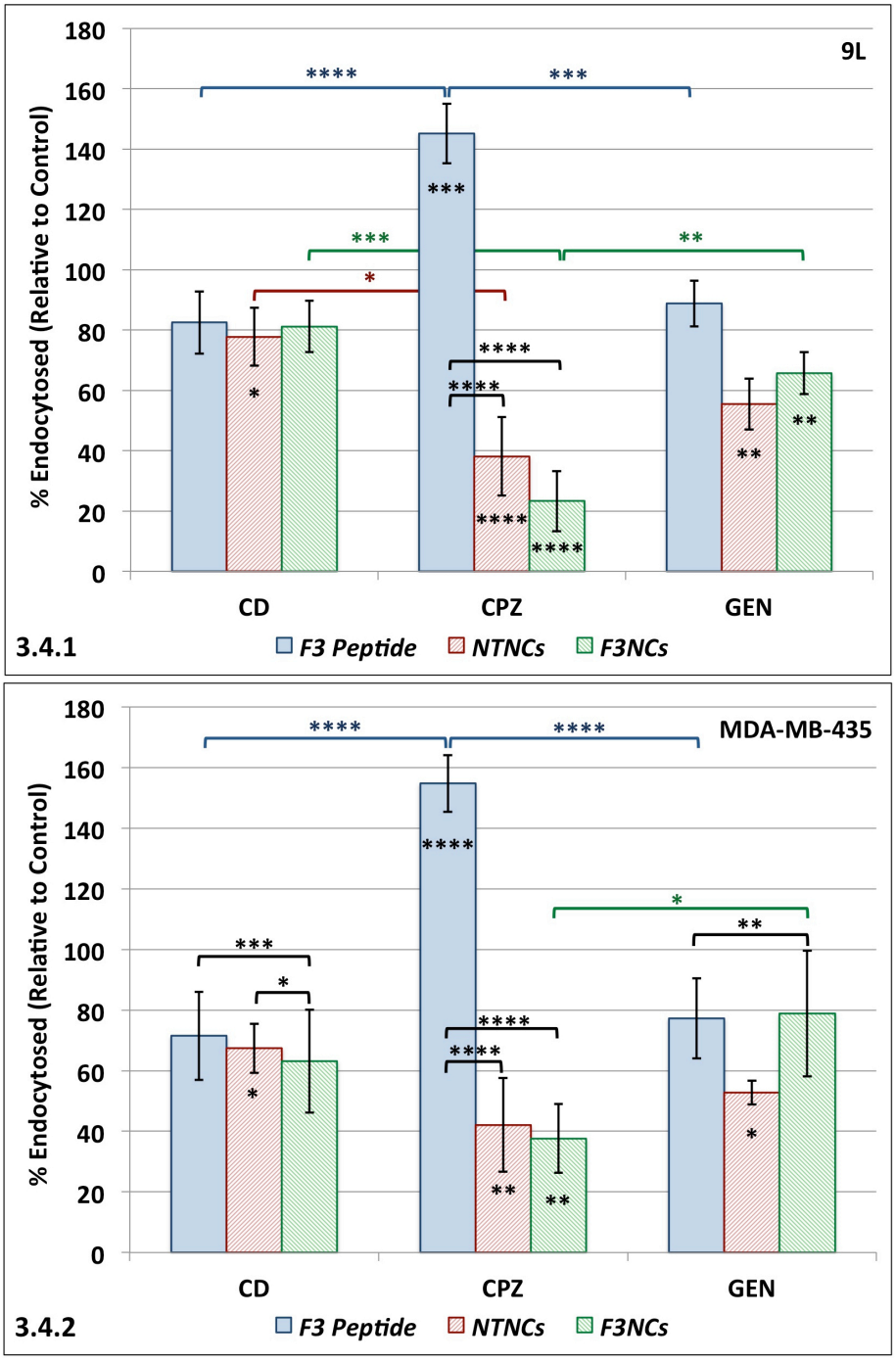

Fig 3.4 Comparison of the influence of the endocytic inhibitors, Cytochalasin D (CD), Chlorpromazine (CPZ) and Genistein (GEN) on the internalization of the F3 peptides, NTNCs and F3NCs in the 9L **(3.4.1)** and MDA-MB-435 cell lines **(3.4.2).** Mean intracellular fluorescence intensities of the F3 peptides, NTNCs and F3NCs in each inhibitor treatment are expressed as percentages relative to the mean fluorescence intensities of their respective control cells, which were not treated with the inhibitors, in each cell line. Error bars show standard deviations. P-values are indicated as follows: $P<0.05$ (*); $P<0.01$ (**); $P<0.001$ (***); $P<0.0001$ (****). Brackets are color-coded to denote significant differences in uptake of F3 peptide (blue), NTNCs (red) and F3NCs (green) across different inhibitor treatments. Black brackets denote significant internalization differences between F3 peptide, NTNCs and F3NCs within the same inhibitor treatment. Asterisks indicated directly on bars denote significant difference from their respective controls (with no inhibitors).

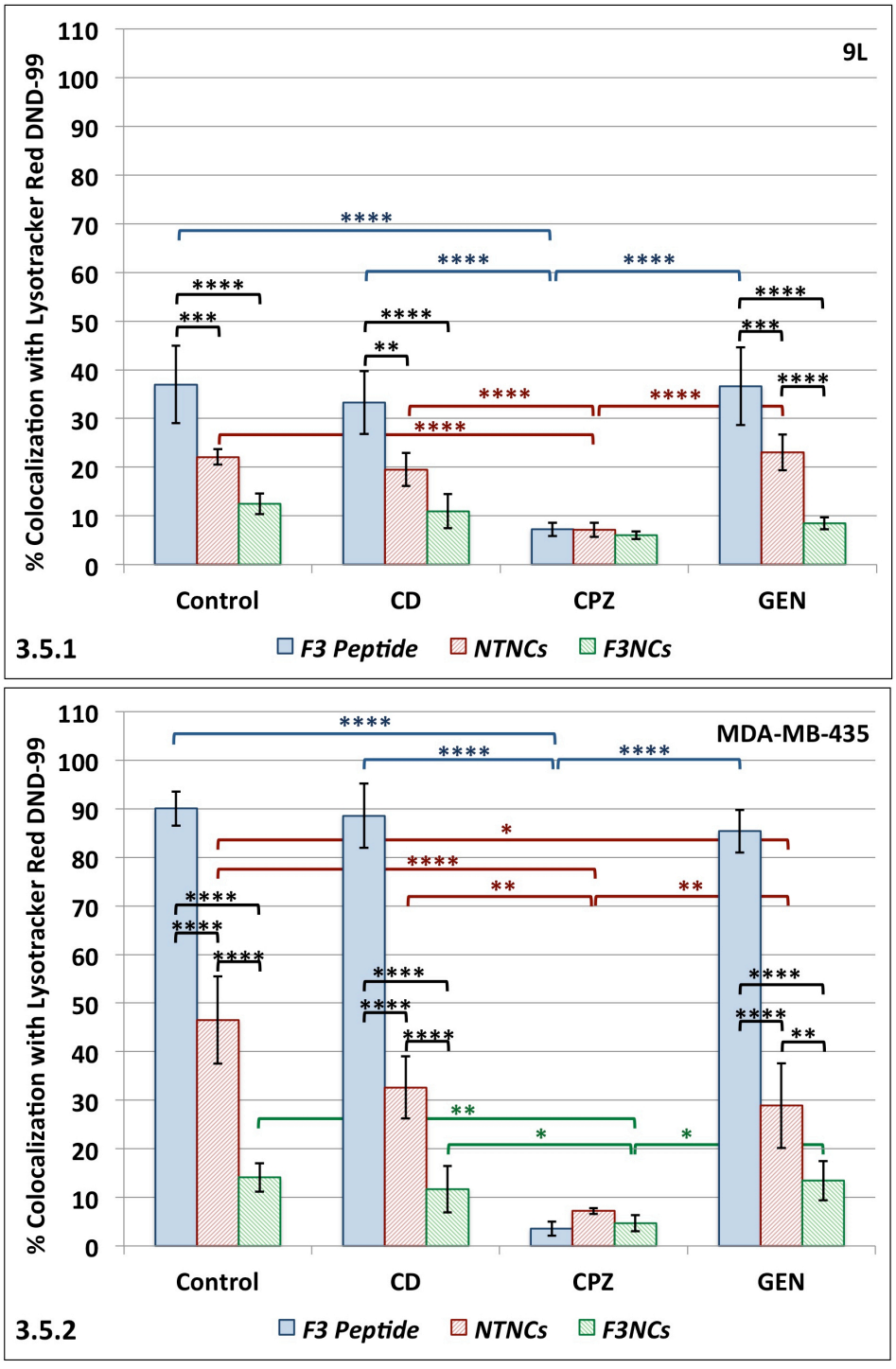

Fig 3.5 Comparison of the influence of the endocytic inhibitors, CD, CPZ and GEN on the degree of colocalization of the F3 peptides, NTNCs and F3NCs with Lysotracker Red DND-99 in the 9L **(3.5.1)** and MDA-MB-435 **(3.5.2)** cell lines. All values are based on the Manders' M_2 colocalization coefficients expressed as mean percentages. Errors bars show standard deviations. P-values are indicated as follows: $P<0.05$ (*); $P<0.01$ (**); $P<0.001$ (***); $P<0.0001$ (****). Brackets are color-coded to denote significant differences in colocalization of F3 peptide (blue), NTNCs (red) and F3NCs (green) with Lysotracker Red DND-99 across different inhibitor treatments. Black brackets denote significant colocalization differences between F3 peptide, NTNCs and F3NCs within the same inhibitor treatment.

marked reductions in the internalization of the NTNCs in both cell lines; 38.1% and 55.5% internalization respectively for 9L cells (Fig. 3.4.1), and 42.1% and 52.8% internalization respectively for MDA-MB-435 cells (Fig. 3.4.2). The greater inhibitory effect of CPZ on the internalization of the NTNCs is evident from the NTNCs being confined mostly to the cell peripheries (Figs. 3.2.2.c and 3.3.2.c). In both cell lines, CD exerted a lower inhibitory effect on the internalization of the NTNCs, which was similar to the level of inhibition exerted on the internalization of molecular-F3 peptide in the respective cell lines (Figs. 3.4.1 and 3.4.2). Importantly, over the duration of the experiment (2-3 hours), the NTNCs did not enter the nuclei of the controls (Figs. 3.2.2.a and 3.3.2.a) or any of the endocytosis-inhibitor treatments, in either of the cell lines (Figs. 3.2.2.b-d and 3.3.2.b-d). The degree of colocalization between the NTNCs and Lysotracker Red was 2-fold higher in the MDA-MB-435 control cells (46.5%) than in the 9L control cells (22.1%) (Figs. 3.5.1 and 3.5.2). All endocytic inhibitors decreased the degree of colocalization between the NTNCs and Lysotracker Red, relative to the control, in MDA-MB-435 cells, whereas only CD and CPZ decreased the degree of colocalization between the NTNCs with Lysotracker Red, relative to the control, in 9L cells. Nonetheless, the degree of NTNC-Lysotracker Red colocalization in CD- and GEN-treated MDA-MB-435 cells remained higher than the corresponding inhibitor treatments in the 9L cells. Notably, CPZ was the most potent inhibitor in reducing the colocalization between the NTNCs and Lyostracker Red in both cell lines; 7.1% and 7.2% colocalization for the 9L and MDA-MB-435 cells, respectively (Figs. 3.5.1 and 3.5.2).

As observed for the NTNCs, F3NC internalization was most potently inhibited by CPZ in both the 9L (23.3%; Figs. 3.2.3.c and 3.4.1) and MDA-MB-435 cells (37.7%; Figs. 3.3.3.c and 3.4.2). Notably, F3NC internalization in both CPZ-treated cell lines were lower than, although

not significantly different from, NTNC internalization in the CPZ-treated 9L (38.1%) and MDA-MB-435 (42.1%) cells. In contrast, F3NC internalization in the GEN-treated 9L (65.7%) and MDA-MB-435 (78.9%) cells were higher than NTNC internalization in the GEN-treated 9L (55.5%) and MDA-MB-435 (52.8%) cells (Figs. 3.34.1 and 3.4.2). Interestingly, F3NC internalization was lower in CD-treated MDA-MB-435 cells (63.1%) than CD-treated 9L cells (81.2%), although these levels of F3NC internalization were not significantly different from NTNC internalization in CD-treated 9L (77.8%) and MDA-MB-435 (67.4%) cells (Figs. 3.4.1 and 3.4.2). Most importantly, there was no observable permeation of the F3NCs into the nuclei of the controls (Figs. 3.2.3.a and 3.3.3.a), or for any of the endocytic inhibitor treatments (Figs. 3.2.3.b-d and 3.3.3.b-d), in either cell line. The absence of nuclear entry by the F3NCs, particularly in the presence of CPZ, is especially interesting in light of the nuclear accumulation of molecular-F3 peptide when mediated by CPZ (Figs. 3.2.1.c and 3.3.1.c). Most strikingly, the degree of colocalization of the F3NCs with Lysotracker Red was significantly lower than for molecular-F3 peptide and NTNCs in the control, CD- and GEN-treated 9L and MDA-MB-435 cells (Figs. 3.5.1 and 3.5.2). For example, in the 9L control cells, F3NC-Lysotracker Red colocalization was 3-fold and 1.8-fold lower than for molecular-F3 peptide and the NTNCs, respectively, while in the MDA-MB-435 control cells, F3NC-Lysotracker Red colocalization was 6.4-fold and 3.3-fold lower than for molecular-F3 peptide and the NTNCs, respectively. As observed for molecular-F3 peptide and the NTNCs, the degree of F3NC-Lysotracker Red colocalization was most potently reduced by CPZ in both 9L (6.0%) and MDA-MB-435 (4.7%) cells, relative to the untreated control 9L (12.5%) and MDA-MB-435 (14.2%) cells (Figs. 3.5.1 and 3.5.2). These levels of colocalization were also similar to those observed for molecular-F3 peptide and the NTNCs in the CPZ-treated 9L and MDA-MB-435 cells (Figs. 3.5.1 and 3.5.2).

The observations from the endocytosis inhibition experiments indicate that: (i) neither macropinocytosis, clathrin-mediated, nor caveolae-mediated endocytosis are utilized by the molecular-F3 peptide as its primary pathway of cellular entry into either 9L or MDA-MB-435 cells; (ii) the above endocytic pathways each promote, to varying degrees, the internalization of the NTNCs and F3NCs, of which clathrin-mediated endocytosis is the major internalization pathway; and (iii) the F3NCs are more efficient than both the molecular-F3 peptide and the NTNCs at evading trafficking to the lysosomes and thus accumulate within different 'endosomal-type' vesicles, with this disparity being most prominent in the MDA-MB-435 cell line. Given the observation that a greater fraction of the endocytosed NTNCs, compared to the F3NCs, accumulate within lysosomes in MDA-MB-435 cells, we subsequently probed the intracellular trafficking of these two types of nanocarriers, independently of each other, in MDA-MB-435 cells, by immunocytochemistry, to gain further insight into the mechanism behind the selective accumulation of the targeted and non-targeted nanocarriers within different subcellular vesicles.

3.2.2 Spatiotemporal Probing of Nanocarrier Intracellular Trafficking by Immunocytochemistry

Separate batches of MDA-MB-435 cells, treated with either NTNCs or F3NCs, were fixed at various time points up to 6 hours after delivery of the NCs, following which, the cells were labeled for lysosome associated membrane protein 1 (LAMP1) and either early endosome antigen 1 (EEA1), which is associated with clathrin-mediated pathway, or caveolin 1 (caveolae marker), and analyzed by confocal microscopy. The rationale behind this approach was to obtain snapshots of any potential interaction between the FITC-labeled NTNCs/F3NCs and the above-

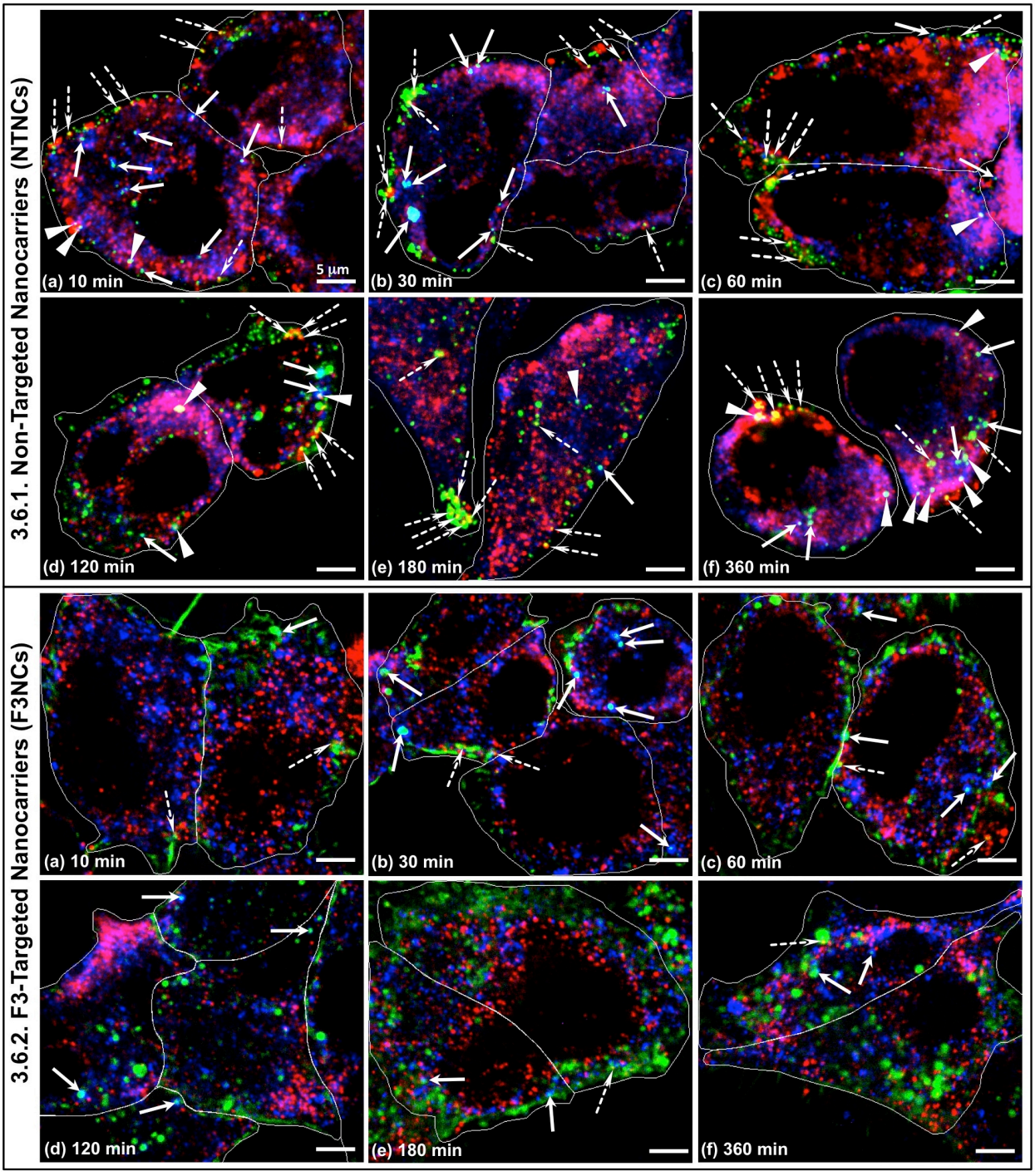

Fig 3.6 Spatiotemporal probing of the intracellular trafficking of the FITC-labeled NTNCs **(green; 3.6.1.a-f)** and FITC-labeled F3NCs **(green; 3.6.2.a-f)** along the clathrin-mediated endocytic pathway in MDA-MB-435 cells at various time points up to 6 hours post-delivery, in relation to the early endosomes (Early Endosomal Antigen 1 (EEA1); blue) and lysosome-associated membrane protein 1 (LAMP1; red). Regions of yellow/orange fluorescence denote colocalization between LAMP1 and either the NTNCs or F3NCs (dashed white arrows), regions of light-blue fluorescence denote colocalization between EEA1 and either the NTNCs or the F3NCs (solid white arrows), and regions of white fluorescence denote colocalization between the NTNCs, LAMP1 and EEA1 (white triangles). Scale bar: 5 µm.

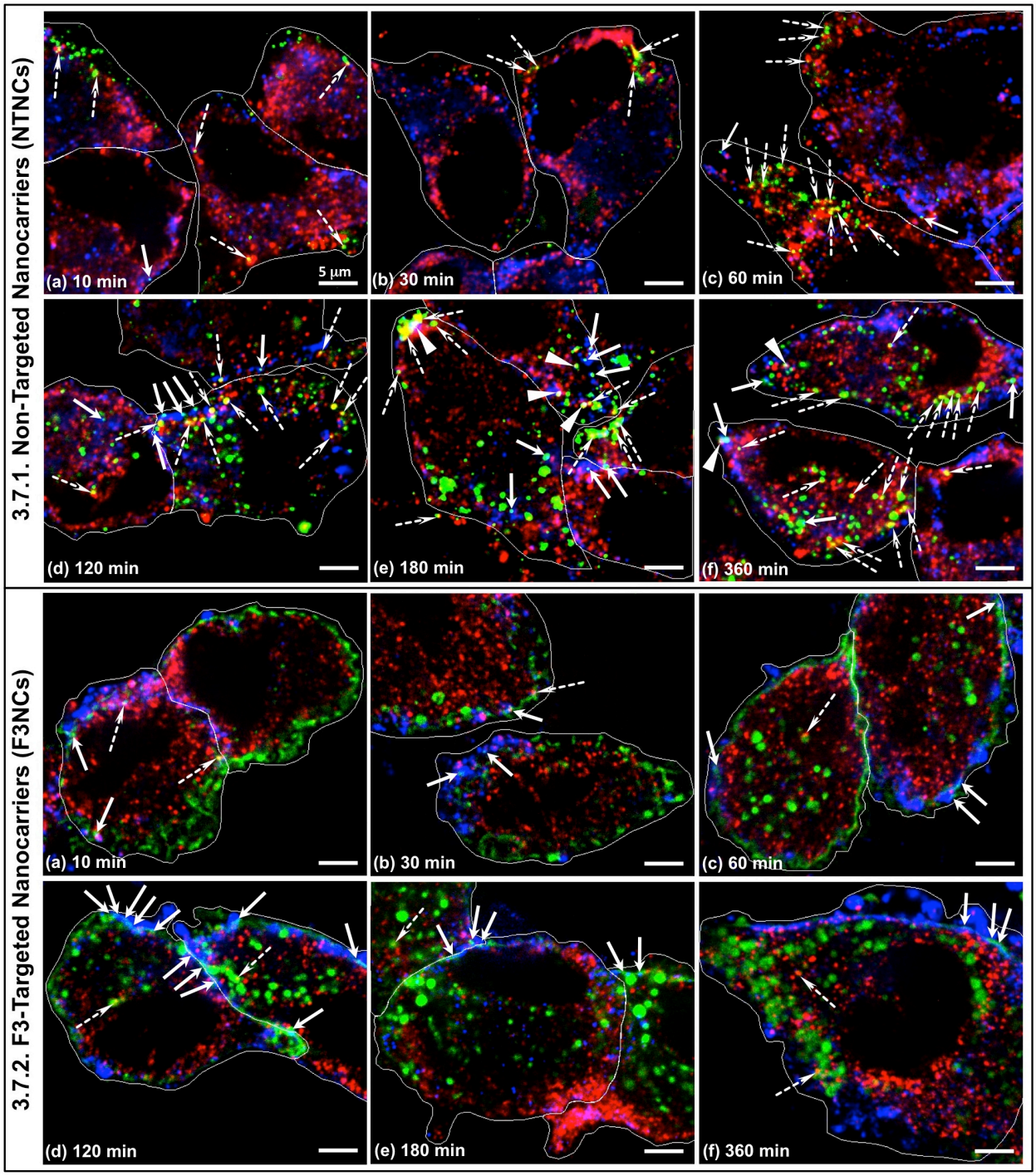

Fig 3.7 Spatiotemporal probing of the intracellular trafficking of the FITC-labeled NTNCs **(green; 3.7.1.a-f)** and FITC-labeled F3NCs **(green; 3.7.2.a-f)** along the caveolae-mediated endocytic pathway in MDA-MB-435 cells at various time points up to 6 hours post-delivery, in relation to the caveolae (Caveolin 1; blue) and lysosome-associated membrane protein 1 (LAMP1; red). Regions of yellow/orange fluorescence denote colocalization between LAMP1 and either the NTNCs or F3NCs (dashed white arrows), regions of light-blue fluorescence denote colocalization between Caveolin1 and either the NTNCs or the F3NCs (solid white arrows), and regions of white fluorescence denote colocalization between the NTNCs, LAMP1 and Caveolin1 (indicated by white triangles). Scale bar: 5 μm.

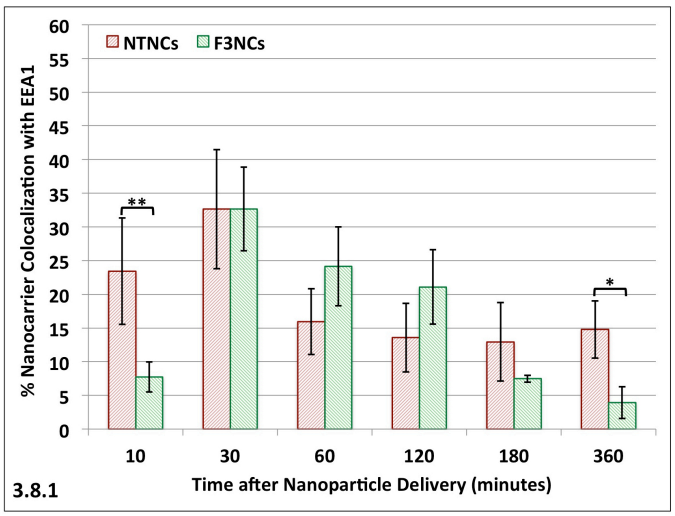

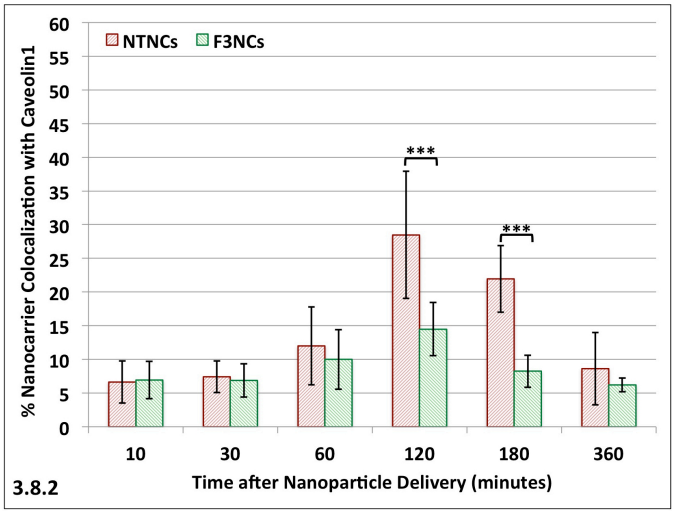

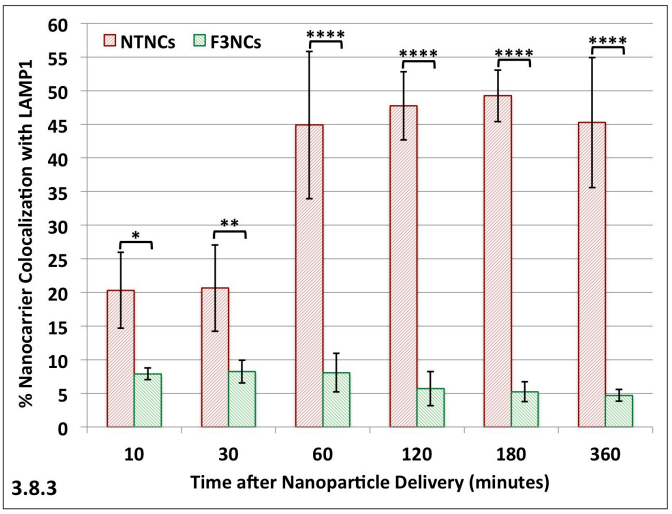

Fig 3.8 Comparisons of the colocalization profiles of the NTNCs and F3NCs with EEA1 **(3.8.1),** Caveolin1 **(3.8.2)** and LAMP1 **(3.8.3)** protein markers from 10 minutes up to 6 hours post-delivery in the MDA-MB-435 cell line. All values are based on the Manders' M_2 colocalization coefficients expressed as mean percentages. Error bars show standard deviations. P-values are indicated as follows: $P<0.05$ (*); $P<0.01$ (**); $P<0.001$ (***); $P<0.0001$ (****). Black brackets denote significant colocalization differences between the NTNCs and F3NCs at the same time point.

mentioned markers from internalization, and throughout their intracellular trafficking within the MDA-MB-435 cells. Therefore, the absence or presence of colocalization between the NTNCs/F3NCs and these markers facilitated further examination of the endocytic pathway(s) responsible for internalizing each of these NCs and, more importantly, if the F3NCs are indeed able to evade trafficking to the lysosomes. All confocal images were analyzed on the basis of (i) the degree of colocalization between the NTNCs/F3NCs with EEA1, Caveolin1 or LAMP1 and, (ii) the absence or presence of nuclear accumulation of the NTNCs/F3NCs. Distinct differences were observed between the F3NCs and NTNCs with respect to their interaction with, and intracellular trafficking within, the MDA-MB-435 cells.

The most prominent feature of the F3NC-treated MDA-MB-435 cells is the distinct delineation of their cell membranes with the green-fluorescent F3NCs. These cell membrane delineations were evident at all time points, up to 180 min post-delivery (Figs. 3.6.2.a-e & 3.7.2.a-e); however by 360 min post-delivery, the cell membrane delineations had markedly diminished, concomitant with prominent endosomal accumulation of the F3NCs (Figs. 3.6.2.f and 3.7.2.f). This observation suggests that, by 360 min post-delivery, the majority of the cell-membrane-bound F3NCs were endocytosed by the MDA-MB-435 cells. Interestingly, despite the high avidity of the F3NCs for the nucleolin over-expressing MDA-MB-435 cells, the appearance of F3NC-laden endosomes within the cytoplasm was most evident only at 30 minutes (Figs. 3.6.2.b and 3.7.2.b) and onward of delivery (Figs. 3.6.2.c-f, 3.7.2.c-f).

At 10 minutes after delivery, only 7.8% of the F3NCs colocalized with EEA1 (Figs. 3.6.2.a, 3.8.1), which then peaked to 32.7% colocalization at 30 minutes post-delivery (Fig. 3.6.2.b, 3.8.1), and thereafter decreased progressively to 3.9% colocalization by 360 minutes post-delivery (Figs. 3.6.2.c-f, 3.8.1). Colocalization between the F3NCs and Caveolin1 was diffuse

and confined exclusively to the cell surface; unlike the distinct punctate foci of colocalization observed between the F3NC-laden endosomes and EEA1 within the cytoplasm. At 10 minutes after delivery, 6.9% of the cell membrane-bound F3NCs colocalized with Caveolin1 (Fig. 3.7.2.a), which then peaked to 14.5% colocalization at 120 minutes post-delivery (Fig. 3.7.2.d), and thereafter decreased progressively to 6.2% by 360 minutes post-delivery (Figs. 3.7.2.e,f, 3.8.2). Furthermore, only scant colocalization between the F3NCs and LAMP1 was observed at the various time points (Figs. 3.6.2.a-f and 3.7.2.a-f; dashed white arrows). At 10 minutes after delivery, only 7.9% of the F3NCs colocalized with LAMP1, which then peaked to 8.2% colocalization at 30 minutes post-delivery, and thereafter decreased progressively to 4.7% colocalization by 360 minutes post-delivery (Fig. 3.8.3). Most notably, from 60 minutes after delivery and onward, larger F3NC-laden endosomes that exhibited an absence of colocalization with the EEA1, Caveolin1 and LAMP1 markers, began to accumulate, which suggests that the F3NCs are sequentially trafficked from the early endosomes to late endosomal vesicles (Figs. 3.6.2.c-f and 3.7.2.c-f), since the late endosomes are devoid of EEA1 and Caveolin1 markers. Moreover, some of these 'larger' F3NC-laden endosomes appeared within the perinuclear region from as early as 120 minutes after delivery and onward (Figs. 3.6.2.e,f and 3.7.2.d-f), although there was no observable entry or accumulation of F3NCs within the nuclei of the cells (Figs. 3.6.2.d-f and 3.7.2.d-f).

In stark contrast to the F3NC-treated cells processed for immunocytochemistry, cell membrane delineations were not observed with the NTNCs at any of the time points investigated (Figs. 3.6.1.a-f and 3.7.1.a-f). Given the inherent non-specific affinity of the NTNCs for negatively charged cell membranes, due to their modest positive surface charge (~ +16 mV, See Chapter 2), in addition to the appearance of NTNC-laden endosomes in the periphery of the

cytoplasm just 10 minutes after delivery (Figs. 3.6.1.a and 3.7.1.a), these observations suggest that the NTNCs are endocytosed slightly faster than the F3NCs upon contact with the cell membrane. In contrast to the F3NCs, a greater fraction of the NTNC-laden endosomes (23.4%; Fig. 3.8.1) were colocalized with EEA1 at 10 minutes after delivery (Figs. 3.5.1.a, solid white arrows), which correlated with the faster appearance of NTNC-laden endosomes in the cytoplasm at this time point. As observed for the F3NCs, the degree of colocalization between the NTNC-laden endosomes and EEA1 peaked to 32.6% colocalization at 30 minutes post-delivery (Fig. 3.6.1.b), and thereafter decreased progressively, but still remained as high as 14.8% by 360 minutes post-delivery (solid white arrows; Figs. 3.6.1.c-f, 3.8.1). Distinct punctate colocalization was observed between the NTNCs and Caveolin1 – positive endosomes both at the cell surface and within the cytoplasm (Figs. 3.7.1.d-f; solid white arrows). This contrasts with the colocalization between the F3NCs and Caveolin1, which was scant and confined exclusively to the cell surface (Figs. 3.7.2.a-f; solid white arrows). At 10 minutes after delivery, 6.6% of the NTNCs colocalized with Caveolin1 (Fig. 3.7.1.a), which then peaked to 28.5% colocalization at 120 minutes post-delivery (Fig. 3.7.1.d), and thereafter decreased to 8.6% colocalization by 360 minutes post-delivery (Figs. 3.7.1.e,f, 3.8.2). In stark contrast to the F3NC-treated cells, the NTNCs colocalized strongly with LAMP1, appearing as distinct punctate foci of orange/yellow fluorescence (dashed white arrows), both at the cell surface and in NTNC-laden endosomes within the cytoplasm (Figs. 3.6.1.a-f and 3.7.1.a-f). At 10 minutes after delivery, 20.3% of the NTNCs colocalized with LAMP1 (compared to 7.9% F3NC-LAMP1 colocalization at 10 minutes), which increased sharply to 44.9% colocalization at 60 minutes post-delivery, and peaked to 49.2% colocalization at 180 minutes post-delivery (Fig. 3.8.3). A slight decrease to 45.3% colocalization was observed at 360 minutes post-delivery, however this was not

significantly different from the degree of colocalization at 180 minutes post-delivery (Fig. 3.8.3). Therefore, the degree of colocalization between the NTNCs and LAMP1 increased with time and was significantly higher than that for the F3NCs at each time point, whereas the colocalization between the F3NCs and LAMP1 decreased with time. Moreover, NTNC-laden endosomes that exhibited dual-colocalization with LAMP1 and either EEA1 or Caveolin1 were also observed (Figs. 3.6.1.a, c-f and 3.7.1.e,f; white triangles). Importantly, as observed for the F3NCs, the NTNC-laden endosomes did not enter the nuclei, and largely remained dispersed throughout the cytoplasm.

3.2.3 Cell Membrane Interaction Profiles of Non-targeted and F3-targeted PAA-NCs

Our immunocytochemical analyses revealed a fundamental difference between the F3NCs and NTNCs, with respect to their interactions with the cell membranes of MDA-MB-435 cells in that, the F3NCs elicited prominent delineation of the MDA-MB-435 cell membranes, whereas this effect was not observed with the NTNCs. Cell membrane delineations were however observed for the NTNC-treated cells in the endocytosis inhibition images, but were less prominent than that observed for the F3NC-treated cells. Interestingly, prominent appearance of the F3NC-laden endosomes in the cytoplasm occurred only 30 minutes after delivery, whereas NTNC-laden endosomes appeared in the cytoplasm as early as 10 minutes after delivery. These observations indicate that the F3NCs first accumulate on the cell membrane, upon binding, for a significant period of time before being internalized, whereas the NTNCs do not accumulate on the cell membrane and are internalized fairly rapidly upon contact with the cell membrane. *Thus, there must be a difference between the F3NCs and NTNCs in their interaction with the MDA-MB-435 cell membrane.* Notably, the binding of positively charged nanoparticles to negatively

charged cell membranes is driven by non-specific electrostatic interactions. Furthermore, it has been demonstrated that the binding of amine-surface modified polystyrene nanoparticles to dipalmitoyl phosphocholine (DPPC) liposomes induces a lipid phase transition, from gel to fluid, at the nanoparticle-membrane interface,[48] which may potentiate the detachment of invaginating endosomes that form around the nanoparticle from the cell membrane.[49] Hence, our positively charged, amine-surface modified NTNCs may elicit a similar lipid phase transition in the regions of the MDA-MB435 cell membranes to which they bind, thereby potentiating their rate of endocytic uptake.

In contrast, while the F3NCs have a higher positive surface charge (~ +30 mV) than the NTNCs (~ +16 mV; See Chapter 2), the interaction of the former with the MDA-MB-435 cell membrane is limited to the binding interaction between their surface-conjugated F3 peptides and the cell surface bound nucleolin receptors. Furthermore, targeted nanoparticles of 50 nm in diameter and greater bind numerous receptors simultaneously with very high avidity (~1-3 x 10^{-13} M),[50] such that the internalization of further nanoparticles is limited by the redistribution of additional receptors on the cell membrane by lateral diffusion in order to compensate for the depletion of unbound cell surface receptors in the contact region between the cell membrane and nanoparticle.[51] The uptake of additional nanoparticles may be further limited by the rate at which new receptors are delivered to the cell membrane,[52] in order to compensate for those receptors that have been internalized along with the bound nanoparticle, as is the case with nucleolin.[53] This phenomenon provides a plausible explanation for the slightly longer lag time observed between the delivery of the F3NCs and their first appearance in the cytoplasm, compared to the NTNCs. This is attributed to the properties of the F3NCs, i.e. their hydrodynamic size of ~60 nm and their ligand surface coverage that elicits cell binding saturation (See Chapter 2), and is in

accordance with previous observations.[50,51]

Evidence in support of the specificity of the interaction between the F3-surface functionalized PAA-NCs and the nucleolin receptors is provided by a control experiment that was performed in a recent study published by our lab,[54] whereby we functionalized PAA-NCs with either the wild-type F3 peptide or a scrambled F3 peptide (identical amino acid composition, length and charge, but scrambled sequence) and compared the uptake of these functionalized nanocarriers in the nucleolin surface-expressing 9L cell line. The wild-type F3 peptide promoted uptake of the PAA-NCs, whereas the scrambled F3 peptide did not. This observation indicates that only the wild-type F3 peptide sequence is capable of adopting the correct secondary and/or tertiary conformation that is necessary for binding to the cell-surface nucleolin receptors, and thus promoting uptake of the nanocarriers.

3.2.4 Internalization and Intracellular Trafficking Profiles of F3 peptide, F3-targeted and Non-targeted PAA-NCs

After internalization, the drug-laden nanocarrier should ideally be delivered to the specific subcellular compartment within which that drug molecule elicits its mechanism of action, in order to circumvent extrusion of these drug molecules by the cell membrane-resident multidrug resistance (MDR) efflux pumps, *and thereby retain the efficacy of therapy*. Although recent studies have demonstrated that the physicochemical properties of a nanocarrier modulates its intracellular trafficking,[55,56] it still remained unclear, prior to our current study, as to how the presence of multiple copies of a targeting ligand on the surface of a nanocarrier, i.e. its multivalency, influences its intracellular trafficking and subcellular accumulation, relative to its non-targeted counterpart, or even relative to the targeting ligand alone. An important observation

from our endocytosis inhibition study is that neither of the endocytic inhibitors, CD, CPZ or GEN, completely blocked the internalization of the NTNCs or F3NCs, but each one decreased the internalization of the various nanocarriers to varying degrees. Since only one endocytic inhibitor was used at a time, so as to minimize cytotoxicity, the other endocytic pathways would have been still operational, and thus able to promote the uptake of the nanocarriers. This would account for why we did not observe complete inhibition of the uptake of the NTNCs and F3NCs in the presence of any one inhibitor.

Our endocytosis inhibition data demonstrated that (i) the intracellular trafficking of molecular-F3 peptide in its monovalent form is markedly different compared to when it is coupled to the surface of hydrogel PAA-NCs and (ii), although the non-targeted and F3-targeted PAA-NCs share common pathways of internalization, albeit to varying degrees, they each accumulate in distinct types of subcellular vesicles. We acknowledge that although the F3 peptides used in our experimental setup were not in their 'native form' i.e. they were chemically labeled with FITC fluorophore, the significantly smaller size of the FITC fluorophore (389 Da), compared to that of a single F3 peptide (3536 Da) or a single PAA-NC, has negligible, if any, effect on the behavior of the F3 peptide. Furthermore, the FITC fluorophore has only one reactive isothiocyanate group, and is therefore incapable of cross-linking multiple F3 peptides, so as to generate a multivalent peptide complex, which would likely alter the binding avidity of the F3 peptide for Nucleolin as well as alter its intracellular trafficking. The intracellular trafficking of monovalent molecular-F3 peptide is particularly interesting in that it inherently accumulated in lysosomes, with neither of the endocytic inhibitors CD or GEN being able to completely prohibit its cellular entry or accumulation in lysosomes. While CPZ also failed to prohibit the cellular entry of molecular-F3 peptide, it however *promoted a diversion in the trafficking of the*

molecular-F3 peptide from the lysosomes to the nucleus. We observed the same result for molecular-F3 peptide in both the 9L and MDA-MB-435 cell lines when the cells were subjected to potassium depletion (Appendix A3.1), which acts as a potent non-pharmacological inhibitor of the clathrin-mediated endocytic pathway. This phenomenon is therefore not unique to chlorpromazine, and we conclude that the inhibition of the clathrin-mediated pathway, irrespective of the inhibitor, promotes accumulation of molecular-F3 peptide within the nuclei of 9L and MDA-MB-435 cells. Notably, our observations are consistent with the study by Legrand *et al*., which first documented that the cellular uptake of the human Lactoferrin protein (hLf) is mediated by nucleolin and that the majority of these nucleolin-hLf complexes colocalize with EEA1, a marker specifically associated with clathrin in early endosomes.[57] Our findings therefore confirm that the cell's surface-bound nucleolin is associated with the clathrin-mediated endocytic pathway, which likely overrides the nuclear localization signal (NLS) of nucleolin and thus promotes the routing of the molecular-F3 peptide into the lysosomes. However, upon inhibiting the clathrin-mediated endocytic pathway by CPZ, the NLS function of nucleolin apparently predominates, thereby allowing translocation of nucleolin, together with any bound molecular-F3 peptide, directly into the nucleus. Given our observations with molecular-F3 peptide, we might have anticipated a similar intracellular trafficking pattern for the F3NCs, however this was not the case. Remarkably, in the absence, as well as the presence, of endocytic inhibitors, the F3NCs exhibited markedly lower accumulation within lysosomes as compared to molecular-F3 peptide and to the NTNCs, in both 9L and MDA-MB-435 cells. Most notably, CPZ was the only inhibitor that elicited a marked reduction in both the endocytosis and lysosomal accumulation of the F3NCs, in either cell line. A similar result was observed for the NTNCs in both the CPZ-treated 9L and MDA-MB-435 cells. Therefore, these data suggest that

while the F3NCs and the NTNCs share clathrin-mediated endocytosis as a common pathway of internalization, *the multivalent nature of the F3-targeted PAA nanocarrier significantly alters its intracellular trafficking within these cell lines, so as to avoid accumulation within the lysosomes.* It should be noted that while not all endocytosed NTNCs were found to colocalize with Lysotracker Red at 1 hour after delivery, it is likely that these NTNCs were sequestered within early and/or late endosomes that were still *en route* for fusion with lysosomes. Evidence in support of this premise is provided by our immunocytochemistry data in which only the NTNCs exhibited a time-dependent increase in colocalization with lysosome associated membrane protein 1 (LAMP1), over the 6-hour period during which the intracellular trafficking of the NTNCs was observed (Fig. 3.8.3).

The immunocytochemical analysis also corroborated the findings of the endocytosis inhibition experiment in MDA-MB-435 cells that clathrin-mediated endocytosis contributed approximately equally to the internalization of the NTNCs and F3NCs, while the caveolae-mediated pathway mediated greater internalization of the NTNCs than the F3NCs. This is evident from the observations that (i) CPZ decreased the internalization of the NTNCs and F3NCs to similar levels (Fig. 3.4.2), while the colocalization of the NTNCs and F3NCs with EEA1 both peaked at 30 minutes post-delivery to similar levels (Fig. 3.8.1), and (ii) in GEN-treated cells, the level of NTNC internalization was approximately 1.49-fold lower than that of the F3NCs (Fig. 3.4.2), while the peak NTNC-Caveolin1 colocalization at 120 min post-delivery was approximately 1.96-fold higher than that of the F3NC-CAV1 colocalization at the same time point (Fig. 3.8.2). These observations suggest that the presence of multiple F3 peptides on the surface of the F3NCs biases their internalization via the clathrin-mediated endocytic pathway, as compared to the NTNCs. From 60 min post-delivery, a progressive decrease in the colocalization

with EEA1, for both the F3NCs and NTNCs, was observed, suggesting that both types of nanocarriers were being transported into the *late endosomes*, which lack the EEA1 marker. Interestingly, for both the F3NCs and NTNCs, the peak in colocalization with Caveolin1 was achieved only at 120 minutes post-delivery. This observation may be due to the existence of bidirectional communication between the clathrin-mediated and caveolae-mediated endocytic pathways, whereby cargo that is internalized via caveolae-mediated endocytosis can be trafficked into EEA1 – positive endosomal compartments, and vice versa.[58,59] It was also interesting to note that the macropinocytosis inhibitor, Cytochalasin D, exerted a slightly greater inhibitory effect than Genistein on the internalization of the F3NCs in the MDA-MB-435 cells. This may be attributed to the previously reported observation that cell surface expressed Nucleolin is associated with the actin cytoskeleton,[60] and that Cytochalasin D inhibits macropinocytosis by disrupting actin polymerization.

3.2.5 F3-targeted PAA-NCs, but not Non-targeted PAA-NCs, evade co-internalization with LAMP1 at the cell surface

The most striking difference between the F3NCs and NTNCs in their intracellular trafficking is the presence of prominent punctate colocalization between the NTNCs and LAMP1, both at the cell surface and during their transport into the interior of the cells, at all time points, whereas such colocalization between the F3NCs and LAMP1 was scant over the 6-hour period during which their intracellular trafficking was tracked. This observation must be understood in the context of the trafficking of the newly synthesized lysosome-associated membrane proteins (LAMPs) themselves, and the role that these proteins play in the interaction between endosomes and lysosomes. First, the transport of newly synthesized LAMPs from the *trans*-Golgi network

(TGN) to the lysosomes may follow either a direct or indirect pathway.[61,62] The direct pathway is a completely intracellular route whereby newly synthesized LAMPs are transported from the TGN to either early or late endosomes and then to lysosomes. In the indirect pathway, the LAMPs are first transported from the TGN to the extracellular surface of the cell membrane, subsequently internalized by the clathrin-mediated endocytic pathway,[63] and then sequentially delivered to the early endosomes, late endosomes and finally the lysosomes. Second, LAMPs are essential for facilitating fusion between phagosomes and lysosomes in macrophages,[64] and may very well be necessary for facilitating fusion between the late endosomes and lysosomes in other non-phagocytic cell types. It is therefore apparent from the positive cell surface labeling of the MDA-MB-435 cells with anti-LAMP1 antibody that (i) the indirect LAMP trafficking pathway is indeed operational in the MDA-MB-435 cell line, and (ii) the NTNCs, but not the F3NCs, are co-internalized with LAMP1 proteins from the cell surface via the clathrin-mediated pathway, which commits these NTNC-laden, EEA1-positive endosomes to undergo fusion with the lysosomes, as illustrated by their colocalization with Lysotracker Red in our live cell endocytosis inhibition experiment. Furthermore, the presence of NTNC-laden endosomes exhibiting dual-colocalization with LAMP1, and with either EEA1 or Caveolin1, indicates that, despite being trafficked via either the clathrin-mediated or caveolae-mediated endocytic pathways, the NTNC-laden endosomes are still committed to undergo fusion with the lysosomes. Moreover, the time-dependent increase in colocalization between the NTNCs and LAMP1 confirms that the NTNCs do accumulate within the lysosomes over time. Figure 3.1 illustrates the internalization and intracellular trafficking profiles of molecular-F3 peptide, the F3NCs and NTNCs in nucleolin-overexpressing cells based on our observations.

Considering that LAMP1 is necessary for facilitating fusion between phagosomes and

lysosomes, it is plausible that the absence of LAMP1 proteins in the F3NC-laden, EEA1-positive endosomes would abrogate the ability of these F3NC-laden late endosomes to fuse with lysosomes. The presence of large, punctate F3NC-laden, EEA1/LAMP1 – negative vesicles within the perinuclear space, 360 minutes after delivery, supports our postulate that the F3NCs accumulate within late endosomes, but without subsequent fusion with lysosomes. Given that the late endosomes can also fuse with the TGN, we speculate that the F3NCs may be transported into the nucleus via retrograde transport, through the endoplasmic reticulum, over longer periods of time. Exploiting this pathway would therefore serve as an alternative mechanism for delivering into the nucleus nanocarriers whose hydrodynamic diameters exceed the cut-off limit of the nuclear pore complexes, as is the case with our hydrogel polyacrylamide nanocarriers. Further studies are underway in our lab to determine the long-term subcellular localization of the F3NCs in nucleolin-overexpressing cells.

Our observation that molecular-F3 peptide is normally trafficked to the lysosomes is consistent with a recent study which reported that nucleolin colocalizes with LAMP1 in the phagosomal compartment of macrophages.[65] Importantly, previous studies have also demonstrated that LAMP proteins are overexpressed at the surface of highly metastatic tumor cells.[66,67] The prominent cell surface labeling of the highly metastatic MDA-MB-435 cells[68] with anti-LAMP1 antibody in our study is therefore consistent with these studies. When taken into consideration with these previous reports, our observations suggest that the high surface density of LAMP1 proteins in the highly metastatic MDA-MB-435 cells increases the likelihood of nucleolin being co-internalized with LAMP1 proteins, which in turn commits the nucleolin-laden endosome to fusion with the lysosomes. However, this is not the case when the F3NCs engage nucleolin receptors at the surface of MDA-MB-435 cells and are internalized.

3.2.6 Conclusion

Our investigation demonstrates that the presence of F3 peptide on the surface of the polyacrylamide hydrogel nanocarrier significantly modulates the nature of the nanocarrier's interaction with the cell membrane of the target cell, including not only its internalization but also its intracellular trafficking and subcellular localization, relative to the non-targeted nanocarrier. Furthermore, the ability of the F3-targeted hydrogel nanocarriers, but not of the molecular-F3 peptide, to evade trafficking to the lysosomes, strongly suggests that the *multivalent nature* of the F3-targeted hydrogel nanocarrier is responsible for this effect. The implications of our observations are two-fold. First, from a general perspective, it cautions against making the assumption that a targeted nanocarrier's fate within cells is solely determined by the targeting ligand, or solely the carrier, or by a combination of the respective properties of the ligand and carrier (which might adversely affect the efficacy of therapy). Second, and more specifically, our findings are particularly relevant to the targeting of highly metastatic tumor cells, and thus may provide new insights into a possible mechanism of preventing the co-internalization of drug nanocarriers with LAMP1, in order to circumvent their trafficking to lysosomes. This appears to have important implications regarding the potential advantages of nano-drugs with multivalent ligand targeting, compared to individual drug molecules containing an identical single targeting ligand, especially when it comes to overcoming the multi-drug resistance (MDR) of metastatic cancer cells. Also of much interest is the possibility of engineering nanoparticles that mimic natural pathogens' ability to overcome the cell's defence mechanisms. Further studies are being conducted in our lab to elucidate the mechanism by which the F3-targeted hydrogel nanocarriers circumvent trafficking to the lysosomes in nucleolin-overexpressing cell lines.

3.2.7 Experimental Section

Reagents and Materials

Acrylamide (AA), 3-(acryloyloxy)-2-hydroxypropylmethacrylate (AHM), ammonium persulfate (APS), *N,N,N`,N`*-tetramethylethylenediamine (TEMED), sodium dioctyl sulfosuccinate (AOT), Brij 30, L-cysteine, fluorescein isothiocyanate (FITC) and phosphate-buffered solution (PBS) tablets were purchased from Sigma-Aldrich (St. Louis, MO). N-(3-aminopropyl)-methacrylamide hydrochloride (APMA) was purchased from Polysciences (Warrington, PA). Ethanol (100 %) and hexane were purchased from Fisher Scientific (Pittsburgh, PA). Heterobifunctional polyethyleneglycol (MAL–PEG–SCM, MW: 2,000 Da) was purchased from Creative PEG Works (Winston Salem, NC). The 9L rat gliosarcoma and MDA-MB-435 human breast adenocarcinoma cell lines were obtained from American Type Culture Collection (Manassas, VA, USA). Dulbecco's modified Eagle medium (DMEM), Rosswell Park Memorial Institute (RPMI-1640) medium, Gibco 0.05 % Trypsin-EDTA, Gibco 100x PenStrep-Glutamine and Gibco Heat-Inactivated Fetal Bovine Serum (HI-FBS) were purchased from Invitrogen (Carlsbad, CA). Endocytosis inhibitors, Cytochalasin D, Chlorpromazine, and Genistein were obtained from Sigma-Aldrich. Cysteine terminated F3 peptide (F3-Cys: KDEPQRRSARLSAKPAPPKPEPKPKKAPAKKC) was purchased from SynBioSci (Livermore, CA). Mouse monoclonal anti-EEA1, rabbit polyclonal anti-Caveolin1 and goat polyclonal anti-LAMP1 antibodies were purchased from Santa Cruz Biotechnology, Inc (Santa Cruz, CA, USA). Lysotracker Red DND-99, donkey anti-mouse (H+L) Alexa Fluor 568 (AF-568), donkey anti-rabbit (H+L) AF-568 and donkey anti-goat (H+L) Alexa Fluor 647 (AF-647) antibodies were obtained from Invitrogen. Normal donkey serum was purchased from LAMPIRE Biological Laboratories (Pipersville, PA). Methanol-free electron microscopy grade 20% (w/v)

paraformaldehyde solution was purchased from Electron Microscopy Services (Hatfield, PA, USA). All solutions were prepared in 18 MΩ water purified in a Barnstead 1 Thermolyne Nanopure II system. All reagents and materials were used as received without further purification.

Synthesis of FITC-labeled amine surface-functionalized hydrogel polyacrylamide nanocarriers

A monomer mixture consisting of 1 mg FITC, 711 mg acrylamide, 55 mg APMA, and 460 μL AHM were dissolved in PBS buffer (pH 7.4) and mixed together for 2 hours at room temperature. The mixture was emulsified in organic media containing surfactant (45 mL hexane, 1.6 g AOT, and 3.1 g Brij30) by continuous stirring for 20 minutes under Argon atmosphere in order to purge the reaction mixture of oxygen. Thereafter, polymerization was triggered by addition of radical initiator (100 μL of 10 % (w/v) ammonium persulfate in DI water and 100 μL of TEMED). The reaction proceeded for 2 hours under mild argon purging and was terminated by exposing the reaction to normal atmosphere (radical quenching by atmospheric oxygen). The product was recovered through multiple separation steps: (i) removal of hexane by rotary evaporation, and (ii) multiple rinses with 100 % (v/v) ethanol to remove unconjugated FITC dye and surfactants, followed by multiple rinses with DI water to remove residual surfactants using an Amicon stirred cell fitted with a 300 kDa molecular weight cut-off filter. The final product was lyophilized and kept frozen at -20 °C until use.

Surface functionalizations of PAA nanocarriers

Lyophilized FITC-labeled PAA-NCs (50 mg) were dissolved in 2.5 mL PBS buffer (pH 7.4) and sonicated until the solution turned transparent, to which 4 mg heterobifunctional PEG (SCM-PEG-MAL) was then added and the mixture stirred continuously (~600 rpm) for 2 hours at room temperature. The reaction between the succinimidyl ester group of the PEG crosslinker and the primary amine groups on the surface of PAA-NCs yielded maleimidyl ester-terminated PEG-conjugated PAA-NCs. Thereafter, the PEGylated PAA-NCs were washed three times with DI water by centrifugation using an Amicon centrifugal filter (Millipore, 100 kDa molecular weight cut-off) at 5000*xg* for 20 min. The procedure was repeated twice more with PBS buffer (pH 7.4). After washing to remove unbound PEG crosslinkers, the surface PEGylated PAA-NCs were reacted with 11 mg F3-Cys peptide in PBS buffer (pH 7.4) and the conjugation reaction allowed to run overnight at room temperature under continuous stirring at ~600 rpm. The reaction between the thiol group of the carboxy terminal Cys residue of the F3 peptide moieties and the maleimidyl ester termini of the PEG crosslinkers facilitated covalent coupling of the F3 peptide moieties to the PEG crosslinkers already conjugated to the PAA-NC surfaces. The F3 surface functionalized PEGylated PAA-NCs (F3NCs) were subsequently incubated with 1.74 mg L-cysteine under continuous stirring for 2 hours at room temperature to cap any unreacted maleimidyl ester groups so as to prevent their reaction with cell surface thiols. Thereafter, the F3NCs were washed five times with PBS (pH 7.4) using an Amicon centrifugal filter (100 kDa molecular weight cut-off) at 4000x*g* for 20 minutes and the final volume adjusted to 5 mL with PBS (pH 7.4). The filtered nanocarriers were kept frozen at -20 °C until use. All steps were performed shielded from light. Note that the mass ratios of heterobifunctional PEG and F3 peptide to PAA-NCs were optimized via cell-based assays as described in Chapter 2.

Synthesis of FITC-labeled F3 peptide

Stock solutions of F3-Cys peptide (100 μg.μL^{-1} in 10 mM phosphate buffer, pH 8.0) and FITC (160 μg.μL^{-1} in DMSO) were initially prepared. Thereafter, 10 μL of the FITC stock was added to 390 μL of F3-Cys solution in a clean glass vial and sonicated for 5 minutes. The final volume of the sonicated solution was increased to 10 mL with 10 mM phosphate buffer (pH 8.0), and the conjugation reaction was allowed to proceed overnight with continuous stirring at 37 °C while shielded from light. The following day, the FITC-labeled F3 peptides were subjected to 15 washes with a 3 kDa molecular weight cut-off Amicon centrifugal filter (4000*xg* for 20 minutes) to remove any unreacted FITC molecules. The filtered FITC-labeled F3 peptides were aliquoted and stored at -20 °C until further use.

Nanocarrier sizing and morphology

The size of the prepared F3NCs was determined via two different methods; scanning electron beam microscopy (SEM) and dynamic light scattering (DLS). Lyophilized F3NCs were dissolved in DI water to a final concentration of 0.2 mg.mL^{-1}. A droplet of the NC solution was loaded onto a SEM stub, dried and subsequently coated with gold using a gold sputter coater. SEM imaging was performed using the FEI Nova NanoLab dualbeam SEM system. For all DLS sizing measurements, the lyophilized NCs were dissolved in DI water to a final concentration of 1 mg.mL^{-1} and analyzed with a Beckman-Coulter Delsa Nano C particle analyzer.

Nanocarrier zeta potential measurement

Zeta potential measurements of unmodified PAA-NCs (without PEG or F3 peptide), PEGylated

PAA-NCs and the F3NCs were performed in order to determine their respective surface charges. All zeta potential measurements were performed on 1 $mg.mL^{-1}$ solutions of each type of nanocarrier, prepared in DI water, using a Beckman-Coulter Delsa Nano C particle analyzer. All measurements were performed in triplicate.

Cell culture

Three different nucleolin-overexpressing tumor cell lines, 9L rat gliosarcoma, MDA-MB-435 human ductal adenocarcinoma/ melanoma, and MCF-7 human breast adenocarcinoma were cultured aseptically at 37 °C under 5 % CO_2 humidified atmosphere in either BD Falcon Primaria tissue culture dishes (100 mm x 20 mm) or Multiwell 6-well plates. The 9L and MCF-7 cell lines were cultured in Rosewell Park Memorial Institute (RPMI) medium supplemented with 10 % (v/v) heat inactivated fetal bovine serum (FBS) and MDA-MB-435 cell was cultured in Dulbecco's Modified Eagle's Medium (DMEM) supplemented with 10 % (v/v) FBS and 1 % (v/v) penicillin-streptomycin-glutamine (PSG). Cell cultures were passaged during exponential growth phase by incubating the cells with 0.05 % Trypsin-EDTA solution at 37 °C until the cells attained rounded morphology, followed by resuspension of the detached cells in their respective culture media, and sub-culturing into new sterile culture dishes or multiwell plates. All F3NC and unmodified PAA-NC suspensions were sterile filtered with a 0.2 μ syringe filter prior to use in all cell culture experiments.

Endocytosis inhibition

The internalization of FITC-labeled F3 peptides, FITC-labeled F3NCs and FITC-labeled unmodified PAA-NCs were studied separately in the MDA-MB-435 and 9L cell lines in the

presence of the endocytosis inhibitors chlorpromazine (CPZ; 10 μg.mL^{-1}), genistein (GEN; 200 μM) or cytochalasin D (CD; 50 μM), which block the clathrin-mediated, caveolae-mediated and macropinocytosis pathways respectively. These inhibitor concentrations were previously reported to inhibit the respective endocytic pathways *in vitro*.[69,70] Furthermore, the *in vitro* cytotoxicity of these inhibitors were tested independently by MTT assay on both the 9L and MDA-MB-435 cell lines. Concentrations higher than the abovementioned values were avoided due to cell viability issues (Appendix A3.2). All inhibitors were dissolved in DMSO as 100-fold concentrated stocks and diluted to their final concentrations in culture medium. MDA-MB-435 or 9L cells, cultured on Corning No.1½ circular glass coverslips, were incubated with either of the above inhibitors at their respective final concentrations for 30 minutes at 37 °C. Thereafter, either F3 peptides, F3NCs or unmodified (non-targeted) PAA-NCs were delivered to the cell cultures at a final concentration of 0.1 mg.mL^{-1} and incubated in the presence of the endocytic inhibitors for an additional 1 hour at 37 °C. Thereafter, the culture media containing endocytic inhibitors and unbound NCs were aspirated and the cells gently rinsed three times with fresh pre-warmed culture media. The cells were then labeled with Lysotracker Red DND-99 fluorophore at a final concentration of 300 nM at 37 °C for 5 minutes and washed once more prior to confocal imaging. Confocal imaging was performed on an Olympus inverted confocal microscope and all images were acquired with a 100x oil immersion objective lens. The FITC and Lysotracker Red DND-99 fluorophores were sequentially excited with the 488 nm and 568 nm lines respectively. The effects of the endocytosis inhibitors on the uptake of the F3 peptides, NTNCs and F3NCs were measured directly from the respective confocal images using ImageJ v.1.46n software. Briefly, the FITC fluorescence emission intensities were measured only within regions of interest (ROI) drawn around individual cells in each image. These ROIs were drawn so as to exclude the

cell membrane, and thus any FITC fluorescence emissions from either F3 peptides or nanocarriers that were only attached to the cell membrane and had not yet been internalized. Uptake values for each inhibitor are represented as percentages of mean FITC fluorescence intensity relative to the mean of the corresponding control ±SD.

Immunocytochemistry

Immunocytochemical labeling of the membrane-bound Caveolin1, EEA1 and LAMP1 proteins was employed to study the intracellular trafficking of F3-targeted PEGylated and unmodified PAA-NCs in MDA-MB-435 cells. Cell monolayers, grown on Corning No.1½ circular glass coverslips, were treated with either unmodified PAA-NCs or F3NCs (final concentration of 0.1 $mg.mL^{-1}$) for 10, 30, 60, 120, 180 and 360 minutes respectively. Following treatment, the cells were rinsed briefly three times with warm GIBCO DPBS solution and fixed in 4 % (v/v) phosphate-buffered paraformaldehyde (10 mM PBS, pH 7.2) for 10 minutes at room temperature. Immediately following fixation, the cells were subjected to three 10-minute washes with 10 mM PBS (pH 7.2) with gentle agitation on a rocking-shaker. The cells were subsequently permeabilized in permeabilization buffer (0.05 % (v/v) Tween-20, 10 mM PBS, pH 7.2) for 10-minutes at room temperature with gentle agitation on a rocking shaker, followed immediately by three washes with 10mM PBS (pH 7.2). The permeabilized cells were blocked overnight at $4^{\circ}C$ in donkey serum buffer (10% (v/v) normal donkey serum; 0.05 % (v/v) Tween-20; 0.05 % (w/v) sodium azide; 10 mM PBS pH 7.2). Following blocking, the cells were incubated in primary antibody labeling solution (either anti-EEA1 and anti-LAMP1 or anti-Caveolin1 and anti-LAMP1 antibodies diluted 1:20 in primary antibody dilution buffer (1 % (v/v) normal donkey serum; 0.05 % (v/v) Tween-20; 0.05 % (w/v) sodium azide; 10 mM PBS

pH 7.2) at room temperature in a humidified chamber for 3 hours. Immediately following incubation, the coverslips were washed three times with PBS at room temperature (10 minutes per wash) to remove excess primary antibody. The secondary antibody incubation buffers were prepared by diluting the appropriate antibodies in a 1:500 ratio in secondary antibody dilution buffer (0.05 % (v/v) Tween-20; 0.05 % (w/v) sodium azide; 10 mM PBS pH 7.2). Incubation in secondary antibody labeling solution for 1 hour as described above for the primary antibody incubation. Following antibody labeling, the coverslips were washed three times with PBS at room temperature (10 minutes per wash) with gentle agitation on a rocking shaker. After the last wash, the coverslips were mounted (cell-surface down) onto glass slides with Dako Fluorescent Mounting Medium and stored overnight at 4 °C prior to fluorescence confocal imaging. Imaging was performed on an Olympus inverted confocal microscope and all images were acquired with a 100x oil immersion objective lens. The FITC, AF-568 and AF-647 fluorophores were sequentially excited with the 488 nm, 568 nm and 647 nm laser lines respectively.

Colocalization Analyses

All confocal images were subjected to fluorophore colocalization analysis in ImageJ v.1.64n software using the JACoP plugin.[71] Briefly, colocalization analyses were performed on a cell-by-cell basis by first drawing ROIs around individual cells in each native confocal image. Each image was then split into its component red, green and blue channels, and each ROI subsequently applied to the separated channels respectively. Thereafter, colocalization analyses between pairs of color channels (either green: FITC vs. red: Lysotracker Red/LAMP1-AF647 or green: FITC vs. blue: EEA1-AF568/ Caveolin1-AF568) for each ROI were then performed in JACoP using automatic thresholding for each channel. Manders' M_2 coefficients based on the

threshold settings were generated for each analysis, where the M_2 coefficient is defined as the fraction of the green channel (FITC) overlapping either the blue channel (EEA1/ Caveolin1) or red channel (Lysotracker Red/LAMP1). Colocalization values for each condition are based on the mean M_2 coefficients represented as percentages ± SD.

Statistical Analyses

The endocytosis inhibition and colocalization data for each cell line were statistically analyzed by One-Way ANOVA followed by Tukey's multiple comparisons test using GraphPad Prism v6.00 software for Mac OSX. In instances where selected pairs of columns in a data set were compared against each other, Bonferroni's multiple comparisons test was used in conjunction with the One-Way ANOVA test. All analyses were performed with a confidence interval set at 95 %. P-values <0.05 were considered significant.

Acknowledgements

The authors thank Dr. Ting Wang and Dr. Zhan Chen for their advice with regard to the experimental approach of the endocytosis inhibition study, as well as Dr. Christine Labno for her generous advice on performing confocal image colocalization analysis. The authors also thank Dr. Kathleen Nolta for her critical review of this manuscript. The authors are also grateful to the Electron Microbeam Analysis Laboratory and Microscopy and Image-Analysis Laboratory for use of their instrumentation for EM and confocal imaging. This work was supported by NIH Grants NIBIB R01 EB007977 (RK), NIBIB R000262 (RK), and NIH/NCI R33CA125297 (RK). L. Karamchand was supported by the International Fulbright Science and Technology Award

and the South African National Research Foundation Doctoral Scholarship for Study Abroad.

References

1. J. Funkhouser, *Curr Drug Discovery*, 2002, **2**.
2. S. S. Kelkar and T. M. Reineke, *Bioconjugate chemistry*, 2011, **22**, 1879–903.
3. J. Harrell and R. R. Kopelman, *Biophotonics Int*, 2000, **7**, 22–24.
4. H. Xu, S. M. Buck, R. Kopelman, M. A. Philbert, M. Brasuel, B. D. Ross, and A. Rehemtulla, *Israel Journal of Chemistry*, 2004, **44**, 317–337.
5. B. Ross, A. Rehemtulla, Y.-E. L. Koo, G. R. Reddy, G. Kim, C. Behrend, S. Buck, R. Schneider, M. A. Philbert, R. Weissleder, and R. R. Kopelman, in *Proceedings of SPIE*, SPIE, 2004, vol. 5331, pp. 76–83.
6. R. Kopelman, Y.-E. Lee Koo, M. Philbert, B. A. Moffat, G. Ramachandra Reddy, P. McConville, D. E. Hall, T. L. Chenevert, M. S. Bhojani, S. M. Buck, A. Rehemtulla, and B. D. Ross, *Journal of Magnetism and Magnetic Materials*, 2005, **293**, 404–410.
7. G. R. Reddy, M. S. Bhojani, P. McConville, J. Moody, B. A. Moffat, D. E. Hall, G. Kim, Y.-E. L. Koo, M. J. Woolliscroft, J. V Sugai, T. D. Johnson, M. a Philbert, R. Kopelman, A. Rehemtulla, and B. D. Ross, *Clinical cancer research : an official journal of the American Association for Cancer Research*, 2006, **12**, 6677–86.
8. Y.-E. Koo Lee and R. Kopelman, in *Multifunctional Nanoparticles for Drug Delivery Applications: Imaging, Targeting, and Delivery*, eds. S. Svenson and R. K. Prud'homme, Springer US, Boston, MA, 2012, pp. 225–255.
9. N. Kashyap, N. Kumar, and M. N. V. R. Kumar, *Critical reviews in therapeutic drug carrier systems*, 2005, **22**, 107–49.
10. S. A. Meenach, K. W. Anderson, and J. Z. Hilt, in *Safety of Nanoparticles, Nanostructure Science and Technology*, ed. T. J. Webster, Springer Science+Business Media, LLC, New York, NY, USA, New York, NY, 2009, pp. 131–157.
11. K. S. Soppimath, T. M. Aminabhavi, A. R. Kulkarni, and W. E. Rudzinski, *Journal of controlled release : official journal of the Controlled Release Society*, 2001, **70**, 1–20.
12. D. Gao, H. Xu, M. A. Philbert, and R. Kopelman, *Nano letters*, 2008, **8**, 3320–4.
13. S. Wang, G. Kim, Y.-E. K. Lee, H. J. Hah, M. Ethirajan, R. K. Pandey, and R. Kopelman, *ACS nano*, 2012, **6**, 6843–51.
14. M. A. M. Oliveira, C. Boyer, M. Nele, J. C. Pinto, P. B. Zetterlund, and T. P. Davis, *Macromolecules*, 2011, **44**, 7167–7175.
15. C. Pinto Reis, R. J. Neufeld, A. J. Ribeiro, and F. Veiga, *Nanomedicine : nanotechnology, biology, and medicine*, 2006, **2**, 8–21.
16. B. A. Moffat, G. R. Reddy, P. McConville, D. E. Hall, T. L. Chenevert, R. R. Kopelman, M. Philbert, R. Weissleder, A. Rehemtulla, and B. D. Ross, *Molecular imaging*, 2003, **2**, 324–32.
17. P. Sharma, S. Brown, G. Walter, S. Santra, and B. Moudgil, *Advances in colloid and interface science*, 2006, **123-126**, 471–85.
18. S. T. Selvan, T. T. Y. Tan, D. K. Yi, and N. R. Jana, *Langmuir : the ACS journal of surfaces and colloids*, 2010, **26**, 11631–41.
19. S. M. Buck, Y.-E. L. Koo, E. Park, H. Xu, M. A. Philbert, M. A. Brasuel, and R. Kopelman, *Current opinion in chemical biology*, 2004, **8**, 540–6.

20. S. M. Buck, H. Xu, M. Brasuel, M. A. Philbert, and R. Kopelman, *Talanta*, 2004, **63**, 41–59.
21. Y.-E. Koo Lee and R. Kopelman, in *Imaging and Spectroscopic Analysis of Living Cells Optical and Spectroscopic Techniques Methods in enzymology*, ed. P. M. Conn, UK Academic Press, First., 2012, vol. 504, pp. 419–70.
22. M. J. Moreno, E. Monson, R. G. Reddy, A. Rehemtulla, B. D. Ross, M. Philbert, R. J. Schneider, and R. Kopelman, *Sensors and Actuators B: Chemical*, 2003, **90**, 82–89.
23. W. Tang, H. Xu, R. Kopelman, and M. A. Philbert, *Photochemistry and photobiology*, 2005, **81**, 242–9.
24. S. Wang, W. Fan, G. Kim, H. J. Hah, Y.-E. K. Lee, R. Kopelman, M. Ethirajan, A. Gupta, L. N. Goswami, P. Pera, J. Morgan, and R. K. Pandey, *Lasers in surgery and medicine*, 2011, **43**, 686–95.
25. W. Tang, H. Xu, E. J. Park, M. A. Philbert, and R. Kopelman, *Biochemical and biophysical research communications*, 2008, **369**, 579–83.
26. M. Hamidi, A. Azadi, and P. Rafiei, *Advanced drug delivery reviews*, 2008, **60**, 1638–49.
27. M. Oishi, H. Hayashi, M. Iijima, and Y. Nagasaki, *Journal of Materials Chemistry*, 2007, **17**, 3720–3725.
28. F. Meng, W. E. Hennink, and Z. Zhong, *Biomaterials*, 2009, **30**, 2180–98.
29. R. Cheng, F. Feng, F. Meng, C. Deng, J. Feijen, and Z. Zhong, *Journal of controlled release : official journal of the Controlled Release Society*, 2011, **152**, 2–12.
30. D. Putnam and J. Kopecek, *Bioconjugate chemistry*, 1995, **6**, 483–92.
31. H. Hillaireau and P. Couvreur, *Cellular and molecular life sciences : CMLS*, 2009, **66**, 2873–96.
32. J. Rejman, V. Oberle, I. S. Zuhorn, and D. Hoekstra, *The Biochemical journal*, 2004, **377**, 159–69.
33. S. Zhang, J. Li, G. Lykotrafitis, G. Bao, and S. Suresh, *Advanced materials*, 2009, **21**, 419–424.
34. H. Yuan and S. Zhang, *Applied Physics Letters*, 2010, **96**, 033704.
35. Y. Geng, P. Dalhaimer, S. Cai, R. Tsai, M. Tewari, T. Minko, and D. E. Discher, *Nature nanotechnology*, 2007, **2**, 249–55.
36. J.-H. Park, G. von Maltzahn, L. Zhang, M. P. Schwartz, E. Ruoslahti, S. N. Bhatia, and M. J. Sailor, *Advanced materials (Deerfield Beach, Fla.)*, 2008, **20**, 1630–1635.
37. X. Banquy, F. Suarez, A. Argaw, J.-M. Rabanel, P. Grutter, J.-F. Bouchard, P. Hildgen, and S. Giasson, *Soft Matter*, 2009, **5**, 3984–3991.
38. O. Harush-Frenkel, E. Rozentur, S. Benita, and Y. Altschuler, *Biomacromolecules*, 2008, **9**, 435–43.
39. O. P. Perumal, R. Inapagolla, S. Kannan, and R. M. Kannan, *Biomaterials*, 2008, **29**, 3469–3476.
40. Y. Zhang, M. Yang, J.-H. Park, J. Singelyn, H. Ma, M. J. Sailor, E. Ruoslahti, M. Ozkan, and C. Ozkan, *Small (Weinheim an der Bergstrasse, Germany)*, 2009, **5**, 1990–6.
41. L. Créancier, H. Prats, C. Zanibellato, F. Amalric, and B. Bugler, *Molecular biology of the cell*, 1993, **4**, 1239–50.
42. S. Christian, J. Pilch, M. E. Akerman, K. Porkka, P. Laakkonen, and E. Ruoslahti, *The Journal of cell biology*, 2003, **163**, 871–8.
43. I. Winer, S. Wang, Y.-E. K. Lee, Y.-E. K. Lee, W. Fan, Y. Gong, D. Burgos-Ojeda, G. Spahlinger, R. Kopelman, and R. J. Buckanovich, *Cancer research*, 2010, **70**, 8674–83.

44. K. Porkka, P. Laakkonen, J. A. Hoffman, M. Bernasconi, and E. Ruoslahti, *Proceedings of the National Academy of Sciences of the United States of America*, 2002, **99**, 7444–9.
45. N. Panté and M. Kann, *Molecular biology of the cell*, 2002, **13**, 425–34.
46. A. Ray, Y.-E. Koo Lee, T. Epstein, G. Kim, and R. Kopelman, *The Analyst*, 2011, **136**, 3616–22.
47. A. Ray, Y.-E. K. Lee, G. Kim, and R. Kopelman, *Small (Weinheim an der Bergstrasse, Germany)*, 2012, **8**, 2213–21.
48. B. Wang, L. Zhang, S. C. Bae, and S. Granick, *Proceedings of the National Academy of Sciences of the United States of America*, 2008, **105**, 18171–5.
49. J. Liu, M. Kaksonen, D. G. Drubin, and G. Oster, *Proceedings of the National Academy of Sciences of the United States of America*, 2006, **103**, 10277–82.
50. W. Jiang, B. Y. S. Kim, J. T. Rutka, and W. C. W. Chan, *Nature nanotechnology*, 2008, **3**, 145–50.
51. H. Yuan, J. Li, G. Bao, and S. Zhang, *Physical Review Letters*, 2010, **105**, 1–4.
52. A. G. Hovanessian, C. Soundaramourty, D. El Khoury, I. Nondier, J. Svab, and B. Krust, *PloS one*, 2010, **5**, e15787.
53. X. Chen, D. M. Kube, M. J. Cooper, and P. B. Davis, *Molecular therapy : the journal of the American Society of Gene Therapy*, 2008, **16**, 333–42.
54. D. A. Orringer, Y.-E. L. Koo, T. Chen, G. Kim, H. J. Hah, H. Xu, S. Wang, R. Keep, M. A. Philbert, R. Kopelman, and O. Sagher, *Neurosurgery*, 2009, **64**, 965–71; discussion 971–2.
55. M. Ekkapongpisit, A. Giovia, C. Follo, G. Caputo, and C. Isidoro, *International journal of nanomedicine*, 2012, **7**, 4147–58.
56. P. J. Smith, M. Giroud, H. L. Wiggins, F. Gower, J. a Thorley, B. Stolpe, J. Mazzolini, R. J. Dyson, and J. Z. Rappoport, *International journal of nanomedicine*, 2012, **7**, 2045–55.
57. D. Legrand, K. Vigie, E. a. Said, E. Elass, M. Masson, M.-C. Slomianny, M. Carpentier, J.-P. Briand, J. Mazurier, and A. G. Hovanessian, *European Journal of Biochemistry*, 2004, **271**, 303–317.
58. L. Pelkmans, T. Bürli, M. Zerial, and A. Helenius, *Cell*, 2004, **118**, 767–80.
59. W. Querbes, B. a O'Hara, G. Williams, and W. J. Atwood, *Journal of virology*, 2006, **80**, 9402–13.
60. A. G. Hovanessian, F. Puvion-Dutilleul, S. Nisole, J. Svab, E. Perret, J. S. Deng, and B. Krust, *Experimental cell research*, 2000, **261**, 312–328.
61. S. R. Carlsson and M. Fukuda, *Archives of biochemistry and biophysics*, 1992, **296**, 630–9.
62. W. Hunziker and H. J. Geuze, *BioEssays : news and reviews in molecular, cellular and developmental biology*, 1996, **18**, 379–89.
63. K. Janvier and J. S. Bonifacino, *Molecular biology of the cell*, 2005, **16**, 4231–42.
64. K. K. Huynh, E.-L. Eskelinen, C. C. Scott, A. Malevanets, P. Saftig, and S. Grinstein, *The EMBO journal*, 2007, **26**, 313–24.
65. M. Barel, K. Meibom, and A. Charbit, *PloS one*, 2010, **5**, e14193.
66. O. Saitoh, W. C. Wang, R. Lotan, and M. Fukuda, *The Journal of biological chemistry*, 1992, **267**, 5700–11.
67. S. F. Siddiqui, J. Pawelek, T. Handerson, C.-Y. Lin, R. B. Dickson, D. L. Rimm, and R. L. Camp, *Cancer epidemiology, biomarkers & prevention : a publication of the American Association for Cancer Research, cosponsored by the American Society of Preventive Oncology*, 2005, **14**, 2517–23.

68. S. K. Khaldoyanidi, V. V Glinsky, L. Sikora, A. B. Glinskii, V. V Mossine, T. P. Quinn, G. V Glinsky, and P. Sriramarao, *The Journal of biological chemistry*, 2003, **278**, 4127–34.
69. T. dos Santos, J. Varela, I. Lynch, A. Salvati, and K. a Dawson, *PloS one*, 2011, **6**, e24438.
70. T. A. Gottlieb, I. E. Ivanov, M. Adesnik, and D. D. Sabatini, *The Journal of cell biology*, 1993, **120**, 695.
71. S. Bolte and F. P. Cordelières, *Journal of microscopy*, 2006, **224**, 213–32.

Appendix

A3.1 Effect of Potassium Depletion on Subcellular Localization of F3 Peptide

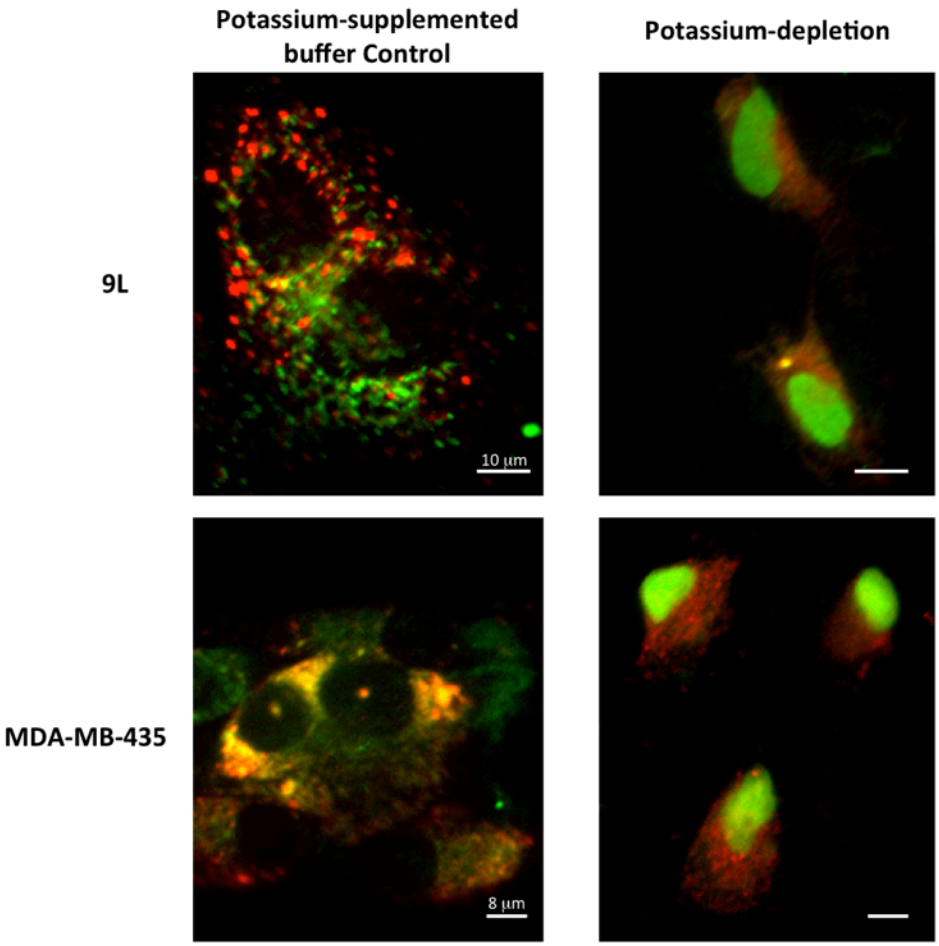

Figure A3.1 Effect of potassium depletion induced inhibition of clathrin-mediated endocytosis on the subcellular localization of F3 peptide in nucleolin-overexpressing 9L rat gliosarcoma and MDA-MB-435 human melanoma cell lines. As observed for 9L and MDA-MB-435 cells treated with Chlorpromazine, a pharmacological inhibitor of clathrin-mediated endocytosis (Figs. 3.1.1.c and 3.2.1.c), potassium-depletion promoted the accumulation of FITC-labeled F3 peptide (green) within the nuclei of both 9L and MDA-MB-435 cells. In the control 9L and MDA-MB-435 cells however, which were treated with potassium-supplemented HEPES buffer, F3 peptide was sequestered either in endosomes, or lysosomes (labeled with Lysotracker Red DND-99) as denoted by regions of yellow fluorescence.

A3.2 Endocytic Inhibitor Cytotoxicity Assays

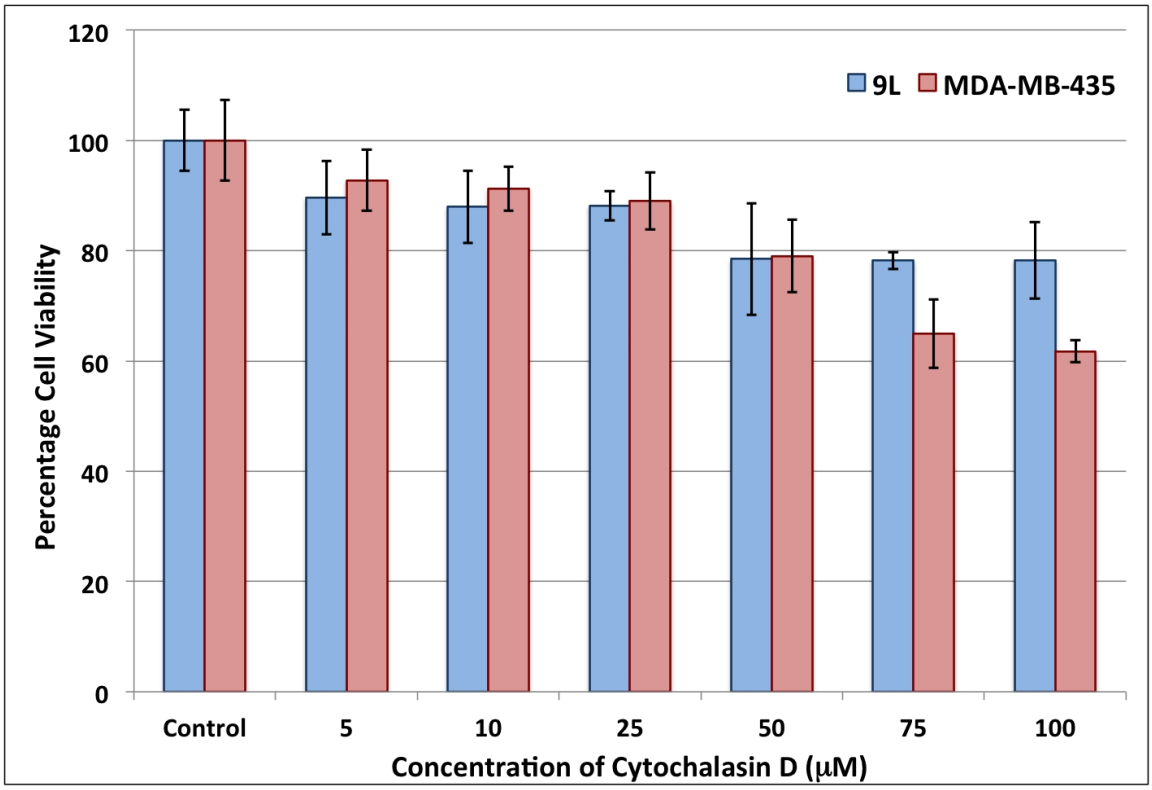

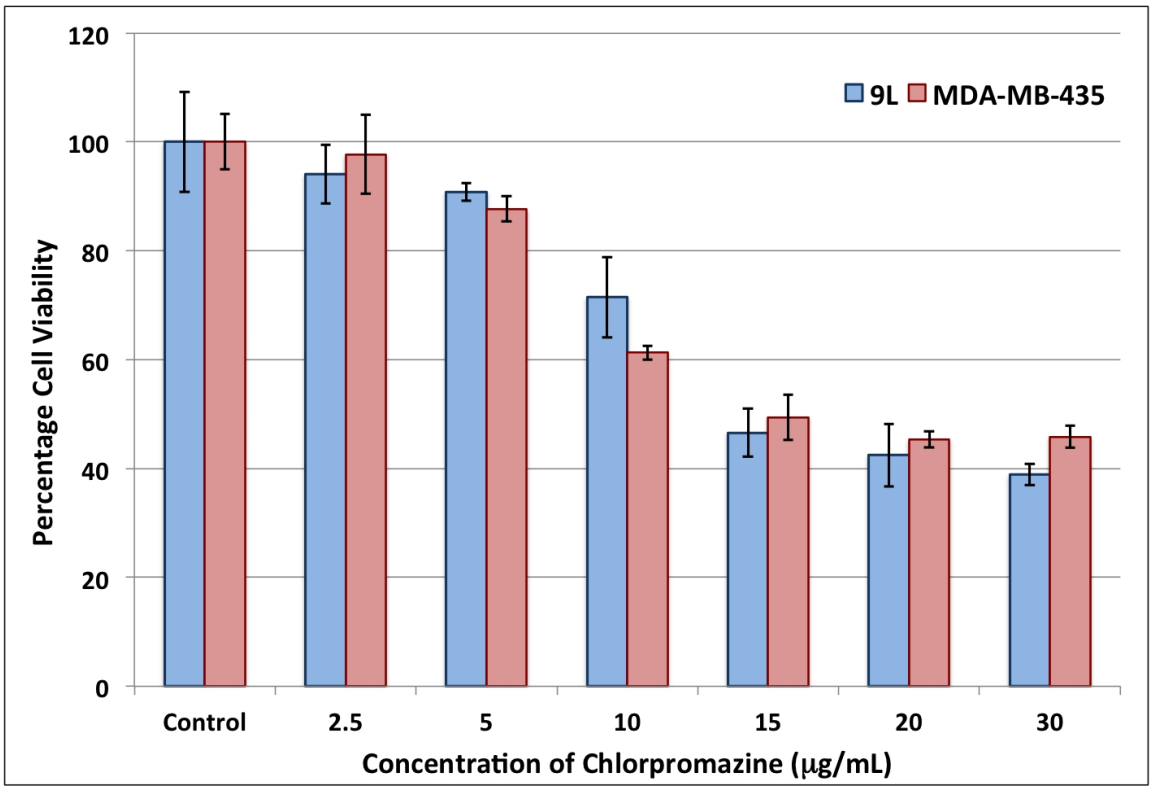

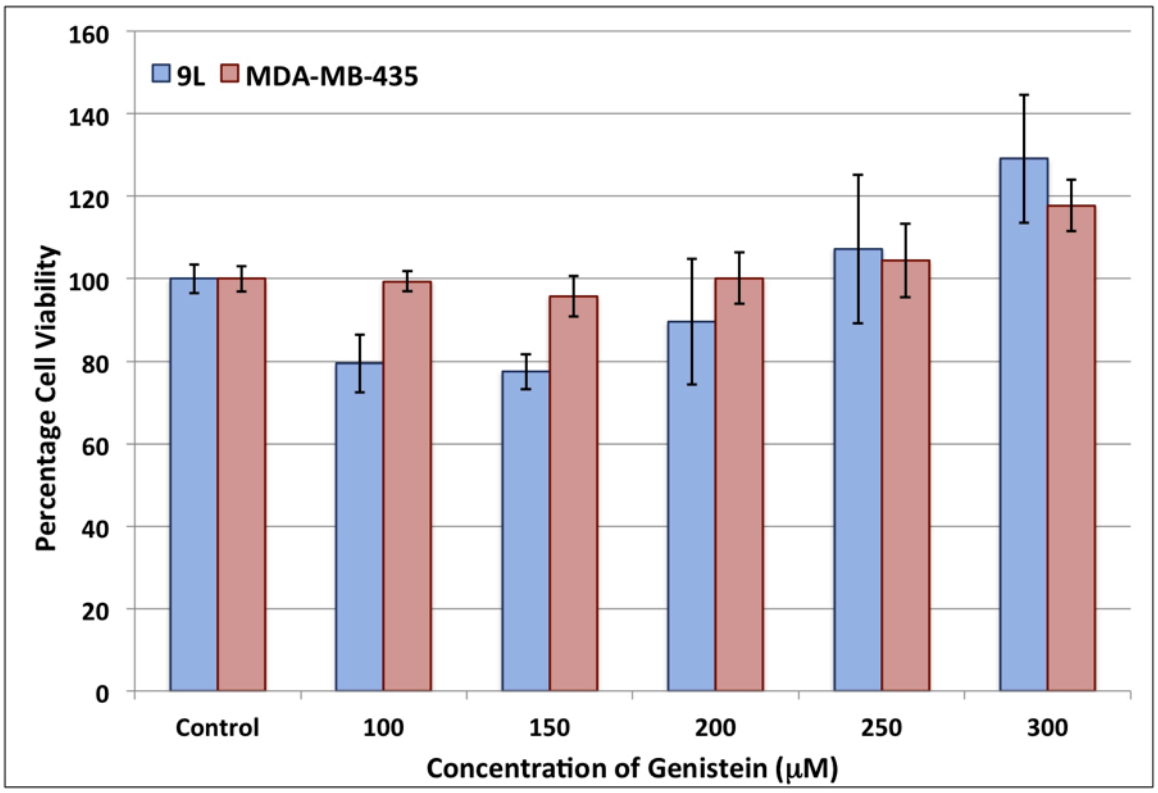

Figure A3.2.1-3.3.3 Cytotoxicity profiles of Cytochalasin D (CD), Chlorpromazine (CPZ) and Genistein (GEN), respectively, in the 9L and MDA-MB-435 cell lines, as determined by the Methylthiazol tetrazolium (MTT) microtiter assay. All drug incubations were performed for 90 minutes, at 37 °C, prior to delivery of the MTT reagent to the cells. This inhibitor incubation period was used for all subsequent endocytosis inhibition assays. Maximal concentrations of 50 μM, 10 $\mu g.mL^{-1}$, and 200 μM, for CD, CPZ and GEN, respectively, were selected for the endocytosis inhibition assays. In the cases of CD and CPZ, concentrations higher than the abovementioned values were avoided for the endocytosis inhibition assays so as to limit cytotoxicity. Furthermore, concentrations higher than 50 μM CD adversely affected the morphology of both 9L and MDA-MB-435 cells. For GEN, concentrations higher than 200 μM enhanced the viability of both 9L and MDA-MB-435 cells, and were thus avoided, so as to prevent potential stimulation of the F3 peptide or nanoparticle uptake by other endocytic pathways in the presence of GEN. Interestingly, GEN reduced the viability of 9L cells up to 200 μM, but increased their viability, as well as that of the MDA-MB-435 cells, above that of the control cells (107% and 129% for 9L; 104% and 118% for MDA-MB-435) at 250 and 300 μM respectively. A similar trend was reported for GEN in other cell lines.[1] All values are represented as means of quadruplicate wells ± SD.

Experimental Section

Methylthiazol tetrazolium (MTT) Assay of Endocytic Inhibitor Cytotoxicity

Suspensions of 9L and MDA-MB-435 cells, prepared in 10% FBS-supplemented RPMI-1640 and DMEM 11965 media respectively, were seeded into the wells of separate Corning 96-well microtiter plates at approximately 10,000 cells per well, and allowed to attach to the wells for 24 hours at 37 °C in 5% CO_2 humidified atmosphere prior to initiating treatment with the endocytic inhibitors, Cytochalasin D (CD), Chlorpromazine (CPZ) and Genistein (GEN). All inhibitors were prepared in DMSO as 100-fold concentrated stocks, and tested in quadruplicate at the following final concentrations; CD: 5, 10, 25, 50, 75 and 100 μM; CPZ: 2.5, 5, 10, 15, 20 and 30 μg/mL; GEN: 100, 150, 200, 250 and 300 μM. Importantly, all drugs were diluted to the above final concentrations in either RPMI-1640 or DMEM 11965 media such that all dilutions contained equal concentrations of DMSO, which did not exceed 1% v/v. At the start of the assay, all microtiter wells were aspirated of their original culture media and refilled with 200 μL of the appropriate culture medium containing either CD, CPZ or GEN at one of the above concentrations. The vehicle controls constituted 9L and MDA-MB-435 cells treated only with 1% v/v DMSO. The cell lines were then incubated with endocytic inhibitors for 90 min at 37 °C in 5% CO_2 humidified atmosphere. At the end of incubation, all microtiter wells were aspirated of their culture media and replenished with 100 μL of either phenol red-free RPMI-1640 without FBS (for 9L cells) or phenol red-free DMEM culture media without FBS (for MDA-MB-435 cells). Thereafter, 20 μL of 5 mg/mL MTT stock solution (prepared in either phenol red-free RPMI or DMEM media) was added to each well and mixed, followed by further incubation for 4 hours at 37 °C in 5% CO_2 humidified atmosphere. At the end of incubation, the culture media were

carefully aspirated from all wells and the purple MTT formazan product in each well was solubilized by addition of 200 μL 100% DMSO solvent, followed by agitation on a rocking shaker overnight at room temperature. Absorbance readings were taken the following day at 550 nm (620 nm reference).

Potassium depletion Assay

Suspensions of 9L and MDA-MB-435 cells, prepared in 10% FBS-supplemented RPMI-1640 and DMEM 11965 media respectively, were seeded into the wells of 8-chambered No. 1 microscopy coverglasses (MatTek Corporation) at approximately 25,000 cells per well and allowed to attach to the coverglasses for 24 hours at 37 °C in 5% CO_2 humidified atmosphere prior to initiating the assay. At the start of the assay, all wells were aspirated of their culture media. Thereafter, the wells containing either 9L or MDA-MB-435 cells designated for potassium depletion were washed once with potassium-depletion buffer (20 mM HEPES, 140 mM NaCl, 1 mM $CaCl_2$, 1mM $MgCl_2$, 1 mg/mL D-glucose) and incubated in hypotonic potassium depletion buffer (1:1 ratio of potassium depletion buffer: dH_2O) for 5 minutes at 37 °C. Thereafter, the potassium-depletion wells were washed three times with potassium-depletion buffer, and the cells subsequently incubated with FITC-labeled F3 peptides (0.1 mg/mL) for a further 30 minutes at 37 °C in the same buffer. The control 9L and MDA-MB-435 cells were subjected to the same treatment protocol except with potassium-supplemented buffer (potassium depletion buffer supplemented with 10 mM KCl). At the end of the incubation, all cells were labeled with Lysotracker Red DND-99 (300 nM for 5 minutes at 37 °C). The potassium-depletion and control wells were subsequently washed three times with their respective buffers to remove excess F3 peptides and Lysotracker Red DND-99. The potassium-depletion and control treatments were performed in triplicate for each cell line. The cells were imaged on an Olympus

inverted disc-spinning confocal microscope, equipped with an environmental chamber and Semrock BrightLine® Sedat filter set, using a 40x oil-immersion lens. The FITC and TRITC filters were used to excite the FITC-F3 peptides and Lysotracker Red DND-99 fluorophore respectively.

References

1. D. Vercauteren, R. E. Vandenbroucke, A. T. Jones, J. Rejman, J. Demeester, S. C. De Smedt, N. N. Sanders, and K. Braeckmans, *Molecular Therapy,* 2010, **18**, 561-569.

Chapter 4

Modulation of MAPK signaling profiles by non-targeted and multivalent tumor-targeting hydrogel nanoparticles in breast adenocarcinoma

4.1 Introduction

Multifunctional nanoparticles (NP) form the basis of modern cancer-targeted nanoscale theranostics, and incorporate the potential for surface functionalizations with the capacity to carry a diverse range of molecular payloads for various therapeutic and diagnostic modalities.[1,2] Polymeric hydrogels, in particular, have been employed successfully as nanoscale theranostic agents.[3,4] The physicochemical properties of a hydrogel NP, namely: size,[5–7] morphology,[8,9] polymer elasticity,[10] surface charge[11–13] and surface chemical functionalizations[14] collectively influence the pathway of internalization, and of subcellular localization of the NP within the tumor cell.[15] In turn, this can directly influence the efficacy of chemotherapeutic drugs. Multivalent surface functionalization of hydrogel NPs with targeting moieties – specific toward a particular cell-surface receptor uniquely overexpressed on tumor cells – is exploited to enhance the hydrogel NP's binding affinity for the target tumor cell, and promote receptor-mediated endocytosis of the targeted NP.[16,17] Importantly, however, it cannot be assumed that the multivalent ligand-targeted hydrogel NP will undergo intracellular trafficking identical to that of the monovalent ligand alone, or the non-targeted NP, for that matter.

We recently demonstrated that multivalent surface functionalization of polyacrylamide (PAA)

hydrogel NPs with the Nucleolin-binding $F3_{wt}$ peptide (wild-type sequence: KDEPQRRSARLSAKPAPPKPEPKPKKAPAKKC) modulates the intracellular trafficking, and the subcellular localization of the targeted PAA-NPs ($F3_{wt}$NP), relative to the non-targeted PAA-NPs (NTNPs), and to the monovalent $F3_{wt}$ peptide targeting ligand alone.[14] Specifically, the $F3_{wt}$NPs exhibited significantly lower trafficking to the lysosomes (acidic, degradative vesicles of the cell) than either the NTNPs, or the monovalent $F3_{wt}$ peptide alone, in Nucleolin-overexpressing tumor cells (9L and MDA-MB-435). Furthermore, the $F3_{wt}$NPs exhibited significantly lower colocalization with Caveolin-1 than the NTNPs, particularly at 2 and 3 hours after delivery of both types of PAA-NPs to MDA-MB-435 cells. The difference in intracellular trafficking of the $F3_{wt}$NPs compared to the NTNPs was remarkable, given that the clathrin- and caveolae-mediated endocytic pathways predominantly facilitated internalization of both types of PAA-NPs. These observations suggested that the $F3_{wt}$NPs and NTNPs likely elicit different cell signaling profiles that directly influence their mechanism of internalization and intracellular trafficking.

In particular, the p38 Mitogen-Activated Protein Kinases (MAPKs) have been shown to enhance the rate of clathrin-mediated endocytosis by phosphorylating Early Endosomal Antigen 1 (EEA1), a protein located in the membranes of early endosomes, specifically on residue Threonine-1392 (Thr/T-1392) (Fig. 4.1).[18] EEA1 is essential for the mediating the homotypic fusion between different early endosomes,[19] and Thr-1392-phosphorylation of EEA1 prevents such homotypic fusion. As a result, the early endosomes bearing Thr-1392-phosphorylated EEA1 rapidly mature into late endosomes. This process is further promoted by the exchange of Rab5 GTPase in the early endosome membranes with Rab7 GTPase,[20] the latter of which catalyzes fusion of the late endosomes with lysosomes.[21,22] In addition, the phosphorylation of

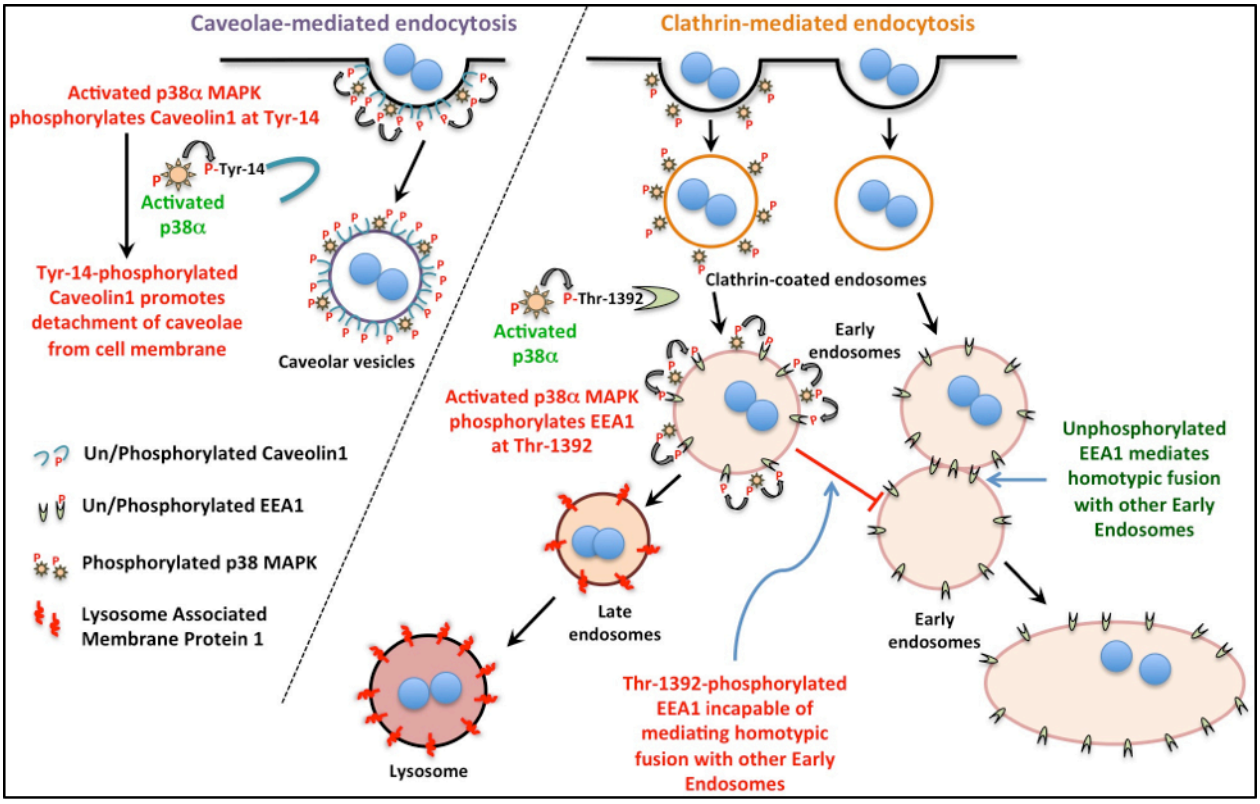

Fig. 4.1 Schematic diagram depicting the mechanisms by which the activated (dual-phosphorylated) p38 MAPKs modulate intracellular trafficking via the caveolae-mediated (left) and clathrin-mediated (right) endocytic pathways, by directly phosphorylating Caveolin-1 at Tyrosine-14 (Tyr-14), and Early Endosome Antigen-1 (EEA1) at Threonine-1392 (Thr-1392), respectively.

the N-terminus of Caveolin-1α at Tyrosine-14 (Tyr/Y-14), by the activated p38 MAPKs,[23] has been shown to promote the scission of caveolae from the cell membrane, thus promoting their internalization from the cell surface (Fig. 4.1).[24] Hence, the activation of the p38 MAPK pathway exerts a direct, and important regulatory role on both the clathrin- and caveolae-mediated endocytic pathways.

Recent studies have demonstrated the potential of a broad range of nanomaterials to activate the p38, as well as the extracellular-regulated signal kinase (ERK) and c-Jun N-terminal kinase (JNK) MAPK pathways, upon interaction with cell surface receptors.[25,26] However, a precise understanding of how a multivalent, ligand-functionalized hydrogel NP modulates the abovementioned MAPK pathways in target cells, relative to its non-targeted counterpart *exhibiting similar size and surface charge properties*, has been lacking to date. In the present

study, we tested the hypothesis that the $F3_{wt}$NPs induce lower levels of phosphorylated p38 MAPKs than the NTNPs, as a plausible mechanism, by which the $F3_{wt}$NPs exhibit markedly lower (i) lysosomal-accumulation, and (ii) colocalization with Caveolin-1, than the NTNPs, in MDA-MB-435 breast adenocarcinoma cells. Moreover, activation of the ERK pathway promotes cell survival and proliferation, which is antagonized by the p38 and JNK pathways, the latter two MAPKs being typically pro-apoptotic signaling phosphoproteins. Crucially, the ratio of phosphorylated ERK (p-ERK) to phosphorylated p38 (p-p38) has been shown to determine whether a cell proliferates, or undergoes apoptosis. We therefore performed a comprehensive phosphoproteomic analysis of the ERK, p38 and JNK MAPK pathways, including the Akt pathway (a mitogenic pathway), and their key downstream targets in MDA-MB-435 cells, so as to elucidate how each of the $F3_{wt}$NPs, NTNPs, and the $F3_{wt}$ peptide, modulate the MAPK signaling profile of the tumor cells. Furthermore, we discuss the implications of the distinct signaling profiles, elicited by these different treatments, on the survival status of the tumor cell, as well as present plausible mechanisms by which each of these signaling profiles is induced.

4.2 Results and Discussion

4.2.1 Phospho-p38α MAPK ELISA

Four isoforms of p38 MAPK, p38α, p38β, p38γ and p38δ, are expressed in human tissue. In all p38 isoforms, dual phosphorylation of the Threonine (Thr/T) 180 and Tyrosine (Tyr/Y) 182 residues (pT180/pY182) in the Thr-Gly-Tyr motif of the activation loop, by the upstream MAP kinase kinases (MAP2Ks) MKK3 and MKK6, is required for complete activation.[27] Since the role of the p38α isoform in phosphorylating EEA1 at Thr-1392 has been well characterized,[18] we initially determined the phosphorylation status of p38α in MDA-MB-435 cells, by phospho-

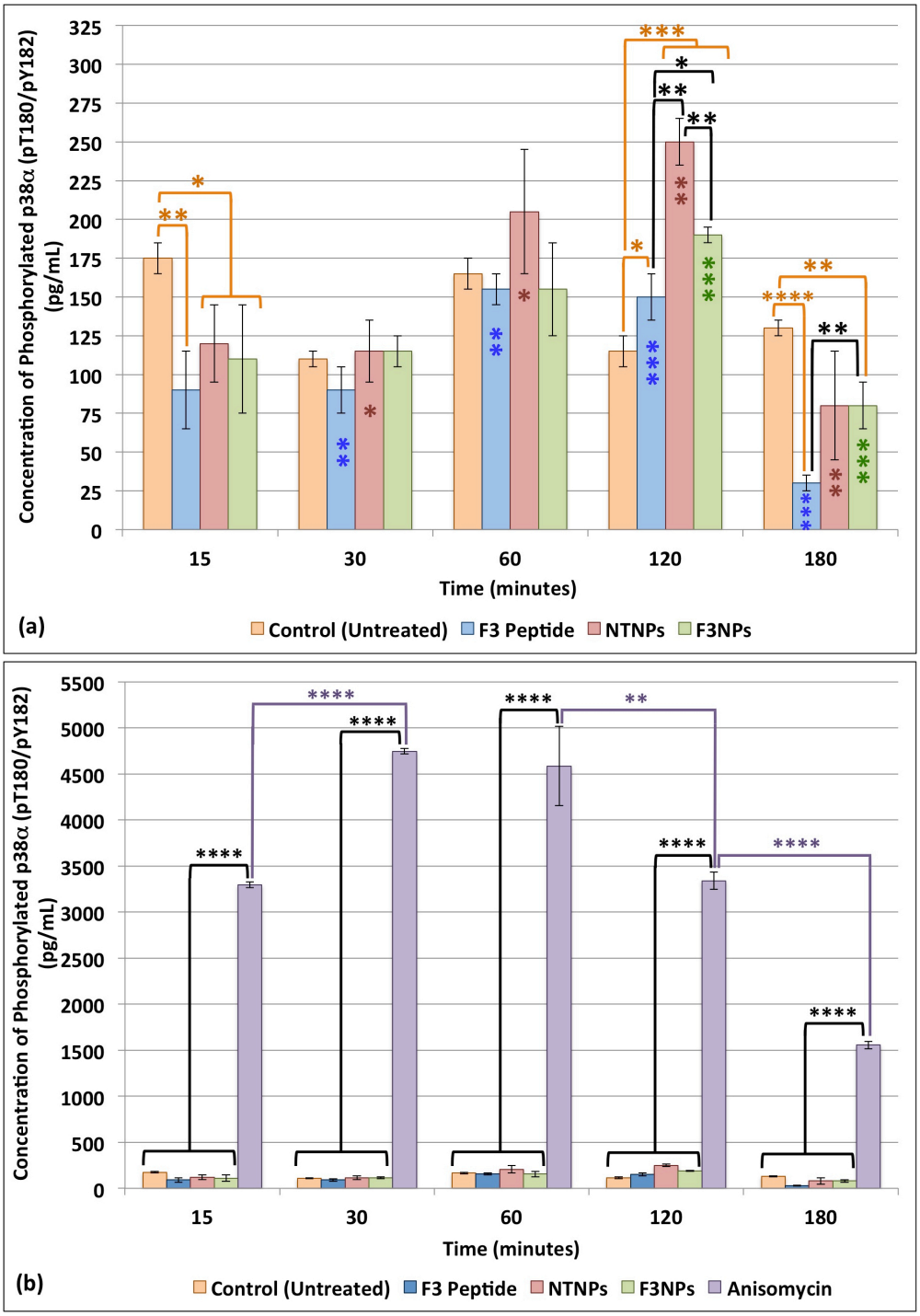

Fig. 4.2 Time-dependent change in concentration of phosphorylated p38α MAPK (pT180/pY182) in MDA-MB-435 cells in response to treatment with (4.2a) $F3_{wt}$ peptide (0.22 mg/mL), NTNPs (1 mg/mL), $F3_{wt}$NPs (1 mg/mL), and (4.2b) Anisomycin (10 μg/mL), a potent inducer of p38 MAPK phosphorylation. Histograms represent means ± standard deviations of two experiments. *P*-values denote: $P<0.05$ (*), $P<0.01$ (**), $P<0.001$ (***), $P<0.0001$ (****). Black brackets denote significant difference between different treatments at a specific time-point. Orange brackets denote significant difference between the untreated control and different treatments. Columns bearing identical numbers of similarly colored asterisks are significantly different from each other (4.2a). Purple brackets denote significant difference between consecutive Anisomycin treatments of different durations (4.2b).

p38α sandwich ELISA, in response to either (i) $F3_{wt}$ peptide alone (0.22 mg/mL), (ii) NTNPs (1 mg/mL) or (iii) $F3_{wt}$NPs (1 mg/mL), relative to the control (untreated) MDA-MB-435 cells (Fig. 4.2a). The $F3_{wt}$ peptide and the $F3_{wt}$NPs treatments induced gradual time-dependent up-regulation in the phosphorylated p38α (p-p38α) concentration, with maxima occurring at 1 hour and 2 hours post-delivery, respectively, followed by marked down-regulation in p-p38α concentrations at 3 hours post-delivery for both treatments (P<0.001, 2-hour vs. 3-hour p-p38α concentrations for both $F3_{wt}$ peptide and $F3_{wt}$NPs). In contrast, the NTNPs elicited a steeper up-regulation in p-p38α phosphorylation, achieving maximal p-p38α concentration at 2 hours post-delivery, followed also by a marked down-regulation at 3 hours post-delivery (P<0.01, 2-hour vs. 3-hour concentrations). Notably, significant differences between all three treatments ($F3_{wt}$ peptide alone, NTNPs and $F3_{wt}$NPs) were observed only at 2-hours post-delivery; the NTNP-induced p-p38α concentration at this time-point was 1.67-fold and 1.32-fold higher than in the $F3_{wt}$ peptide, and $F3_{wt}$NPs treatments, respectively (P<0.01), while the $F3_{wt}$NP-induced p-p38α concentration was 1.27-fold greater than for the $F3_{wt}$ peptide alone treatment (P<0.05) (Fig. 4.2a). Furthermore, the p-p38α concentrations in all three treatments were significantly higher than the untreated control only at 2-hours; the $F3_{wt}$ peptide, NTNP and $F3_{wt}$NPs treatments induced 1.30-fold, 2.17-fold and 1.65-fold higher p-p38α concentrations, respectively, than in the control (Fig. 4.2a). We also confirmed the activity of the p38 pathway in MDA-MB-435 cells with Anisomycin (10 μg/mL), a known potent activator of p38 MAPKs (Fig. 4.2b). The p38 pathway in MDA-MB-435 cells is indeed responsive to external stimuli with Anisomycin being a clearly more potent activator of p38α than the $F3_{wt}$ peptide, NTNPs and $F3_{wt}$NPs. Nonetheless, all treatments only transiently activated p38α, which is consistent with the deactivation of phosphorylated p38 MAPKs by phosphatase enzymes, such as PP2C (Ser/Thr phosphatase).[28,29]

In our previous intracellular trafficking study in MDA-MB-435 cells, the $F3_{wt}$ peptide and NTNPs exhibited 6.4-fold and 3.3-fold higher colocalization with Lysotracker Red (a lysosome-specific fluorophore), respectively, than the $F3_{wt}$NPs,[14] which cannot be explained solely by the respective p38α phosphorylation profiles of the $F3_{wt}$ peptide, NTNPs and $F3_{wt}$NPs as observed in this study. Thus, our previously reported intracellular trafficking data of the $F3_{wt}$ peptide, NTNPs and $F3_{wt}$NPs, taken into account with their corresponding p38α phosphorylation profiles, led us to consider the possibility of the p38β, p38γ and/or p38δ isoforms being more influential than the p38α isoform alone, on the intracellular trafficking of the $F3_{wt}$ peptide, NTNPs and $F3_{wt}$NPs.

4.2.2.1 Phosphoproteomic Arrays (p38 MAPK Pathway)

Using MAPK phosphoproteomic arrays with pre-selected phospho-specific antibodies (Appendix A4.2), we then determined the phosphorylation status of all four p38 isoforms, including 20 other signaling proteins belonging to the ERK, JNK and Akt pathways, in response to either the $F3_{wt}$ peptide alone, NTNPs, or $F3_{wt}$NPs (Appendix A4.2). In addition, the phosphorylation profiles of these proteins were determined in response to treatment with scrambled-F3NPs ($F3_{scram}$NPs; PAA-NPs surface functionalized with the scrambled-F3 sequence, PKAARALPSQRSRPPEKAKKPPDKPAPEKKKC) as a further control to the $F3_{wt}$NPs. Notably, the $F3_{scram}$NPs share similar physicochemical characteristics with the $F3_{wt}$NPs in terms of hydrodynamic radius, and surface charge (NP hydrodynamic radius and zeta potential characterizations presented in Appendix A4.1). More crucially, however, the $F3_{scram}$NPs also mimicked the surface chemical properties (multivalency) of the $F3_{wt}$NPs, as their surfaces were

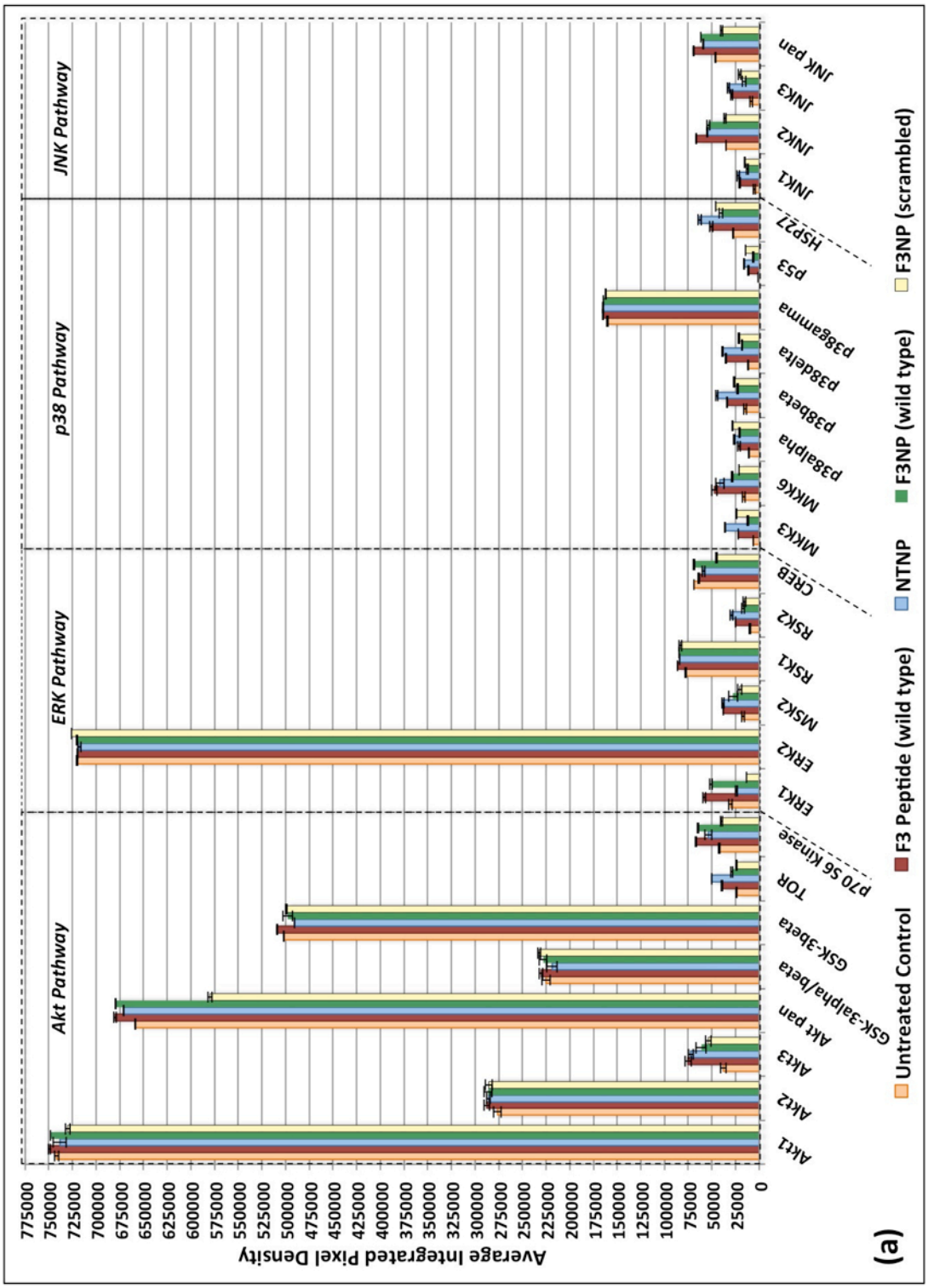

Fig. 4.3a Complete phosphoproteomic profiles of Akt, ERK, p38 and JNK pathway signaling proteins isolated from MDA-MD-435 cells treated with $F3_{wt}$ peptide, NTNPs, $F3_{wt}$NPs and $F3_{scram}$NPs for 2 hours. Notably, Akt1, Akt2, Akt pan, Glycogen Synthase Kinase (GSK)-3α/β, GSK-3β, ERK2, and p38γ exhibited markedly higher basal phosphorylation levels than the other kinases. All treatments were repeated three times, and protein isolates from all three replicates of a specific treatment were pooled and probed on separate Phospho-Proteome MAPK array membranes. Histograms represent means ± standard deviations obtained from measurements of duplicate spots for each protein probed on the array membrane (See Appendix Fig. A4.2).

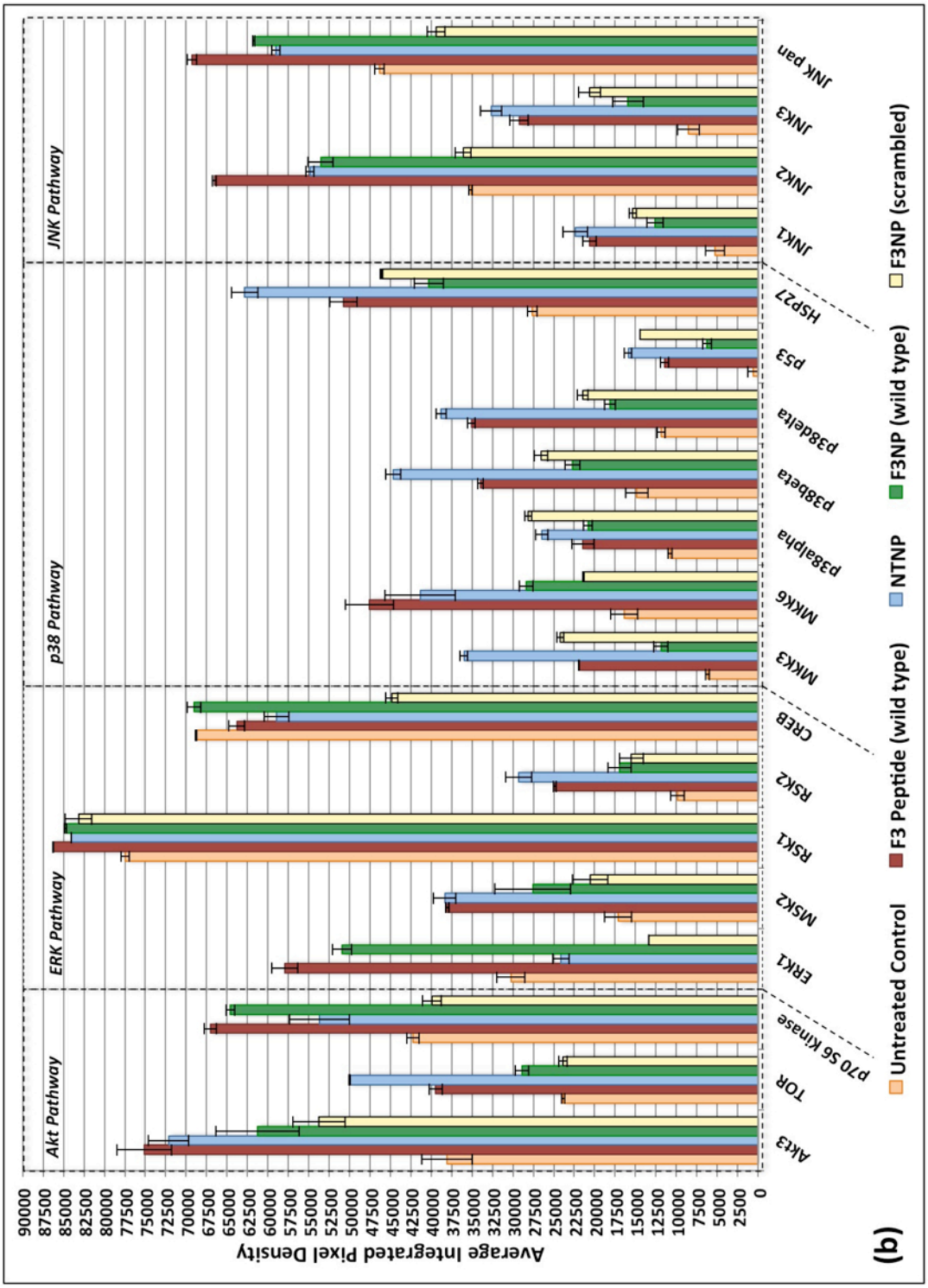

Fig. 4.3b Partial phosphoproteomic profiles of Akt, ERK, p38 and JNK pathway signaling proteins isolated from MDA-MD-435 cells treated with $F3_{wt}$ peptide, NTNPs, $F3_{wt}$NPs and $F3_{scram}$NPs treated for 2 hours. Notably, Akt1, Akt2, Akt pan, Glycogen Synthase Kinase (GSK)-3α/β, GSK-3β, ERK2, and p38γ exhibited markedly higher basal phosphorylation levels than the other kinases. Hence, a partial phosphoproteomic profile of the Akt, ERK, p38 and JNK pathways from which signals for Akt1, Akt2, Akt pan, GSK-3α/β, GSK-3β, ERK2, and p38γ have been omitted so as to clearly illustrate the profiles of the kinases that exhibited lower levels of phosphorylation. Histograms represent means ± standard deviations obtained from measurements of duplicate spots for each protein probed on the array membrane (See Appendix Fig. A4.2).

functionalized with flexible polyethylene glycol (PEG) molecules, to which multiple peptides that bear identical amino acid composition, and charge to the $F3_{wt}$ peptides, albeit without binding specificity toward the Nucleolin receptors, were conjugated. All treatments were performed at the optimal duration of 2-hours, as determined by phospho-p38α sandwich ELISA (Fig. 4.2a). Of the four p38 isoforms, p38γ (pT183/pY185) exhibited the highest basal phosphorylation level in the untreated control (average of 13.07-fold higher than basal p-p38α, β and δ isoforms) which, however, did not vary significantly from the basal phosphorylation level in response to any of the different treatments (Figs. 4.3a, Table 4.1, Appendix A4.3.2). In contrast, the various treatments elicited more pronounced differences in the p-p38β (pT180/pY182) and p-p38δ (pT180/pY182) levels, as compared to the p-p38α isoform (Fig. 4.3b, Table 4.1). In ascending order, the p-p38β, and p-p38δ levels were up-regulated, relative to the untreated control, as follows, (i) $F3_{wt}$NPs: 1.53-fold for both p38β and p38δ isoforms, (ii) $F3_{scram}$NPs: 1.79-fold and 1.81-fold respectively, (iii) $F3_{wt}$ peptide: 2.29-fold and 2.96-fold respectively, and (iv) NTNPs: 3.01-fold and 3.27-fold respectively (Table 4.1). In this assay, the up-regulation in p-p38α levels by the $F3_{wt}$ peptide (1.99-fold) and $F3_{wt}$NPs (1.94-fold) were nearly identical, while the NTNPs and $F3_{scram}$NPs induced 2.46-fold and 2.61-fold increases in p-p38α levels, respectively (Fig. 4.3b, Table 4.1). Although the array-derived fold-enhancements in p-p38α levels were higher than that observed in the p-p38α ELISA assay for the corresponding treatments, the ratio of p-p38α level enhancements particularly between the NTNPs and $F3_{wt}$NPs, essentially remained unchanged (~1.30-fold). Notably, the absolute p-p38α, β and δ levels induced by the $F3_{wt}$NPs were reasonably consistent (Fig. 4.3b), however the $F3_{wt}$ peptides alone, and NTNPs elicited markedly higher p-p38β and p-p38δ levels as compared to their corresponding p-p38α levels (Fig. 4.3b). Also, the $F3_{scram}$NPs elicited consistently higher

p-p38α, β and δ levels than the $F3_{wt}$NPs. The possible reason for this observation will be discussed further on.

Table 4.1 Summary of the fold changes in the phosphorylation levels of the MAP2K phosphoproteins, MKK3 and MKK6, and the phosphorylation levels of the downstream p38α, β, δ and γ MAPK isoforms, elicited by the various treatments relative to the untreated control

Phosphoprotein/ ***Phosphorylation sites detected***	**Untreated Control**	**$F3_{wt}$ Peptide**	**NTNPs**	**$F3_{wt}$NPs**	**$F3_{scram}$NPs**
MKK3 *(pS218/pT222)*	1.00	3.53	5.80	1.92	3.90
MKK6 *(pS207/pT211)*	1.00	2.90	2.52	1.73	1.31
p38α *(pT180/pY182)*	1.00	1.99	2.46	1.94	2.61
p38β *(pT180/pY182)*	1.00	2.29	3.01	1.53	1.79
p38δ *(pT180/pY182)*	1.00	2.96	3.27	1.53	1.81
p38γ *(pT183/pY185)*	1.00	1.03	1.03	1.03	1.01

Table 4.2 Summary of the correlation strength between the phosphorylation levels of the MAP2K phosphoproteins, MKK3 and MKK6, and the phosphorylation levels of the p38α, β, and δ MAPK isoforms

Phosphorylated MAP2K vs. Phosphorylated p38 MAPK	**Correlation Strength (Linear correlation coefficient (R^2))**
pMKK3 vs. p-p38α	0.691
pMKK3 vs. p-p38β	0.897
pMKK3 vs. p-p38δ	0.764
pMKK6 vs. p-p38α	0.165
pMKK6 vs. p-p38β	0.675
pMKK6 vs. p-p38δ	0.843
Average p-MKK3/6 vs. p-p38α	0.449
Average p-MKK3/6 vs. p-p38β	0.953
Average p-MKK3/6 vs. p-p38δ	0.991

The phosphorylation levels of the upstream MAP2K enzyme MKK3 exhibited stronger linear correlations than MKK6 with the p-p38α (R^2 coefficient: 0.691) and p-p38β (R^2 coefficient: 0.897) levels (Table 4.2, Appendix A4.4.1), whereas the phosphorylation levels of MKK6 correlated better than MKK3 with p-p38δ levels (R^2 coefficient: 0.843; Table 4.2, Appendix A4.4.1). Overall, strong linear correlations were observed between the average MKK3/6 phosphorylation levels, and the p-p38β (R^2 coefficient: 0.953) and p-p38δ (R^2 coefficient: 0.991) levels (Table 4.2, Appendix A4.4.2), however the correlation between the average MKK3/6 phosphorylation levels and the p-p38α levels was weaker (R^2 coefficient: 0.449; Table 4.2, Appendix A4.4.2). Given that the MKK3 and MKK6 enzymes lie directly upstream of the p38 isoforms in the p38 MAPK signaling cascade, these data suggest that the signals generated by the $F3_{wt}$ peptide, NTNP, $F3_{wt}$NPs and $F3_{scram}$NPs treatments are channeled by MKK3 and MKK6 preferentially to the p38β and p38δ isoforms, in MDA-MB-435 cells. However, of these two p38 isoforms, it is likely that p38β predominantly phosphorylates EEA1 at its Thr-1392 residue. This is supported by, (i) the observation that the p38β isoform, in addition to p38α, is responsible for phosphorylating EEA1 at its Thr-1392 residue,[18] and (ii) the p38δ isoform likely having lower substrate specificity for EEA1 at the location of the Thr-1392 residue. The latter point can be explained by the fact that the p38β isoform has 75% amino acid sequence identity to the p38α isoform, while the p38δ isoform has only 61% sequence identity to the p38α isoform.[30]

In our previously reported intracellular trafficking study with our NTNPs and $F3_{wt}$NPs in MDA-MB-435 cells, the NTNPs and $F3_{wt}$NPs both achieved similar peak colocalization levels with EEA1-positive endosomes (~32%) at 30 minutes post-delivery, however the NTNPs exhibited a significantly sharper decrease in EEA1-colocalization at 60 minutes than the $F3_{wt}$NPs.[14] This was further accompanied by a significant, sharp increase in colocalization

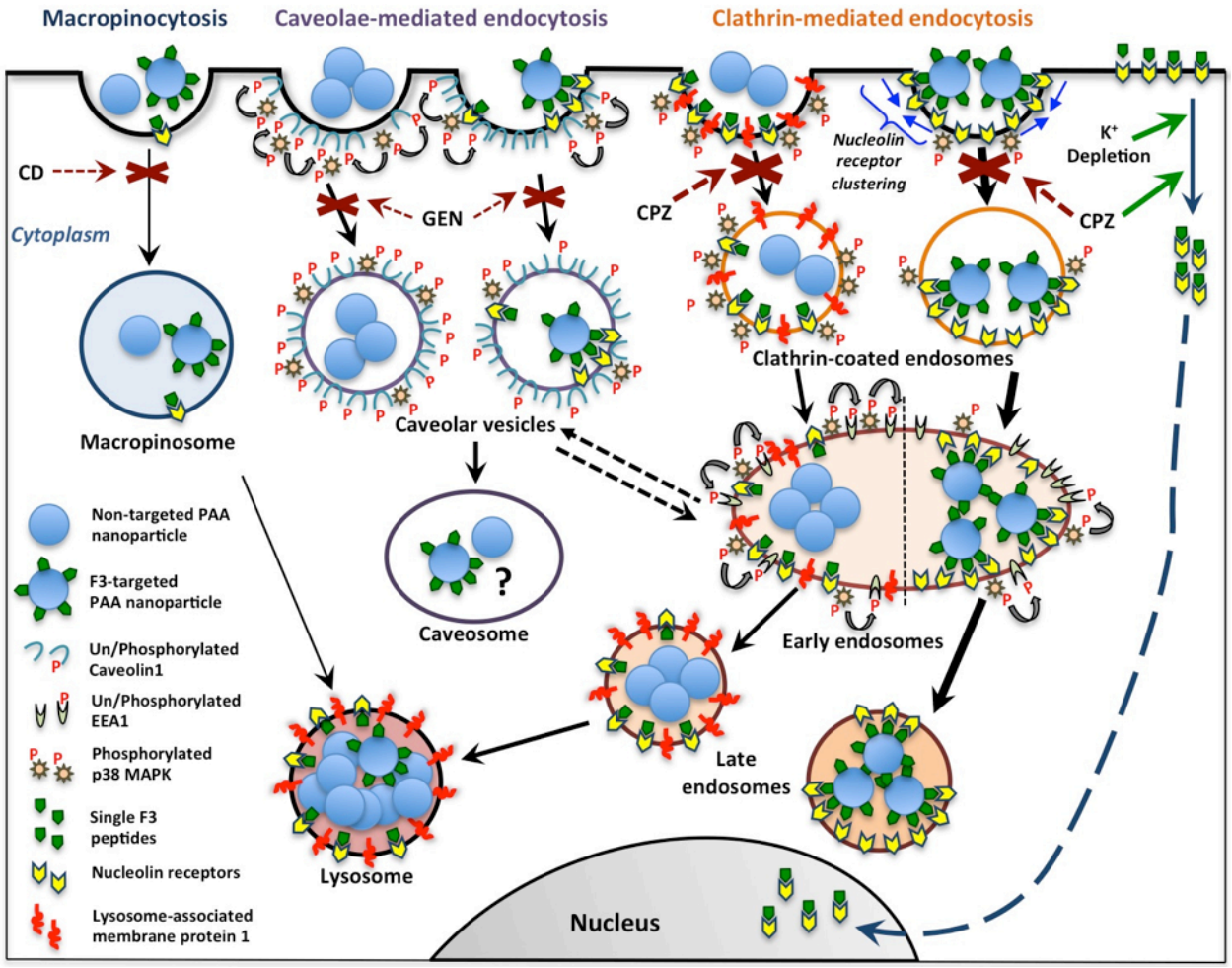

Fig. 4.4 Schematic summary of the endocytic pathways of internalization for $F3_{wt}$ peptide, non-targeted and $F3_{wt}$-targeted PAA nanoparticles (NTNPs and $F3_{wt}$NPs), and their activation of the p38 MAPK pathway in the nucleolin-overexpressing MDA-MB-435 cell line. The $F3_{wt}$NPs are predominantly internalized *via* the clathrin-mediated endocytic pathway, denoted by the potent inhibition of their internalization by Chlorpromazine (CPZ). The $F3_{wt}$NPs accumulated within vesicles devoid of LAMP1 protein (Lysosome-Associated Membrane Protein 1) in the perinuclear space. The caveolae-mediated and macropinocytosis endocytic pathways also contribute to the internalization of the $F3_{wt}$NPs, but to a lesser extent than the clathrin-mediated pathway. The clathrin-mediated and caveolae-mediated endocytic pathways contribute approximately equally to the internalization of the NTNPs, while macropinocytosis mediates their internalization to a lesser extent. Notably, the NTNPs co-internalize with LAMP-1 proteins from the cell surface following which they are trafficked to lysosomes, as denoted by the intense colocalization between the NTNPs and LAMP1 proteins (~50%) compared to the significantly lower colocalization between the $F3_{wt}$NPs and LAMP1 (8%). Furthermore, the $F3_{wt}$ peptide, and NTNPs more potently activated the p38β and p38δ MAPK isoforms than the $F3_{wt}$NPs. Activated p38 MAPKs phosphorylate Early Endosomal Antigen1 (EEA1), located in early endosomes, at Thr-1392, which abrogates the ability of EEA1 to mediate homotypic fusion of early endosomes. Hence, the $F3_{wt}$ peptide-laden and NTNP-laden EEA1-postive, early endosomes rapidly mature into late endosomes and fuse with lysosomes (LAMP-1 positive). In contrast, the $F3_{wt}$NPs exhibited slower egress from the EEA1-positive early endosomes, and lower colocalization with LAMP1-positive lysosomes. In addition, the activated p38 MAPKs phosphorylate Caveolin-1 at Tyr-14, which promotes the scission of caveolae from the cell membrane, and their subsequent internalization. While both the NTNPs and $F3_{wt}$NPs exhibited peak p38 MAPK activation at 2 hours post-delivery, the greater activation of the p38 MAPKs elicited by the NTNPs correlates with the higher colocalization, and internalization of the NTNPs with Caveolin-1 at 2 hours post-delivery than the $F3_{wt}$NPs.

between the NTNPs and Lysosome-Associated Membrane Protein-1 (LAMP1) from ~20% at 30 minutes post-delivery, to ~45% colocalization at 60 minutes post-delivery, whereas the $F3_{wt}$NPs-LAMP1 colocalization levels remained fairly constant (~8%) at 30 and 60 minutes post-delivery.[14] This suggested that at 60 minutes post-delivery the NTNPs, but not the $F3_{wt}$NPs, were rapidly trafficked out of the EEA1-positive endosomes, and into the LAMP1-positive lysosomes. Hence, the intracellular trafficking profiles of the NTNPs and $F3_{wt}$NPs also correlate well with their p-p38α ELISA profiles in that, of the NTNPs and $F3_{wt}$NPs, only the NTNPs induced a significant increase in the p-p38α concentration, from the 30 minute to 60 minute treatment time points (Fig. 4.2a). Although we did not perform time-dependent phosphorylation response assays for the p38β and p38δ isoforms, it is reasonable to deduce that these isoforms follow a similar phosphorylation trend to that of the p38α isoform. It has been established that activated p38 MAPKs can be recruited to early endosomes, and subsequently suppress the ability of EEA1 to catalyze homotypic fusion of early endosomes via phosphorylation of its Thr-1392 residue. We therefore present compelling evidence that the faster trafficking of the NTNPs out of the EEA1-positive early endosomes, with their concomitantly higher accumulation within the LAMP1-positive lysosomes, in MDA-MB-435 cells, can be attributed to the greater stimulation of p38 MAPK phosphorylation by the NTNPs than the $F3_{wt}$NPs.

Also, as previously reported by our group, the NTNPs and $F3_{wt}$NPs both reached peak colocalization with Caveolin-1 at 2 hours post-delivery, followed by subsequent decreases in colocalization for both types of PAA-NPs, at 3 hours post-delivery, and onward.[14] However, only at 2 hours and 3 hours post-delivery did we observe that the degree of NTNP-Caveolin-1 colocalization ($28.47 \pm 9.43^{(2hr)}$ and $21.95 \pm 4.97^{(3hr)}$) was significantly higher than the degree of $F3_{wt}$NP-Caveolin-1 colocalization ($14.50 \pm 3.94^{(2hr)}$ and $8.25 \pm 2.93^{(3hr)}$). It has already been

established that the activated p38 MAPKs mediate Tyr-14-phosphorylation of Caveolin-1, a critical requirement for the internalization of caveolae from the cell surface (Fig. 4.1).[23,24] These trends in NTNP-Caveolin-1, and $F3_{wt}$NP-Caveolin-1 colocalization indeed correlate with the trends in p38 MAPK phosphorylation (activation) elicited by the NTNPs and $F3_{wt}$NPs, respectively (Figs. 4.2a and 4.3b), i.e., NTNP-Caveolin-1 colocalization was ~2-fold greater than $F3_{wt}$NP-Caveolin-1 colocalization at 2 hours post-delivery, and at the same time-point, the NTNPs induced ~2-fold greater phosphorylation levels of p38β and p38δ than the $F3_{wt}$NPs (Fig. 4.3b, Table 4.1). Hence, our p38 MAPK data provide a compelling signaling mechanism to support our prior observation that, despite both the NTNPs and $F3_{wt}$NPs reaching peak colocalization with Caveolin-1 only 2 hours after delivery to the MDA-MB-435 cells, the NTNPs exhibited ~2-fold higher colocalization with Caveolin-1 than the $F3_{wt}$NPs. We present a revised schematic diagram that integrates the internalization, and intracellular trafficking of the $F3_{wt}$ peptide, NTNPs and $F3_{wt}$NPs of our previous study, with the cell signaling data presented in this study (Fig. 4.4).

Table 4.3 Summary of the fold changes in phosphorylation levels of the p38α, β, γ and δ isoforms, and phosphorylation levels of their downstream targets, the Heat Shock Protein (Hsp) 27 and tumor-suppressor protein p53, elicited by the various treatments relative to the untreated control

Phosphoprotein/ ***Phosphorylation sites detected***	**Untreated Control**	**$F3_{wt}$ Peptide**	**NTNPs**	**$F3_{wt}$NPs**	**$F3_{scram}$NPs**
p38α *(pT180/pY182)*	1.00	1.99	2.46	1.94	2.61
p38β *(pT180/pY182)*	1.00	2.29	3.01	1.53	1.79
p38δ *(pT180/pY182)*	1.00	2.96	3.27	1.53	1.81
p38γ *(pT183/pY185)*	1.00	1.03	1.03	1.03	1.01
p53 *(pS46)*	1.00	18.52	25.77	10.10	23.42
Hsp27 *(pS78/pS82)*	1.00	1.84	2.28	1.46	1.67

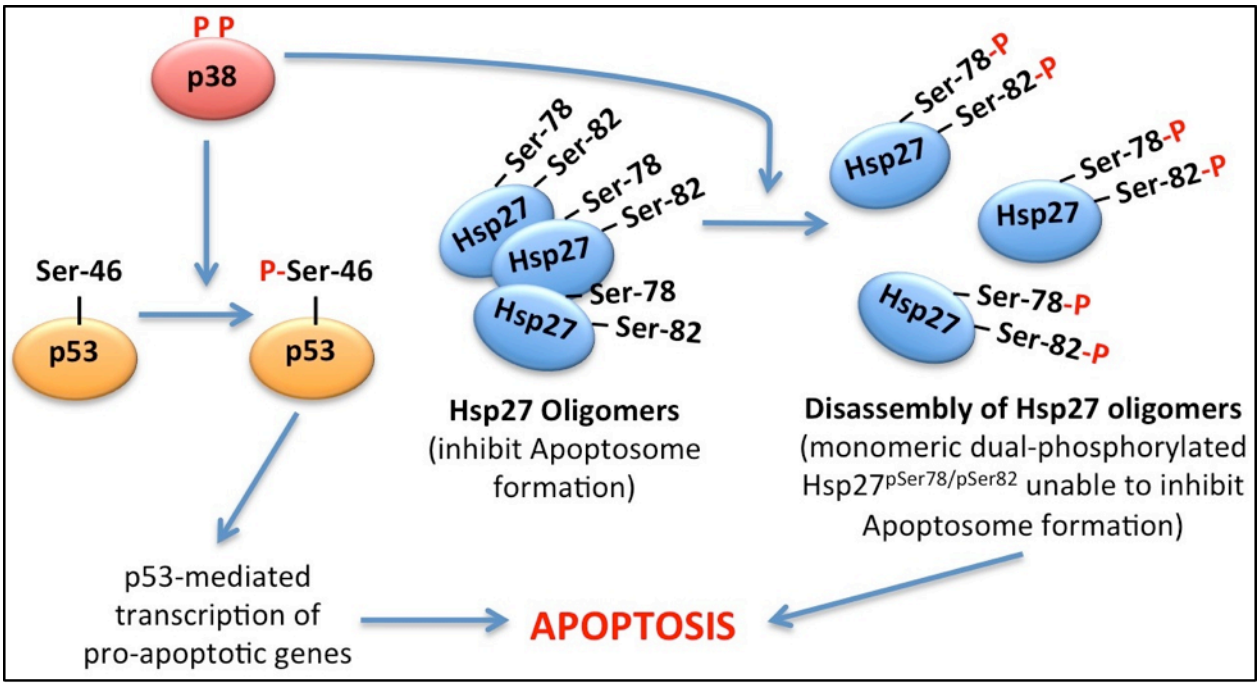

Fig. 4.5 Schematic diagram depicting the mechanisms by which activated p38 MAPKs promote apoptotic cell death by directly phosphorylating the p53 tumor suppressor, and Heat Shock Protein (Hsp) 27 proteins at specific Serine residues on the respective proteins.

The phosphorylation levels of two key target proteins of the p38 MAPKs, (i) tumor suppressor protein p53, phosphorylated at serine 46 ($p53^{pS46}$),[31] and (ii) Heat Shock Protein 27, phosphorylated at serine 78 and serine 82 ($Hsp27^{pS78/pS82}$),[32] were also assayed in the phosphoproteomic array (Fig. 4.3b, Table 4.3). Ser-46-phosphorylation of p53 promotes its transcription of several pro-apoptotic genes, which ultimately leads to apoptotic cell death (Fig. 4.5).[33] Hsp27, only when in its oligomeric high molecular weight state, inhibits apoptosis by interacting directly with cytochrome c, thus preventing formation of the apoptosome.[34] Ser-78/Ser-82-phosphorylation of Hsp27 promotes disassembly of Hsp27 oligomers, thus impairing its ability to prevent initiation of apoptosis (Fig. 4.5).[35] Hence, p38-mediated phosphorylation of both p53 and Hsp27 proteins, at their respective serine residues, shifts the cell toward a pro-apoptotic state (Fig. 4.5). Importantly, the trends in the enhancement of the phosphorylated p38β and p38δ levels were also reflected in the enhancement of the phosphorylated Hsp27

(Hsp27$^{pS78/pS82}$) levels (Fig. 4.3b, Table 4.3), i.e., the order of Hsp27$^{pS78/pS82}$ enhancement was: Untreated Control < $F3_{wt}$NPs < $F3_{scram}$NPs < $F3_{wt}$ peptide < NTNPs. The order of enhancement in the phosphorylated p53 (p53^{pS46}) levels was however slightly different: Untreated Control < $F3_{wt}$NPs < $F3_{wt}$ peptide < $F3_{scram}$NPs < NTNPs (Fig. 4.3b, Table 4.3). It is interesting to note that despite the absolute levels of p53^{pS46} being markedly lower than the absolute levels of Hsp27$^{pS78/pS82}$ across all treatments, the greatest fold-increases in phosphorylation levels, relative to the untreated control, were observed for p53 (Table 4.3). Nonetheless, it is evident that the higher enhancements in p-p38β and p-p38δ levels elicited by the $F3_{wt}$ peptide, NTNPs and $F3_{scram}$NPs, translated into higher Hsp27$^{pS78/pS82}$ and p53^{pS46} levels than those observed for the $F3_{wt}$NPs treatment.

4.2.2.2 Phosphoproteomic Arrays (JNK MAPK Pathway)

It is particularly interesting that the trend in enhancement of phosphorylated p-JNK1 (pT183/pY185) and p-JNK3 (pT221/pY223) levels were not only similar to each other, despite having different phosphorylation sites, but also similar to that of the p38β and p38δ isoforms (Fig. 4.3b, Appendix A4.3.2). The enhancement in p-JNK1/3 levels was as follows: Untreated control < $F3_{wt}$NPs < $F3_{scram}$NPs < $F3_{wt}$ peptide < NTNPs; albeit, only small differences in p-JNK1/3 levels between the $F3_{wt}$NPs and $F3_{scram}$NPs treatments, as well as between the $F3_{wt}$ peptide and NTNPs treatments were observed (Table 4.4). The phosphorylation profile for p-JNK2 (pT183/pY185), however, deviated from this trend; $F3_{wt}$ peptide induced the highest p-JNK2 level (1.89-fold), while the NTNPs and $F3_{wt}$NPs induced similar p-JNK2 levels (1.56- and 1.52-fold, respectively), while p-JNK2 remained at basal levels in the $F3_{scram}$NPs treatment (Fig.

Table 4.4 Summary of the fold changes in phosphorylation levels of the JNK1, JNK2, and JNK3 isoforms, elicited by the various treatments relative to the untreated control. The JNK pan represents the average phosphorylation level of the JNK1, 2, and 3 isoforms collectively.

Phosphoprotein/ ***Phosphorylation sites detected***	**Untreated Control**	**$F3_{wt}$ Peptide**	**NTNPs**	**$F3_{wt}$NPs**	**$F3_{scram}$NPs**
JNK1 *(pT183/pY185)*	1.00	3.91	4.23	2.39	2.90
JNK2 *(pT183/pY185)*	1.00	1.89	1.56	1.52	1.03
JNK3 *(pT221/pY223)*	1.00	3.44	3.84	1.87	2.43
JNK pan *(pT183/pY185/pT221/pY223)*	1.00	1.50	1.27	1.33	0.85

4.3b, Table 4.4). Although the absolute levels of p-JNK2 were markedly higher than the p-JNK1 and p-JNK3 levels in the corresponding treatments, the greatest enhancements were observed for p-JNK1 and p-JNK3 (Table 4.4, Appendix 4.3.2).

Nonetheless, the similarity between the p-p38β/δ and p-JNK1/3 phosphorylation profiles is not surprising since most stimuli that activate the p38 MAPKs typically also activate the JNK MAPKs. This is due to the p38 MAPKs and JNK MAPKs, along with their respective upstream MAP3K and MAP2K proteins, being assembled on common scaffold proteins, known as JNK-interacting proteins (JIP) (Fig. 4.9).[36] The MAP2K enzymes that directly phosphorylate the JNK1-3 MAPKs are the MKK4 and MKK7 phosphoproteins. Of the four characterized JIP scaffolds, JIP1, JIP2, JIP3 and JLP, the JIP1 and JIP2 bind only MKK7, the JLP binds only MKK4, while the JIP3 binds both MKK4 and MKK7. JLP binds only JNK1, while JIP1-3 bind all JNK MAPK isoforms. Furthermore, only JIP2 and JIP4 serve as scaffolds for assembling the p38 MAPKs, and their upstream MAP2K enzymes MKK3 (JIP1 and JLP) and MKK6 (JLP only). In addition, all JIPs can form homo-oligomers, while JIP2 can hetero-oligomerize with JIP1 and JIP3,[36] thus facilitating integration of extracellular signals into the p38 and JNK MAPK pathways. We were, however, unable to determine the phosphorylation levels of MKK4 and

MKK7, due to the exclusion of the phospho-specific antibodies for these proteins from the phosphoproteomic arrays used in this study, which would otherwise have provided further insight into the phosphorylation profiles of the JNK1-3 MAPKs. In addition, the tumor suppressor protein p53 is also a direct target of the JNK MAPKs. However, the JNK MAPKs phosphorylate p53 at Thr-81 ($p53^{pT81}$),[37] as opposed to Ser-46, the residue phosphorylated by the p38 MAPKs. Thr-81 phosphorylation stabilizes p53, thereby promoting its transcriptional activities, and ability to induce apoptosis.[37] Thus, Ser-46 and Thr-81 phosphorylation of p53 by the p38 and JNK MAPKs, respectively, act cooperatively in stabilizing p53, and promoting its transcriptional activity to induce apoptotic cell death. Although we were unable to determine the levels of $p53^{pT81}$ in this phosphoproteomic array, it is reasonable to postulate that the trend in enhancement of $p53^{pT81}$ levels would be similar to that of $p53^{pS46}$, given the strong similarity between the p-p38β/δ and p-JNK1/3 enhancement profiles.

4.2.2.3 Phosphoproteomic Arrays (ERK MAPK Pathway)

In contrast to the p38 and JNK MAPK pathways, the ERK MAPK pathway promotes cell survival and proliferation. The basal phosphorylated p-ERK2 (pT185/pY187) levels were ~24-fold greater than basal phosphorylated p-ERK1 (pT202/pY204) levels (Fig. 4.3a). However, the p-ERK2 levels essentially remained unchanged even after MDA-MB-435 cells were subjected to the various treatments (Fig. 4.3a, Table 4.5, Appendix A4.3.2), whereas the p-ERK1 levels elicited by the various treatments were significantly different from each other, and the untreated control (Fig. 4.3b, Table 4.5, Appendix A4.3.2). Most notably, the NTNPs and $F3_{scram}$NPs treatments both down-regulated p-ERK1 levels relative to the untreated control (0.80-fold and

Table 4.5 Summary of the fold changes in phosphorylation levels of the ERK1 and ERK2 MAPK phosphoproteins, and phosphorylation levels of their downstream targets, MSK2, RSK1, RSK2 and CREB, elicited by the various treatments relative to the untreated control.

Phosphoprotein/ ***Phosphorylation sites detected***	**Untreated Control**	**$F3_{wt}$ Peptide**	**NTNPs**	**$F3_{wt}$NPs**	**$F3_{scram}$NPs**
ERK1 *(pT202/pY204)*	1.00	1.92	0.80	1.68	0.44
ERK2 *(pT185/pY187)*	1.00	1.00	1.00	1.00	1.01
MSK2 *(pS360)*	1.00	2.22	2.24	1.61	1.20
RSK1 *(pS380)*	1.00	1.11	1.09	1.09	1.07
RSK2 *(pS386)*	1.00	2.52	2.97	1.72	1.57
CREB *(pS133)*	1.00	0.93	0.86	1.00	0.65

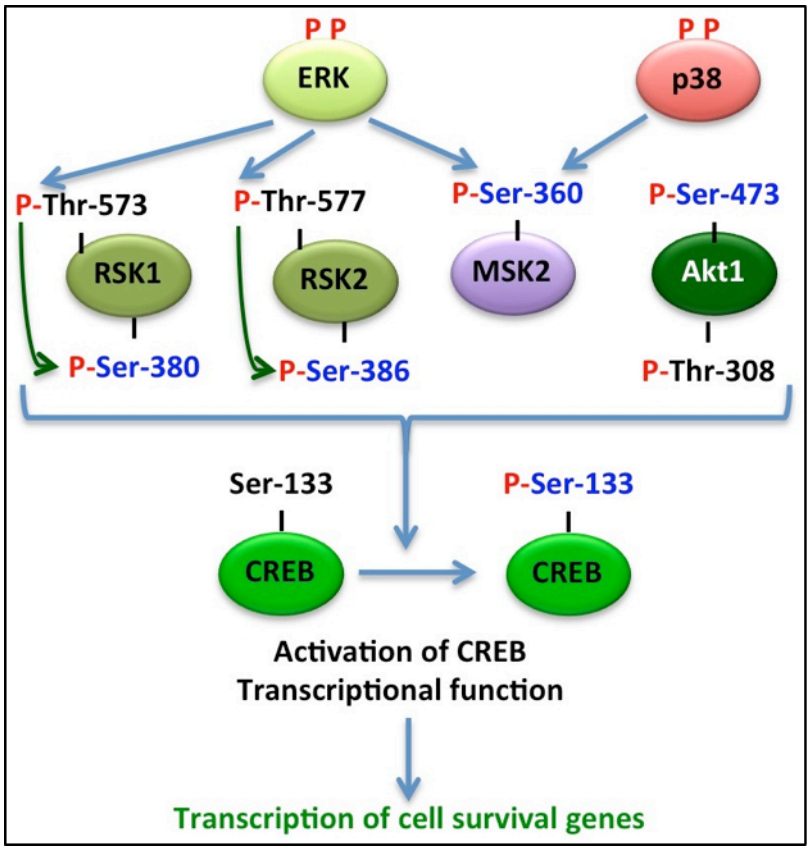

Fig. 4.6 Schematic diagram depicting the mechanism by which phosphorylated (activated) ERK MAPKs promote cell survival through direct phosphorylation of the RSK1, RSK2 and MSK2 proteins, which in turn phosphorylate and activate the transcriptional activator protein, CREB, at its Ser-133 residue. ERK1/2 directly phosphorylate and activate RSK1 and RSK2 at Thr-573 and Thr-577, respectively, located in the activation loops of their C-terminal kinase domains. The phosphorylated C-terminal kinase domains of RSK1 and RSK2 in turn auto-phosphorylate their hydrophobic motifs at Ser-380 and Ser-386, respectively. Phosphorylated residues detected on the various phosphoproteins in this study are highlighted in blue text.

0.40-fold, respectively), while the $F3_{wt}$ peptide and $F3_{wt}$NPs up-regulated p-ERK1 levels relative to the untreated control (1.92-fold and 1.68-fold, respectively) (Fig. 4.3b, Table 4.5, Appendix A4.3.2). The phosphorylation status of the ERK1/2-target proteins, MSK2 (mitogen- and stress-activated kinase 2), RSK 1 and RSK2 (p90 ribosomal S6 kinases 1 and 2), and the further downstream target CREB (cAMP response element-binding protein) were also determined in this phosphoproteomic array (Fig. 4.6). MSK2 is potently activated *in vivo* by ERK1/2 and p38, but not by JNK1-3, by direct phosphorylation of Ser-360 located in its turn motif,[38] which was detected in this assay (Fig. 4.6). Both the $F3_{wt}$ peptide and NTNPs elicited essentially similar enhancements in Ser-360-phosphorylated MSK2 ($MSK2^{pS360}$) (2.22-fold and 2.24-fold respectively), followed by the $F3_{wt}$NPs (1.61-fold) and $F3_{scram}$NPs (1.20-fold) (Fig. 4.3b, Table 4.5, Appendix 4.3.2).

RSK1 and RSK2, however, are activated only by ERK1/2 by direct phosphorylation of their Thr-573 and Thr-577 residues, respectively (located in the activation loop of their C-terminal kinase domains), which in turn auto-phosphorylate their hydrophobic motifs at Ser-380 and Ser-386, respectively (Fig. 4.6).[39,40] Only the Ser380- and Ser386-phosphorylated sites of RSK1 and RSK2, respectively, were detected in this phosphoproteomic array (Fig. 4.6). All treatments enhanced the levels of Ser-380-phosphorylated RSK1 ($RSK1^{pS380}$), however there were only marginal differences in the $RSK1^{pS380}$ levels between the different treatments (Fig. 4.3b, Table 4.5, Appendix A4.3.2). Although basal $RSK1^{pS380}$ levels were ~8-fold higher than Ser-386-phosphorylated RSK2 ($RSK2^{pS386}$) levels, there were distinct differences in the $RSK2^{pS386}$ levels between the different treatments (Fig. 4.3b, Table 4.5, Appendix A4.3.2). Surprisingly, the NTNPs, which down-regulated pERK1 levels (0.80-fold relative to untreated control), induced the highest $RSK2^{pS386}$ levels of all the treatments (2.97-fold), followed by the $F3_{wt}$ peptide (2.52-

fold), the $F3_{wt}$NPs (1.72-fold) and $F3_{scram}$NPs (1.57-fold). It is important to note however, that additional sites in the activation loop and N-terminal kinase domains of RSK1 and RSK2 also require phosphorylation for these kinases to achieve full activation.[41,42] Hence, the $RSK1^{pS380}$ and $RSK2^{pS386}$ phosphorylation levels alone are insufficient to accurately assess the activation status of RSK1 and RSK2, and require in-depth investigation.

The phosphorylation of CREB at Ser-133 ($CREB^{pS133}$) is crucial for its activation, and is facilitated by multiple kinases, including MSK1/2,[38,43] RSK2,[44] and Akt (Fig. 4.6).[45] Briefly, CREB is an important DNA-binding protein transcription factor, which upon activation up-regulates the expression of a broad range of cellular survival genes.[46] Remarkably, the $CREB^{pS133}$ level in $F3_{wt}$NPs-treated cells remained at basal level, whereas the $F3_{wt}$ peptide, NTNPs, and $F3_{scram}$NPs treatments progressively down-regulated $CREB^{pS133}$ levels relative to the untreated control (0.93-fold, 0.86-fold and 0.65-fold, respectively) (Fig. 4.2b, Table 4.5, Appendix A4.3.2). This observation suggests that the $F3_{wt}$ peptide, NTNPs, and $F3_{scram}$NPs treatments, but not the $F3_{wt}$NPs, promote dephosphorylation of CREB at Ser-133. This is particularly interesting considering that both the $F3_{wt}$ peptide and NTNPs treatments induced higher $MSK2^{pS360}$ and $RSK2^{pS386}$ levels than the $F3_{wt}$NPs. However, it has been shown that CREB is potently dephosphorylated by the phosphatase enzyme Protein Ser/Thr Phosphatase Type 2A (PP2A),[47] which is typically activated between 0.5 to 1 hour after initiation of an apoptotic stress, and remains active for several hours therafter.[48] Given that PP2A is activated by the p38 MAPKs, with the $F3_{wt}$ peptide, NTNPs and $F3_{scram}$NPs being the most potent activators of p38β and p38δ (Fig. 4.3b, Table 4.1, Appendix 4.3.2), and that our phospho-proteomic experiment was performed on 2-hour post-treatment cell lysates, it is therefore likely that these treatments antagonize the activation of CREB via p38-mediated activation of the PP2A enzyme.

4.2.2.4 Phosphoproteomic Arrays (Akt Pathway)

The Akt pathway is an important signal transduction pathway that regulates cellular functions including cell growth, nutrient metabolism, transcriptional regulation and cell survival.[49] Three Akt isoforms, Akt1, Akt2, and Akt3, mediate signaling through this pathway, and require dual phosphorylation of their Thr-308/Ser-473 (Akt1), Thr-309/Ser-474 (Akt2), and Thr-305/Ser-472 (Akt3) residues respectively, to achieve full activation.[50] The phospho-specific antibodies employed in this array, however, detected only the Ser-473-, Ser-474- and Ser-472-phosphorylated forms of Akt1, Akt2 and Akt3, respectively (Fig. 4.7). Nonetheless, based on the limited data on the activation status of the Akt isoforms ($Akt1^{pS473}$, $Akt2^{pS474}$ and $Akt3^{pS472}$), $Akt3^{pS472}$ had the lowest basal level of phosphorylation, but was the only Akt isoform that exhibited markedly varying degrees of phosphorylation enhancement in response to the different treatments (Figs. 4.3a and 4.3b, Table 4.6, Appendix 4.3.2). The $F3_{wt}$ peptide elicited a 1.97-fold enhancement of $Akt3^{pS472}$ levels relative to the untreated control, followed by the NTNPs (1.90-fold), $F3_{wt}$NPs (1.61-fold) and $F3_{scram}$NPs (1.41-fold), however the difference between the $F3_{wt}$ peptide and NTNPs treatments, as well as between the $F3_{wt}$NPs and $F3_{scram}$NPs treatments were not significant (Fig. 4.3b, Table 4.6, Appendix 4.3.2).

The downstream targets directly phosphorylated by the activated Akt isoforms include, GSK-3α and GSK-3β (glycogen synthase kinase-3α/β),[51] TOR (target of rapamycin),[52] and CREB.[45] Briefly, GSK-3α and GSK-3β are responsible for regulating a broad range of cellular processes including, glycogen and protein metabolism, cell cycle regulation and proliferation. Akt-mediated phosphorylation of GSK-3α at Ser-21, and GSK-3β at Ser-9 (as detected in this phosphoproteomic array) inhibits both isoforms.[51] Furthermore, p70 ribosomal S6 kinase (p70S6k)- and RSK2-mediated phosphorylation of GSK-3α and GSK-3β at Ser-21 and Ser-9,

Table 4.6 Summary of the fold changes in phosphorylation levels of the Akt1, Akt2 and Akt3 isoforms, and phosphorylation levels of their downstream targets, Glycogen synthase kinase-3α/β, TOR and p70S6 Kinase, elicited by the various treatments relative to the untreated control. The Akt pan represents the average phosphorylation level of the Akt1, 2 and 3 isoforms, collectively.

Phosphoprotein/ ***Phosphorylation sites detected***	**Untreated Control**	**$F3_{wt}$ Peptide**	**NTNPs**	**$F3_{wt}$NPs**	**$F3_{scram}$NPs**
Akt1 *(pS473)*	1.00	1.01	1.00	1.01	0.98
Akt2 *(pS474)*	1.00	1.04	1.03	1.04	1.03
Akt3 *(pS472)*	1.00	1.97	1.90	1.61	1.41
Akt pan *(pS473/pS474/pS472)*	1.00	1.03	1.02	1.03	0.88
GSK-3α/β *(pS21/pS9)*	1.00	1.02	0.97	1.01	1.03
GSK-3β *(pS9)*	1.00	1.01	0.98	0.99	0.99
TOR *(pS2448)*	1.00	1.65	2.09	1.21	1.00
p70S6k *(pT421/pS424)*	1.00	1.59	1.27	1.53	0.94

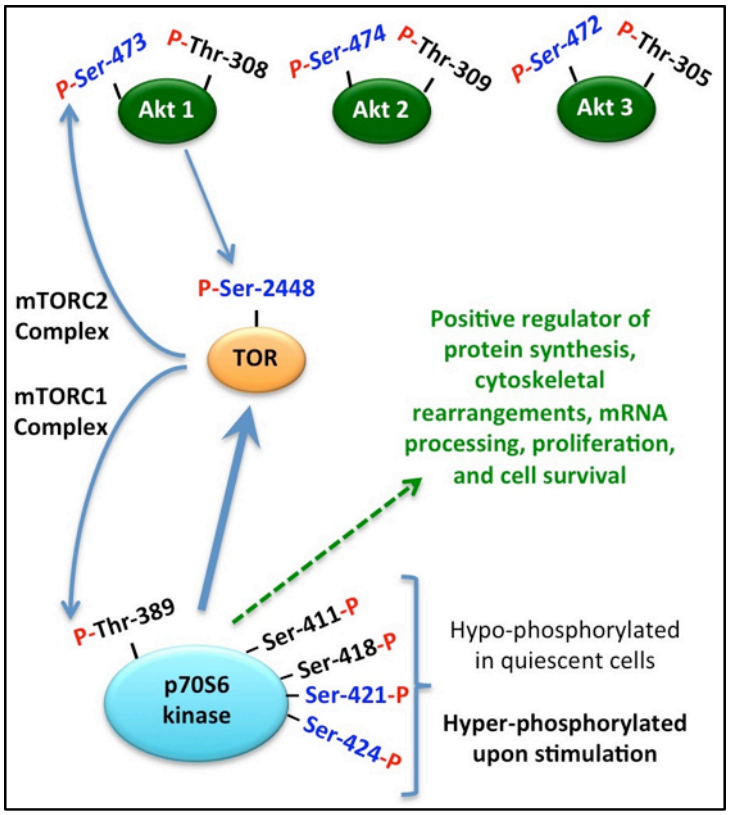

Fig. 4.7 Schematic diagram depicting the feedback phosphorylation relationship between Akt1, TOR and p70S6 kinase phosphoproteins. The p70S6 kinase is predominantly responsible for phosphorylating TOR at its Ser-2448 residue. Ser-2448-phosphorylated TOR is, in turn, incorporated within the mTORC1 and mTORC2 multi-protein complexes. mTORC1 subsequently phosphorylates p70S6 kinase at Thr-389, which, however, was not detected in the phosphoproteomic assay employed in this study. mTORC2 further phosphorylates Akt1 at its Ser-473 residue. Phosphorylated residues detected on the various phosphoproteins in this study are highlighted in blue text.

respectively, also inhibits both GSK-3 isoforms.[53,54] However, neither treatment elicited significant changes in the phosphorylated levels of either GSK-3 isoform, compared to their respective basal phosphorylated levels in the untreated control (Fig. 4.3a, Table 4.6, Appendix A4.3.2).

TOR is a highly conserved protein kinase that functions as a central coordinator of cell growth, by positively and negatively regulating several anabolic and catabolic processes, respectively. The p70S6k, and to a lesser extent Akt, directly phosphorylates TOR at Ser-2448 (TOR^{pS2448}; as detected in this phosphoproteomic array), which lies within its C-terminal regulatory region (Fig. 4.7).[52,55,56,57] Furthermore, TOR^{pS2448} is found in both the functional multi-protein complexes mTORC1 and mTORC2,[58] which in turn phosphorylate and activate p70S6k (at Thr-389), and Akt1 (at Ser-473), respectively. However, even though TOR^{pS2448} is found in both the mTORC1 and mTORC2 complexes, the level of Ser-2448-phosphorylated TOR was found to correlate only with the mTORC1 activity, and not with the mTORC2 activity.[58] That is, despite Akt1 being directly phosphorylated at Ser-473 by mTORC2, the level of TOR^{pS2448} did not correlate directly with the levels of $Akt1^{pS473}$ as a direct measure of mTORC2 activity. The NTNPs elicited the greatest enhancement in TOR^{pS2448} levels (2.09-fold), relative to the untreated control, followed by the $F3_{wt}$ peptide (1.65-fold), and the $F3_{wt}$NPs (1.21-fold), while the $F3_{scram}$NPs treatment elicited no change from the basal TOR^{pS2448} level of the untreated control (Fig. 4.3b, Table 4.6, Appendix 4.3.2). The various treatments however, did not elicit a similar trend in the levels of $Akt1^{pS473}$ to that of TOR^{pS2448}. Hence, our observations are in agreement with the findings of Rosner *et al.,*[58] that the levels of $Akt1^{pS473}$ do not correlate directly with the levels of TOR^{pS2448}.

In addition to phosphorylation at Thr-389, p70S6k is also phosphorylated at residues Ser-411, Ser-418, Ser-421 and Ser-424, which are located in the auto-inhibitory domain of Module IV in p70S6k (Fig. 4.7).[59] These residues are hypo-phosphorylated in quiescent cells, and become hyper-phosphorylated upon serum-induced activation. Of the above-mentioned residues, the phospho-specific antibody, used in this phospho-proteomic array, detected the phosphorylated forms of only the Ser-421 and Ser-424 residues of p70S6k (Fig. 4.7), thus providing only a limited view into the activation status of p70S6k. Also, the absence of data on the Thr-389-phosphorylation levels of p70S6k, which would be a direct indicator of mTORC1 activity, precludes us from making direct correlations with the levels of TOR^{pS2448}, since it is one of the functional components in the mTORC1 complex. Nonetheless, the $F3_{wt}$ peptide and $F3_{wt}$NPs elicited the highest enhancement in the $p70S6k^{pS421/424}$ levels (1.59-fold and 1.53-fold, respectively), relative to the untreated control, followed by the NTNPs (1.27-fold); on the other hand, the $F3_{scram}$NPs elicited a slight, but not significant, down-regulation in $p70S6k^{pS421/424}$ levels (0.94-fold) (Fig. 4.3b, Table 4.6, Appendix A4.3.2). Given that p70S6k is a positive regulator of protein synthesis, cytoskeletal rearrangements, mRNA processing, proliferation, and of cell survival,[60] these data suggest that the $F3_{wt}$ peptide and $F3_{wt}$NPs are more supportive of cellular proliferation than the NTNPs, and the $F3_{scram}$NPs.

4.2.2.5 p-ERK/p-p38 MAPK Signaling Profiles and Implications for Cell Survival

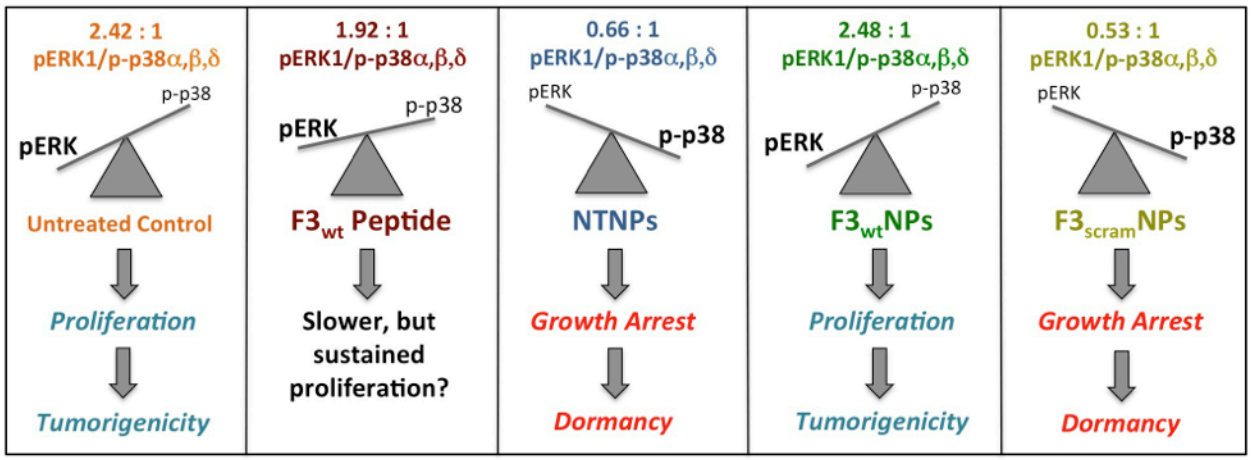

Fig. 4.8 Schematic diagram depicting the effects of the $F3_{wt}$ peptide, NTNPs, $F3_{wt}$NPs and $F3_{scram}$NPs treatments on the ratio of phosphorylated ERK1 (pERK1) to average phosphorylated p38 (p-p38α, β and δ isoforms) MAPKs in MDA-MB-435 cells. MDA-MB-435 cells, proliferating under standard cell culture conditions, exhibited a basal pERK/p-p38 ratio of 2.42: 1. Of the various treatments, the $F3_{wt}$NPs elicited the highest pERK/p-p38 ratio, which was marginally higher than that of the untreated control MDA-MD-435 cells, followed by $F3_{wt}$ peptide (1.92 : 1), NTNPs (0.66 : 1), and $F3_{scram}$NPs (0.53 : 1).

It is now known that the activation of the p38 and JNK MAPK pathways, with concurrent inhibition of the ERK MAPK pathway, is necessary for cells to undergo apoptosis.[61] Moreover, it has been shown that a *high p-ERK/p-p38 ratio* in tumor cells favors proliferation, whereas a *low p-ERK/p-p38 ratio* favors dormancy.[62,63] Given that ERK1, and p38α, p38β and p38δ were the only isoforms of their respective MAPK pathways that were phosphorylated to varying degrees in response to the different treatments in this study, we determined the ratio of p-ERK1 to average p-p38(α, β and δ) for each treatment and the untreated control (Fig. 4.8). The resultant p-ERK1/p-p38 ratios suggest that the $F3_{wt}$NPs, and to a lesser extent the $F3_{wt}$ peptide, promote cellular proliferation, whereas the NTNPs and $F3_{scram}$NPs promote growth arrest. Further support for this hypothesis lies in the observations that the NTNPs, and $F3_{scram}$NPs treatments elicited higher phosphorylated levels of the pro-apoptotic $Hsp27^{pS78/pS82}$ and $p53^{pS46}$ proteins, but lower phosphorylated levels of the pro-survival $CREB^{pS133}$ and $p70S6k^{pS421/424}$ proteins, than the $F3_{wt}$NPs treatment (Fig. 4.3b, Tables 4.3, 4.5, 4.6, Appendix A4.3.2). Interestingly, the $F3_{wt}$

peptide treatment elicited intermediate levels of phosphorylated Hsp27$^{pS78/pS82}$ and p53^{pS46} proteins (higher than in the F3$_{wt}$NPs treatment, but lower than in the NTNPs treatment), but higher phosphorylated levels of the CREB^{pS133} and p70S6k$^{pS421/424}$ proteins than the NTNPs treatment (Fig. 4.3b, Tables 4.3, 4.5, 4.6, Appendix A4.3.2). Considering these data together with the p-ERK1/p-p38 ratio of 1.92: 1 elicited by the F3$_{wt}$ peptide treatment, the cells treated with F3$_{wt}$ peptide may therefore still proliferate, albeit at a slower rate than the untreated control cells, and the F3$_{wt}$NPs-treated cells. *Table 4.7 summarizes the physicochemical properties of the various peptides, and nanoparticles, as well as the pertinent signaling profiles elicited by each.*

Table 4.7 Summary of the physicochemical properties of the F3$_{wt}$ peptide, F3$_{scram}$ peptide, NTNPs, F3$_{wt}$NPs and F3$_{scram}$NPs, and the pertinent signaling profiles elicited by each. ND: not determined

Physicochemical Properties	**F3$_{wt}$ Peptide**	**F3$_{scram}$ Peptide**	**NTNPs**	**F3$_{wt}$NPs**	**F3$_{scram}$NPs**
Hydrodynamic diameter (nm)	-	-	52.5 nm	53.0 nm	52.2 nm
Peptide charge/ Zeta Potential (mV)	+9	+9	+20.56 mV	+25.89 mV	+25.74 mV
Surface PEGylation	No	No	No	Yes	Yes
Valency/ *Receptor Specificity*	Monovalent/ *Nucleolin*	Monovalent/ *Scavenger Receptors?*	No surface conjugated peptides/ *LRP-1?*	Multivalent/ *Nucleolin*	Multivalent/ *Scavenger Receptors?*
p-ERK1/p-p38α,β,δ MAPK Signaling Ratio ***(Proliferative ratio highlighted in green; Pro-apoptotic ratio highlighted in red)***					
p-ERK1/p-p38α,β,δ	**1.92: 1**	ND	**0.66: 1**	**2.48: 1**	**0.53: 1**
Fold changes in phosphorylation levels of anti-apoptotic phosphoproteins (relative to untreated control) ***(Proliferative changes highlighted in green; Pro-apoptotic changes highlighted in red)***					
CREB *(pS133)*	**0.93-fold**	ND	**0.86-fold**	**1.00-fold**	**0.65-fold**
p70S6k *(pT421/pS424)*	**1.59-fold**	ND	**1.27-fold**	**1.53-fold**	**0.94-fold**
Fold changes in phosphorylation levels of pro-apoptotic phosphoproteins (relative to untreated control) ***(Proliferative changes highlighted in green; Pro-apoptotic changes highlighted in red)***					
p53 *(pS46)*	**18.52-fold**	ND	**25.77-fold**	**10.10-fold**	**23.42-fold**
Hsp27 *(pS78/pS82)*	**1.84-fold**	ND	**2.28-fold**	**1.46-fold**	**1.67-fold**

4.2.2.6 Proposed Cell Surface Receptor-NP Interactions

Since each of these treatments elicited different p-ERK1/p-p38 ratios, the question remains as to what the underlying mechanism(s) are by which these different MAPK signaling profiles are elicited. First, the *low p-ERK1/p-p38 ratio* (0.66: 1) elicited by the NTNPs suggests that they bind to a cell surface receptor which favors signaling predominantly via the p38 MAPK pathway. One such cell surface receptor is LRP-1 (low-density lipoprotein receptor-related protein-1), which is a large, transmembrane scavenger receptor that recognizes and mediates the internalization of 51 known structurally distinct biological macromolecules from the extracellular environment.[64] LRP-1 is also inextricably involved in cell signaling via association of its cytoplasmic domain with the scaffold proteins JIP1 and JIP2 (JNK-associated interacting proteins), and the adapater protein Shc.[64] As mentioned earlier, JIP2 provides scaffolding functions for the assembly of both p38 and JNK signaling modules, while JIP1 exclusively promotes the assembly of JNK modules.[36] Shc interacts with Grb2 and Sos to activate Ras, ultimately leading to the activation of the ERK1/2 MAPKs. However, strong activation of the p38 and JNK pathways rapidly promote down-regulation of the ERK pathway, as observed with the NTNPs. This is achieved by p38-mediated activation of the phosphatase (dephosphorylating) enzyme PP2A,[65] typically between 0.5 and 1 hour after stimulation, and JNK-mediated expression of the dual-specificity phosphatases, MKP-1 and MKP-2,[66] typically between 1 and 3 hours after stimulation.[48] PP2A has been shown to bind directly to, and inhibit the phosphorylation of Shc, thereby inhibiting activation of Ras, and signaling further downstream to ERK1/2 [67] (Fig. 4.9). Furthermore, PP2A can also directly dephosphorylate, and inactivate both MEK1/2 and ERK1/2; MEK1/2 being the upstream MAP2Ks that directly phosphorylate ERK1/2 when activated[68,69] (Fig. 4.9). The phosphatases MKP-1 and MKP-2 activated by JNK

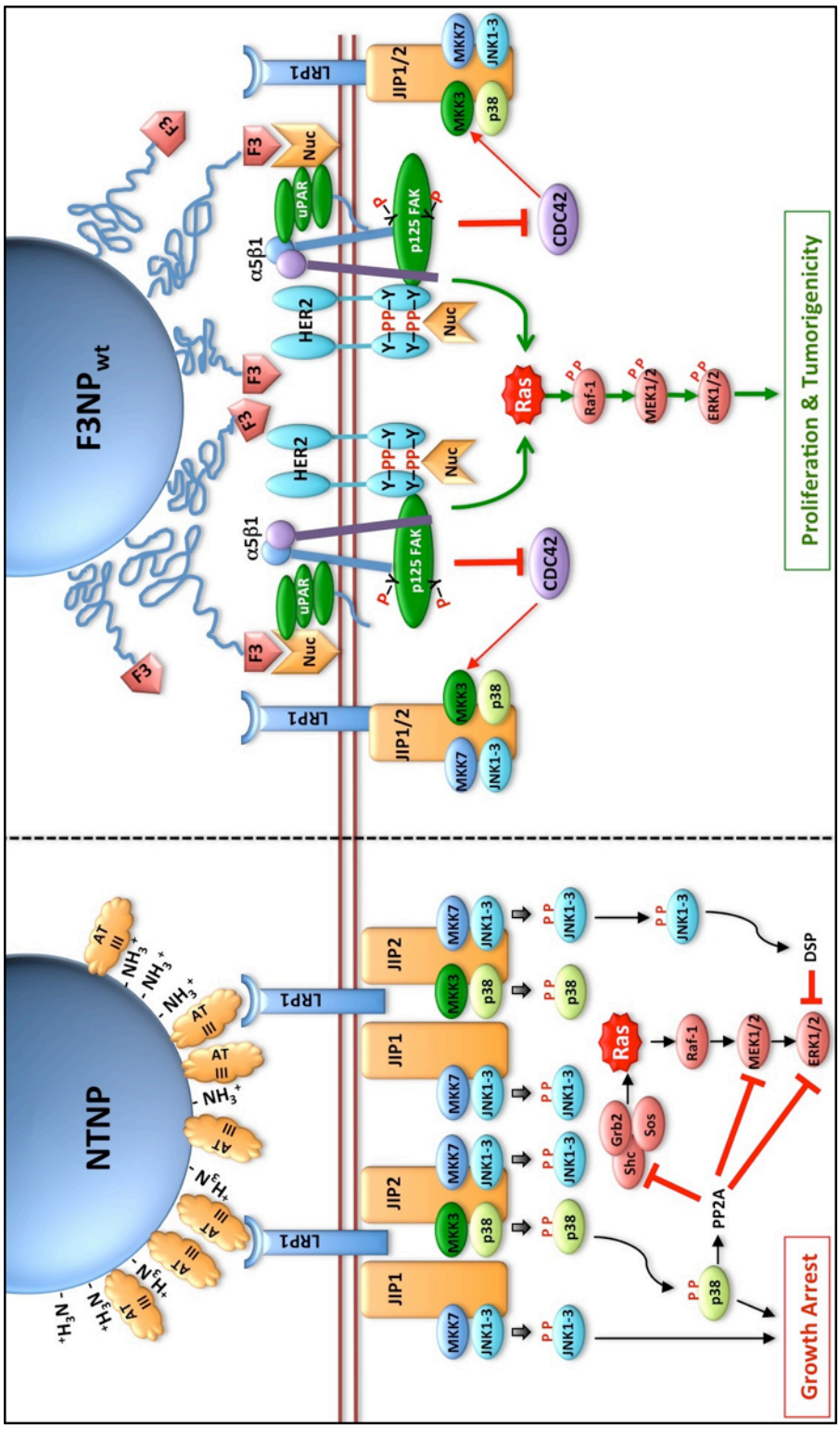

Fig. 4.9 Proposed receptor complex interactions of the NTNPs and F3$_{wt}$NPs at the cell surface of MDA-MD-435 cells as plausible mechanisms by which the NTNPs elicit a *low p-ERK/high p-p38 ratio*, and the F3$_{wt}$NPs elicit a *high p-ERK/low p-p38 ratio*. α5β1 (α5β1 Integrin receptors), AT III (Antithrombin III), DSP (Dual-specificity Phosphatase), p125 FAK (Focal Adhesion Kinase), JIP1/2 (JNK Interacting Protein 1/2), LRP1 (Low-density Lipoprotein-related Receptor 1), Nuc (Nucleolin), PP2A (Protein Phosphatase 2A), uPAR (Urokinase Plasminogen Activator Receptor).

in turn directly dephosphorylate ERK1/2 [66] (Fig. 4.9). It is important to note that all treatments in this study were performed for a duration of 2 hours. Thus, at this time point, the *low p-ERK1/p-p38 ratio* in the NTNP treatment is indicative of induced PP2A, MKP-1 and MKP-2 phosphatase enzyme activites. Although the NTNPs employed in this study were devoid of surface functionlizations, they would acquire a corona of surface-adsorbed serum proteins upon delivery into the cell culture medium, as has been shown with other acrylamide-based NPs.[70,71] Antithrombin III, a protein component of fetal bovine serum,[72] and a ligand also recognized by LRP-1,[64] is a likely serum protein constitutent of the protein corona that would form around the NTNPs, and thus mediate the binding of the NTNPs specifically to LRP-1 (Fig. 4.9).

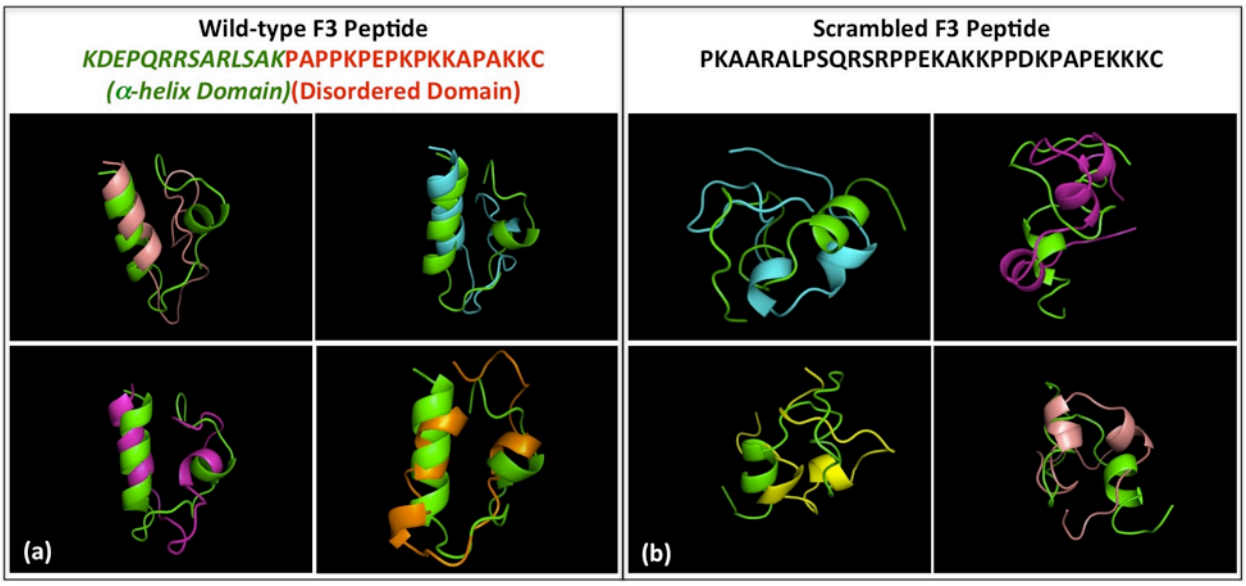

Fig. 4.10 Simulated secondary structures of the wild-type (a) and scrambled (b) F3 peptides. Five different structural simulations for each peptide were generated via the PEP-FOLD peptide structure prediction server (http://bioserv.rpbs.univ-paris-diderot.fr/services/PEP-FOLD/) and compared. In each set of comparisons, the green peptide structure was kept constant against which the other four structures were compared.

Second, the *low p-ERK1/p-p38 ratio* (0.53: 1) elicited by the $F3_{scram}$NPs is interesting in that, although they were not as effective as the NTNPs in inducing phosphorylation of the p38β/δ and JNK1-3 MAPKs, the $F3_{scram}$NPs were more effective at suppressing the p-ERK1 levels. Based on our stuctural simulations of the F3-wild type and F3-scrambled peptide sequences, we

observed that the N-terminal half of the F3-wild type peptide folds into a stable α-helix, whereas this property is completely absent in the F3-scrambled peptide, which adopts a range of misfolded states (Figs. 4.10a,b). As such, the misfolded states and incorrect sequence of amino acids of the F3-scrambled peptide would abrogate its ability to recognize and bind specifically to the cell surface Nucleolin receptors, however internalization of the $F3_{scram}$NPs may occur via scavenger receptors, such as gp18 and gp30. Consistent with this theory, Fleischer and Payne recently demonstrated that a loss of α-helicity in the secondary structure of albumin proteins, upon binding to cationic polystyrene NPs, diverts their internalization via the albumin receptor to via the gp18 and gp30 scavenger receptors.[73] However, the signaling pathways associated with gp18 and gp30 are currently unknown, and this hypothesis remains to be tested.

The cell surface Nucleolin receptor, to which the $F3_{wt}$NPs specifically bind, lack both transmembrane and cytoplasmic domains. Therefore, the *high p-ERK1/p-p38 ratio* (2.48: 1) elicited by the $F3_{wt}$NPs suggests that cell surface Nucleolin receptors associate with transmembrane receptor complexes that favor signaling via the ERK pathway over p38/JNK pathways. A possible receptor complex is one comprised of the urokinase plasminogen activator receptor (uPAR), α5β1-integrin, and epidermal growth factor receptor (EGFR).[74,75] Briefly, when uPAR is expressed at high-levels, it frequently interacts with, and activates α5β1-integrin (the fibronectin receptor), which in turn associates with, and activates EGFR in a ligand-independent manner by promoting auto-phosphorylation of its intracellular domains. The assembly of the uPAR/α5β1-integrin/EGFR complex subsequently recruits focal adhesion kinase (FAK), from the cytoplasm to the intracellular domains of α5β1-integrin and EGFR, and undergoes phosphorylation. In combination with the phosphorylated intracellular domains of EGFR, activated FAK subsequently activates Ras, ultimately leading to activation of the ERK

pathway.[75,76] Furthermore, activated FAK also suppresses activation of p38 MAPKs by inactivating Cdc42[74] (Fig. 4.9). Cdc42 is a Rho GTP-binding protein that directly phosphorylates MLK1 (the MAP3K enzyme which promotes downstream activation of the p38 and JNK MAPK enzymes).[77] Briefly, FAK promotes deactivation of Cdc42 by converting it from its GTP-bound state (active) to its GDP-bound state (inactive) by recuritment of the GTPase activating protein (GAP) known as GRAF (GTPase regulator associated with FAK).[78] This hypothesis is supported by our observation that the $F3_{wt}$NPs elicited lower levels of phosphorylated MKK3 and MKK6 (the MAP2K enzymes that directly phosphorylate the p38α/β/γ/δ isoforms) than the $F3_{wt}$ peptide and NTNPs (Fig. 4.3b).

The involvement of Nucleolin in this signaling complex is two-fold. First, cell surface Nucleolin physically interacts, via its C-terminal glycine-arginine-rich domain (GAR domain, 646-707 aa) with uPAR,[79] while α5β1-integrin interacts with uPAR via the NLTY motif of α5[80] (Fig. 4.9). Second, the C-terminal 212 amino acids (the fourth RNA-binding domain (RBD) and GAR domain) of *cytoplasmically-localized Nucleolin* interacts with the cytoplasmic domain of EGFR, and the overexpression of both leads to EGFR phosphorylation, dimerization and enhanced cell proliferation.[81] In addition to inducing phosphorylation and dimerization of EFGR (or HER1/ ErB1) in a ligand-independent manner, Nucleolin has been shown to induce phosphorylation and dimerization of the structurally similar HER2 (ErbB2), HER3 (ErbB3), and HER4 (ErbB4) receptors by direct interaction with their cytoplasmic domains.[82] MDA-MB-435 cells specifically, overexpress HER2 receptors, instead of EGFR/HER1,[83] in addition to α5β1-integrin,[84] and cell surface Nucleolin,[85] but express uPAR at low levels.[86] Nonetheless, it is highly plausible that, in MDA-MB-435 cells, Nucleolin/uPAR/α5β1-integrin/HER2 complexes exist at the cell surface, with intracellular Nucleolin maintaining the HER2 receptors in a

dimerized, and constitutively activated state. The $F3_{wt}$NPs could indeed upregulate the ERK MAPK pathway via the Nucleolin/uPAR/α5β1-integrin/HER2 complex by binding directly to cell surface Nucleolin receptors. It is important to note that while the GAR (C-terminal) domain of surface Nucleolin interacts with uPAR, it would still be able to simultaneously bind the highly-basic $F3_{wt}$ peptide via its acidic N-terminal domain.[87] Despite the inhibitory effect of FAK on Cdc42, and consequently on the p38 and JNK MAPK pathway, the $F3_{wt}$NPs did activate the p38α, β and δ isoforms, as well as the JNK1-3 isoforms, above their respective basal levels in the untreated control. This is likely attributable to the possible association of surface-expressed Nucleolin with the transmembrane LRP-1 receptors,[88] such that the LRP-1 receptors are co-internalized with the Nucleolin-$F3_{wt}$NPs complexes from the cell surface. In turn, this could lead to activation of the p38 and JNK MAPKs that are associated with the cytoplasmic domain of LRP-1 via the JIP1/2 scaffold proteins.

Finally, given the clearly opposing p-ERK1/p-p38 signaling profiles elicited by the NTNPs and $F3_{wt}$NPs, it was rather interesting that the $F3_{wt}$ peptide elicited higher levels of both phosphorylated p-p38 (β and δ isoforms), and phosphorylated p-ERK1 than the $F3_{wt}$NPs (Fig. 4.3b). The more potent stimulation of p38β and p38δ phosphorylation by the $F3_{wt}$ peptide is likely due a combination of (i) co-activation of the LRP-1 receptors associated with surface-expressed Nucleolin, and (ii) less efficient recruitment of FAK to the regions of the cell membrane where the monovalent $F3_{wt}$ peptides bind to the Nucleolin/uPAR/α5β1-integrin/HER2 complexes. In contrast, it is plausible that a single, multivalent $F3_{wt}$NP would simultaneously engage multiple surface-expressed Nucleolin receptors, and in the process, assemble foci of multiple Nucleolin/uPAR/α5β1-integrin/HER2 complexes at the point of contact with the cell membrane. In turn, FAK would be more strongly recruited to that region of

surface-bound $F3_{wt}$NPs, than the surface-bound monovalent $F3_{wt}$ peptides, thus promoting deactivation of Cdc42 with subsequent suppression of p38 MAPK phosphorylation. The slightly higher levels of p-ERK1 elicited by the $F3_{wt}$ peptide is not surprising given the constitutively activated state in which the HER2 receptors are maintained by *cytoplasmically-localized Nucleolin*.[82]

4.3 Conclusion

In this study we demonstrate that the non-targeted PAA-NPs are more potent activators of the p38 MAPK pathway than the $F3_{wt}$-targeted PAA-NPs. It is well-documented that the p38 MAPKs phosphorylate and modulate the activity of key components of the endocytic machinery namely, EEA1 and Caveolin-1. We therefore present compelling evidence that the non-targeted PAA-NPs, and $F3_{wt}$-targeted PAA-NPs modulate their intracellular trafficking within nucleolin-overexpressing tumor cells, as previously reported by our group, via differential activation of the p38 MAPK pathway. Furthermore, our detailed phosphoproteomic analysis of key proteins in the ERK, JNK, p38 and Akt pathways revealed that the $F3_{wt}$ peptide, non-targeted PAA-NPs, and $F3_{wt}$-targeted PAA-NPs each elicit markedly different signaling profiles in MDA-MB-435 cells, which can either promote proliferation, or induce growth arrest of the tumor cells. In particular, it appears counter-intuitive to employ the $F3_{wt}$-targeted PAA-NPs as targeted nano-drug delivery system in the treatment of tumors, considering the proliferative MAPK signaling profile that they elicited. However, the $F3_{wt}$-targeted PAA-NPs may be particularly efficacious in activating dormant tumor stem cells that remain refractory to conventional chemotherapeutic drugs, and are responsible for establishing metastases. Therefore, a potentially viable approach to killing domant tumor stem cells is to activate them with the multivalent, $F3_{wt}$-targeted PAA-NPs, which

simultaneously deliver high concentrations of one, or more synergistic cytotoxic chemotherapeutic drugs directly into the tumor stem cell following endocytosis of the nanoparticle, thereby also circumventing the multi-drug resistance drug-efflux transporters located within the cell membrane. This may result in more efficient elimination of tumor stem cells with a concomitant reduction in the formation of secondary metastatic tumor sites, and thus improve the prognosis of cancer patients. We believe that our phosphoproteomic data provide compelling evidence that the design of tumor-targeting nanoparticle systems should also take into consideration the MAPK signaling profiles that they elicit on the intended target cell type, due to the profound influence that the p38 MAPKs, in particular, have on endocytic trafficking, as well as the survival status of the target tumor cell.

4.4 Experimental Section

Reagents and Materials

Acrylamide (AA), 3-(acryloyloxy)-2-hydroxypropylmethacrylate (AHM), ammonium persulfate (APS), *N,N,N`,N`*-tetramethylethylenediamine (TEMED), sodium dioctyl sulfosuccinate (AOT), Brij 30, L-cysteine, phosphate-buffered solution (PBS) tablets, disodium EDTA salt, sodium fluoride, sodium orthovanadate, sodium pyrophosphate, sodium azide, protease inhibitor cocktail (P8340), urea, Triton X-100, and Anisomycin were purchased from Sigma-Aldrich (St. Louis, MO). N-(3-aminopropyl)-methacrylamide hydrochloride (APMA) was purchased from Polysciences (Warrington, PA). Ethanol (100 %) and hexane were purchased from Fisher Scientific (Pittsburgh, PA). Heterobifunctional polyethyleneglycol (MAL–PEG–SCM, MW: 2,000 Da) was purchased from Creative PEG Works (Winston Salem, NC). The MDA-MB-435 human breast carcinoma cell line was obtained from American Type Culture Collection

(Manassas, VA, USA). Dulbecco's modified Eagle medium (DMEM), Hanks Balanced Salt Solution (HBSS; without Calcium/Magnesium), Gibco 0.25 % Trypsin-EDTA, Gibco 100x PenStrep-Glutamine and Gibco Heat-Inactivated Fetal Bovine Serum (HI-FBS) were purchased from Life Technologies (Carlsbad, CA). The Pierce Bicinchoninic Acid (BCA) Protein Assay Kit was purchased from Thermo Fisher Scientific Inc. (Rockford, IL). Probumin Bovine Serum Albumin (BSA) was purchased from EMD Millipore (Billerica, MA). Cysteine terminated wild-type F3 peptides ($F3_{wt}$-Cys: KDEPQRRSARLSAKPAPPKPEPKPKKAPAKKC) and scrambled F3 peptides ($F3_{scram}$-Cys: PKAARALPSQRSRPPEKAKKPPDKPAPEKKKC) were purchased from SynBioSci (Livermore, CA). The phospho-p38α (T180/Y182) DuoSet IC ELISA kit (DYC869-B), Human phospho-MAPK Array kit (ARY002B), Substrate Reagent Pack (H_2O_2 and Tetramethylbenzidine), and clear polystyrene plates were purchased from R&D Systems, and used according to the manufacturer protocol. Kodak BioMax MS X-Ray film was purchased from Fisher Scientific. All solutions were prepared in 18 MΩ water purified in a Barnstead 1 Thermolyne Nanopure II system. All reagents and materials were used as received without further purification.

Synthesis of amine surface-functionalized hydrogel polyacrylamide nanoparticles

A monomer mixture consisting of 711 mg acrylamide, 55 mg APMA, and 460 μL AHM were dissolved in PBS buffer (pH 7.4) and mixed together for 2 hours at room temperature. The mixture was emulsified in organic media containing surfactant (45 mL hexane, 1.6 g AOT, and 3.1 g Brij30) by continuous stirring for 20 minutes under Argon atmosphere in order to purge the reaction mixture of oxygen. Thereafter, polymerization was triggered by addition of radical initiator (100 μL of 10 % (w/v) ammonium persulfate in DI water and 100 μL of TEMED). The

reaction proceeded for 2 hours under mild argon purging and was terminated by exposing the reaction to normal atmosphere (radical quenching by atmospheric oxygen). The product was recovered through multiple separation steps: (i) removal of hexane by rotary evaporation, and (ii) multiple rinses with 100 % (v/v) ethanol to remove the surfactants, followed by multiple washes with DI water to remove residual surfactants using an Amicon stirred cell fitted with a 300 kDa molecular weight cut-off filter. The final product was lyophilized and kept frozen at -20 °C until use.

Surface functionalizations of PAA nanoparticles

Lyophilized PAA-NPs (50 mg) were dissolved in 2.5 mL PBS buffer (pH 7.4) and sonicated until the solution turned transparent, to which 4 mg heterobifunctional PEG (SCM-PEG-MAL) was then added and the mixture stirred continuously (~600 rpm) for 30 minutes at room temperature. The reaction between the succinimidyl ester group of the PEG crosslinker and the primary amine groups on the surface of PAA-NPs yielded maleimidyl ester-terminated PEG-conjugated PAA-NPs. Thereafter, the PEGylated PAA-NPs were washed three times with PBS buffer (pH 7.4) by centrifugation using an Amicon centrifugal filter (Millipore, 100 kDa molecular weight cut-off) at 5000*xg* for 20 min. After washing to remove unbound PEG crosslinkers, the surface PEGylated PAA-NPs were then reacted with either 11 mg wild-type F3-Cys peptide, or 11 mg scrambled F3-Cys peptide in PBS buffer (pH 7.4) and the conjugation reaction allowed to run overnight at room temperature under continuous stirring at ~600 rpm. The reaction between the thiol group of the carboxy terminal Cys residue of the $F3_{wt/scram}$ peptide moieties and the maleimidyl ester termini of the PEG crosslinkers facilitated covalent coupling of the $F3_{wt/scram}$ peptide moieties to the PEG crosslinkers already conjugated to the PAA-NP

surfaces. The $F3_{wt/scram}$ peptide functionalized PEGylated PAA-NPs were subsequently incubated with 1.74 mg L-cysteine under continuous stirring for 2 hours at room temperature to cap any unreacted maleimidyl ester groups so as to prevent their reaction with cell surface thiols. Thereafter, the $F3_{wt}$NPs/$F3_{scram}$NPs were washed five times with PBS (pH 7.4) using an Amicon centrifugal filter (100 kDa molecular weight cut-off) at 4000x*g* for 20 minutes and the final volume adjusted to 5 mL with PBS (pH 7.4). The final product was lyophilized and kept frozen at -20 °C until use. All steps were performed shielded from light.

Nanoparticle sizing and morphology

For all DLS sizing measurements, the lyophilized NPs were dissolved in DI water to a final concentration of 1 $mg.mL^{-1}$ and analyzed with a Beckman-Coulter Delsa Nano C particle analyzer. All measurements were performed in triplicate.

Nanoparticle zeta potential measurement

Zeta potential measurements of unmodified PAA-NPs (without PEG or F3 peptides), PEGylated PAA-NPs, and the $F3_{wt}$NPs/$F3_{scram}$NPs were performed in order to determine their respective surface charges. All zeta potential measurements were performed on 1 $mg.mL^{-1}$ solutions of each type of nanocarrier, prepared in DI water, using a Beckman-Coulter Delsa Nano C particle analyzer. All measurements were performed in triplicate.

Cell culture

MDA-MB-435 human breast adenocarcinoma cells were cultured aseptically at 37 °C under 5 % CO_2 humidified atmosphere in BD Falcon Primaria tissue culture dishes (100 mm x 20 mm). MDA-MB-435 cells were cultured in Dulbecco's Modified Eagle's Medium (DMEM) supplemented with 10 % (v/v) FBS and 1 % (v/v) penicillin-streptomycin-glutamine (PSG). Cell cultures were passaged during exponential growth phase by incubating the cells with 0.25 % Trypsin-EDTA solution at 37 °C until the cells attained rounded morphology, followed by resuspension of the detached cells in complete culture medium, and sub-culturing into new sterile culture dishes. The $F3_{wt}NP$, $F3_{scram}NP$ and unmodified PAA-NP suspensions were sterile filtered with a 0.2 μ syringe filter prior to use in all cell culture experiments.

Treatment of MDA-MB-435 cells for phospho-p38α ELISA

MDA-MB-435 cells were harvested by trysinisation with 0.25% Trypsin-EDTA solution at 37°C, and counted using a hemacytometer. Approximately $9x10^5$ cells were seeded into the required number of 100 mm x 20 mm culture dishes, and allowed to multiply over a period of 60 hours under standard culture conditions. Prior to the start of the experiment, stock solutions of the $F3_{wt}$ peptide, NTNPs, $F3_{wt}NPs$, and Anisomycin were prepared in complete culture medium and sonicated for 10 minutes to ensure complete dissolution. These stock solutions were then further diluted to their final working concentrations in complete culture medium as follows: $F3_{wt}$ peptide (0.22 mg/mL), NTNPs (1 mg/mL), $F3_{wt}NPs$ (1 mg/mL), and Anisomycin (10 μg/mL). The MDA-MB-435 cells were rinsed once with HBSS immediately before the start of the experiment. The dishes were replenished with culture medium up to a final volume of 5 mL containing either one of the above treatments at their respective working concentrations, or

culture medium without any treatment (untreated control). The cells were incubated with the above-mentioned treatments for the following periods: 15, 30, 60, 120 and 180 minutes under standard culture conditions. At the end of each treatment period, the culture media were immediately aspirated from each dish, the cells rinsed thoroughly with Calcium/Magnesium-free HBSS buffer, and rapidly detached with 1 mL 0.25% Trysin/EDTA solution. The cells were then resuspended in culture medium, and pelleted at 150x*g* for 5 minutes at 4 °C. The supernatants were discarded and the cell pellets immediately resuspended in ~500 μL ice-cold cell lysis buffer (1mM EDTA, 0.5% Triton X-100, 5 mM NaF, 6 M urea, 1 mM activated sodium orthovanadate, 2.5 mM sodium pyrophosphate, Sigma protease inhibitor cocktail P8340 (diluted 100-fold), in PBS pH 7.2-7.4) and kept on ice for 30 minutes. The lysates were then centrifuged at 2000 x*g* for 5 minutes at 4 °C to pellet cell debris. Protein concentrations of the supernatants were then determined by micro-BCA protein assay. The concentrations of the supernatants were then equilibrated to the lowest sample concentration in the batch, and further diluted 6-fold to reduce the urea concentration to 1 M. The supernatants were stored at -80 °C until further use. The treatment experiments were performed twice. The concentration of dual-phosphorylated (pT180/pY182) p38α MAPK in the equilibrated, 6-fold diluted samples was determined via the phospho-p38α MAPK ELISA according to the standard R&D Systems Inc. assay protocol. Each sample was assayed in triplicate, and the dual-phosphorylated (pT180/pY182) p38α MAPK concentration interpolated from a 2-fold, 8-point standard curve with a high concentration of 8000 pg/mL phosphorylated p38α MAPK protein. The ELISA assay was developed with a 1:1 mixture of H_2O_2 and Tetramethylbenzidine, and stopped with a 2N H2SO4 solution. The absorbance of the substrate was measured on a microplate reader at 450 nm with 550 nm wavelength correction.

Treatment of MDA-MB-435 cells for Human Phospho-MAPK Array Assay

Based on the results of the phospho-p38α ELISA, an optimal treatment period of 2 hours for the $F3_{wt}$ peptide, NTNPs and $F3_{wt}$NPs was identified. MDA-MB-435 cells were prepared as described for the phospho-p38α ELISA assay, and subjected to the above treatments, in addition to the $F3_{scram}$NPs (1 mg/mL) as a further control, for 2 hours under standard culture conditions. At the end of the 2 hour treatment period the culture dishes were immediately placed on ice, the culture medium aspirated, and ~400 μL of ice-cold array kit lysis buffer added to each dish. The cells were detached from the dishes into the lysis buffer using a rubber cell scraper. The cells were collected into 1.5 mL microfuge tubes and kept on ice for 30 minutes, after which the lysates were centrifuged at 14,000 x*g* for 5 minutes at 4 °C to pellet cell debris. Protein concentrations of the supernatants were then determined by micro-BCA protein assay. The concentrations of the supernatants were then equilibrated to the lowest sample concentration in the batch, and probed on the MAPK proteome profiler membranes according to the standard R&D Systems Inc. assay protocol. The membranes were developed with a chemiluminescent reagent provided with the MAPK proteome profiler kit, and the light signals generated were recorded on Kodak BioMax MS X-Ray films using an autoradiography cassette. Exposure times were typically between 5 and 10 minutes. The developed film was scanned at 800dpi resolution, and the individual spot intensities were measured using Image J v1.48 software.

Statistical Analyses

The endocytosis inhibition and colocalization data for each cell line were statistically analyzed by Student's t-test using GraphPad Prism v6.00 software for Mac OSX. All analyses were performed with a confidence interval set at 95 %. P-values <0.05 were considered significant.

References

1. J. Funkhouser, *Curr Drug Discov.*, 2002, **2**.
2. S. S. Kelkar and T. M. Reineke, *Bioconjug. Chem.*, 2011, **22**, 1879–903.
3. M. Hamidi, A. Azadi, and P. Rafiei, *Adv. Drug Deliv. Rev.*, 2008, **60**, 1638–49.
4. Y.-E. Koo Lee and R. Kopelman, in *Multifunctional Nanoparticles for Drug Delivery Applications: Imaging, Targeting, and Delivery*, eds. S. Svenson and R. K. Prud'homme, Springer US, Boston, MA, 2012, pp. 225–255.
5. J. Rejman, V. Oberle, I. S. Zuhorn, and D. Hoekstra, *Biochem. J.*, 2004, **377**, 159–69.
6. S. Zhang, J. Li, G. Lykotrafitis, G. Bao, and S. Suresh, *Adv. Mater.*, 2009, **21**, 419–424.
7. H. Yuan and S. Zhang, *Appl. Phys. Lett.*, 2010, **96**, 033704.
8. Y. Geng, P. Dalhaimer, S. Cai, R. Tsai, M. Tewari, T. Minko, and D. E. Discher, *Nat. Nanotechnol.*, 2007, **2**, 249–55.
9. J.-H. Park, G. von Maltzahn, L. Zhang, M. P. Schwartz, E. Ruoslahti, S. N. Bhatia, and M. J. Sailor, *Adv. Mater.*, 2008, **20**, 1630–1635.
10. X. Banquy, F. Suarez, A. Argaw, J.-M. Rabanel, P. Grutter, J.-F. Bouchard, P. Hildgen, and S. Giasson, *Soft Matter*, 2009, **5**, 3984–3991.
11. O. Harush-Frenkel, E. Rozentur, S. Benita, and Y. Altschuler, *Biomacromolecules*, 2008, **9**, 435–43.
12. O. P. Perumal, R. Inapagolla, S. Kannan, and R. M. Kannan, *Biomaterials*, 2008, **29**, 3469–3476.
13. Y. Zhang, M. Yang, J.-H. Park, J. Singelyn, H. Ma, M. J. Sailor, E. Ruoslahti, M. Ozkan, and C. Ozkan, *Small*, 2009, **5**, 1990–6.
14. L. Karamchand, G. Kim, S. Wang, H. J. Hah, A. Ray, R. Jiddou, Y.-E. Koo Lee, M. a Philbert, and R. Kopelman, *Nanoscale*, 2013, **5**, 10327–44.
15. H. Hillaireau and P. Couvreur, *Cell. Mol. Life Sci.*, 2009, **66**, 2873–96.
16. E. Ruoslahti, *Nat. Rev. Cancer*, 2002, **2**, 83–90.
17. E. Ruoslahti, S. N. Bhatia, and M. J. Sailor, *J. Cell Biol.*, 2010, **188**, 759–68.
18. G. Macé, M. Miaczynska, M. Zerial, and A. R. Nebreda, *EMBO J.*, 2005, **24**, 3235–46.
19. J. Callaghan, A. Simonsen, J. M. Gaullier, B. H. Toh, and H. Stenmark, *Biochem. J.*, 1999, **338 (Pt 2**, 539–43.
20. J. Rink, E. Ghigo, Y. Kalaidzidis, and M. Zerial, *Cell*, 2005, **122**, 735–49.
21. R. E. Harrison, C. Bucci, O. V Vieira, T. A. Schroer, and S. Grinstein, *Mol. Cell. Biol.*, 2003, **23**, 6494–506.
22. N. A. Bright, M. J. Gratian, and J. P. Luzio, *Curr. Biol.*, 2005, **15**, 360–5.
23. D. Volonté, F. Galbiati, R. G. Pestell, and M. P. Lisanti, *J. Biol. Chem.*, 2001, **276**, 8094–103.
24. L. Orlichenko, B. Huang, E. Krueger, and M. A. McNiven, *J. Biol. Chem.*, 2006, **281**, 4570–9.
25. F. Marano, S. Hussain, F. Rodrigues-Lima, A. Baeza-Squiban, and S. Boland, *Arch. Toxicol.*, 2011, **85**, 733–41.
26. J. Rauch, W. Kolch, S. Laurent, and M. Mahmoudi, *Chem. Rev.*, 2013, **113**, 3391–406.
27. G. Remy, A. M. Risco, F. a Iñesta-Vaquera, B. González-Terán, G. Sabio, R. J. Davis, and A. Cuenda, *Cell. Signal.*, 2010, **22**, 660–7.
28. M. Takekawa, T. Maeda, and H. Saito, *EMBO J.*, 1998, **17**, 4744–52.

29. M. Takekawa, M. Adachi, A. Nakahata, I. Nakayama, F. Itoh, H. Tsukuda, Y. Taya, and K. Imai, *EMBO J.*, 2000, **19**, 6517–26.
30. A. Cuenda and S. Rousseau, *Biochim. Biophys. Acta*, 2007, **1773**, 1358–75.
31. J.-L. Perfettini, M. Castedo, R. Nardacci, F. Ciccosanti, P. Boya, T. Roumier, N. Larochette, M. Piacentini, and G. Kroemer, *J. Exp. Med.*, 2005, **201**, 279–89.
32. J. Landry, H. Lambert, M. Zhou, J. N. Lavoie, E. Hickey, L. A. Weber, and C. W. Anderson, *J. Biol. Chem.*, 1992, **267**, 794–803.
33. L. Smeenk, S. J. van Heeringen, M. Koeppel, B. Gilbert, E. Janssen-Megens, H. G. Stunnenberg, and M. Lohrum, *PLoS One*, 2011, **6**, e17574.
34. J. M. Bruey, C. Ducasse, P. Bonniaud, L. Ravagnan, S. A. Susin, C. Diaz-Latoud, S. Gurbuxani, A. P. Arrigo, G. Kroemer, E. Solary, and C. Garrido, *Nat. Cell Biol.*, 2000, **2**, 645–52.
35. J. M. Bruey, C. Paul, a Fromentin, S. Hilpert, a P. Arrigo, E. Solary, and C. Garrido, *Oncogene*, 2000, **19**, 4855–63.
36. D. N. Dhanasekaran, K. Kashef, C. M. Lee, H. Xu, and E. P. Reddy, *Oncogene*, 2007, **26**, 3185–202.
37. T. Buschmann, O. Potapova, A. Bar-Shira, V. N. Ivanov, S. Y. Fuchs, S. Henderson, V. A. Fried, T. Minamoto, D. Alarcon-Vargas, M. R. Pincus, W. A. Gaarde, N. J. Holbrook, Y. Shiloh, and Z. Ronai, *Mol. Cell. Biol.*, 2001, **21**, 2743–54.
38. M. Deak, a D. Clifton, L. M. Lucocq, and D. R. Alessi, *EMBO J.*, 1998, **17**, 4426–41.
39. K. N. Dalby, N. Morrice, F. B. Caudwell, J. Avruch, and P. Cohen, *J. Biol. Chem.*, 1998, **273**, 1496–1505.
40. C. a Chrestensen and T. W. Sturgill, *J. Biol. Chem.*, 2002, **277**, 27733–41.
41. P. P. Roux and J. Blenis, *Microbiol. Mol. Biol. Rev.*, 2004, **68**, 320–44.
42. H. Vaidyanathan, J. Opoku-Ansah, S. Pastorino, H. Renganathan, M. L. Matter, and J. W. Ramos, *Proc. Natl. Acad. Sci. U. S. A.*, 2007, **104**, 19837–42.
43. G. R. Wiggin, A. Soloaga, J. M. Foster, V. Murray-Tait, P. Cohen, and J. S. C. Arthur, *Mol. Cell. Biol.*, 2002, **22**, 2871–81.
44. J. Xing, D. D. Ginty, and M. E. Greenberg, *Science*, 1996, **273**, 959–63.
45. K. Du and M. Montminy, *J. Biol. Chem.*, 1998, **273**, 32377–9.
46. B. Mayr and M. Montminy, *Nat. Rev. Mol. Cell Biol.*, 2001, **2**, 599–609.
47. B. E. Wadzinski, W. H. Wheat, S. Jaspers, L. F. Peruski, R. L. Lickteig, G. L. Johnson, and D. J. Klemm, *Mol. Cell. Biol.*, 1993, **13**, 2822–34.
48. M. R. Junttila, S.-P. Li, and J. Westermarck, *FASEB J.*, 2008, **22**, 954–65.
49. D. P. Brazil and B. A. Hemmings, *Trends Biochem. Sci.*, 2001, **26**, 657–64.
50. G. Song, G. Ouyang, and S. Bao, *J. Cell. Mol. Med.*, 2005, **9**, 59–71.
51. D. A. Cross, D. R. Alessi, P. Cohen, M. Andjelkovich, and B. A. Hemmings, *Nature*, 1995, **378**, 785–9.
52. A. Sekulić, C. C. Hudson, J. L. Homme, P. Yin, D. M. Otterness, L. M. Karnitz, and R. T. Abraham, *Cancer Res.*, 2000, **60**, 3504–13.
53. C. Sutherland, I. A. Leighton, and P. Cohen, *Biochem. J.*, 1993, **296 (Pt 1)**, 15–9.
54. C. Sutherland and P. Cohen, *FEBS Lett.*, 1994, **338**, 37–42.
55. B. T. Navé, M. Ouwens, D. J. Withers, D. R. Alessi, and P. R. Shepherd, *Biochem. J.*, 1999, **344 Pt 2**, 427–31.
56. G. G. Chiang and R. T. Abraham, *J. Biol. Chem.*, 2005, **280**, 25485–90.
57. M. K. Holz and J. Blenis, *J. Biol. Chem.*, 2005, **280**, 26089–93.

58. M. Rosner, N. Siegel, A. Valli, C. Fuchs, and M. Hengstschläger, *Amino Acids*, 2010, **38**, 223–8.
59. N. Pullen and G. Thomas, *FEBS Lett.*, 1997, **410**, 78–82.
60. T. R. Fenton and I. T. Gout, *Int. J. Biochem. Cell Biol.*, 2011, **43**, 47–59.
61. Z. Xia, M. Dickens, J. Raingeaud, R. J. Davis, and M. E. Greenberg, *Science*, 1995, **270**, 1326–31.
62. A. C. Ranganathan, A. P. Adam, and J. A. Aguirre-Ghiso, *Cell Cycle*, 2006, **5**, 1799–807.
63. M. S. Sosa, A. Avivar-Valderas, P. Bragado, H.-C. Wen, and J. A. Aguirre-Ghiso, *Clin. Cancer Res.*, 2011, **17**, 5850–7.
64. A. P. Lillis, L. B. Van Duyn, J. E. Murphy-Ullrich, and D. K. Strickland, *Physiol. Rev.*, 2008, **88**, 887–918.
65. J. Westermarck, S. P. Li, T. Kallunki, J. Han, and V. M. Kähäri, *Mol. Cell. Biol.*, 2001, **21**, 2373–83.
66. E. J. Black, M. Walker, W. Clark, A. MacLaren, and D. A. F. Gillespie, *Oncogene*, 2002, **21**, 6540–8.
67. S. Ugi, T. Imamura, W. Ricketts, and J. M. Olefsky, *Mol. Cell. Biol.*, 2002, **22**, 2375–87.
68. E. Sontag, S. Fedorov, C. Kamibayashi, D. Robbins, M. Cobb, and M. Mumby, *Cell*, 1993, **75**, 887–97.
69. S. Grethe and M. I. Pörn-Ares, *Cell. Signal.*, 2006, **18**, 531–40.
70. T. Cedervall, I. Lynch, M. Foy, T. Berggård, S. C. Donnelly, G. Cagney, S. Linse, and K. a Dawson, *Angew. Chem. Int. Ed. Engl.*, 2007, **46**, 5754–6.
71. T. Cedervall, I. Lynch, S. Lindman, T. Berggård, E. Thulin, H. Nilsson, K. a Dawson, and S. Linse, *Proc. Natl. Acad. Sci. U. S. A.*, 2007, **104**, 2050–5.
72. X. Zheng, H. Baker, W. S. Hancock, F. Fawaz, M. McCaman, and E. Pungor, *Biotechnol. Prog.*, 2006, **22**, 1294–300.
73. C. C. Fleischer and C. K. Payne, *J. Phys. Chem. B*, 2014.
74. J. A. Aguirre Ghiso, D. Liu, A. Mignatti, K. Kovalski, and L. Ossowski, *Mol. Biol. Cell*, 2001, **12**, 863–79.
75. D. Liu, J. Aguirre Ghiso, Y. Estrada, and L. Ossowski, *Cancer Cell*, 2002, **1**, 445–57.
76. J. A. Aguirre Ghiso, *Oncogene*, 2002, **21**, 2513–24.
77. S. Bagrodia, B. Dérijard, R. J. Davis, and R. A. Cerione, *J. Biol. Chem.*, 1995, **270**, 27995–8.
78. J. D. Hildebrand, J. M. Taylor, and J. T. Parsons, *Mol. Cell. Biol.*, 1996, **16**, 3169–78.
79. N. Song, Y. Ding, W. Zhuo, T. He, Z. Fu, Y. Chen, X. Song, Y. Fu, and Y. Luo, *Angiogenesis*, 2012, **15**, 697–711.
80. Y. Wei, R.-P. Czekay, L. Robillard, M. C. Kugler, F. Zhang, K. K. Kim, J.-P. Xiong, M. J. Humphries, and H. a Chapman, *J. Cell Biol.*, 2005, **168**, 501–11.
81. K. Farin, A. Di Segni, A. Mor, and R. Pinkas-Kramarski, *PLoS One*, 2009, **4**, e6128.
82. A. Di Segni, K. Farin, and R. Pinkas-Kramarski, *PLoS One*, 2008, **3**, e2310.
83. K. Subik, J.-F. Lee, L. Baxter, T. Strzepek, D. Costello, P. Crowley, L. Xing, M. Hung, T. Bonfiglio, D. G. Hicks, and P. Tang, *Breast Cancer (Auckl).*, 2010, **4**, 35–41.
84. F. Schaffner, A. M. Ray, and M. Dontenwill, *Cancers (Basel).*, 2013, **5**, 27–47.
85. S. Christian, J. Pilch, M. E. Akerman, K. Porkka, P. Laakkonen, and E. Ruoslahti, *J. Cell Biol.*, 2003, **163**, 871–8.
86. A. M. LeBeau, S. Duriseti, S. T. Murphy, F. Pepin, B. Hann, J. W. Gray, H. F. VanBrocklin, and C. S. Craik, *Cancer Res.*, 2013, **73**, 2070–81.

87. H. Ginisty, H. Sicard, B. Roger, and P. Bouvet, *J. Cell Sci.*, 1999, **112 (Pt 6)**, 761–72.
88. B. Krust, D. El Khoury, I. Nondier, C. Soundaramourty, and A. G. Hovanessian, *BMC Cancer*, 2011, **11**, 333.

Appendix

A4.1 Hydrodynamic size and Zeta Potential (surface charge) characterizations of the NTNPs, F3NP$_{wt}$ and F3NP$_{scram}$

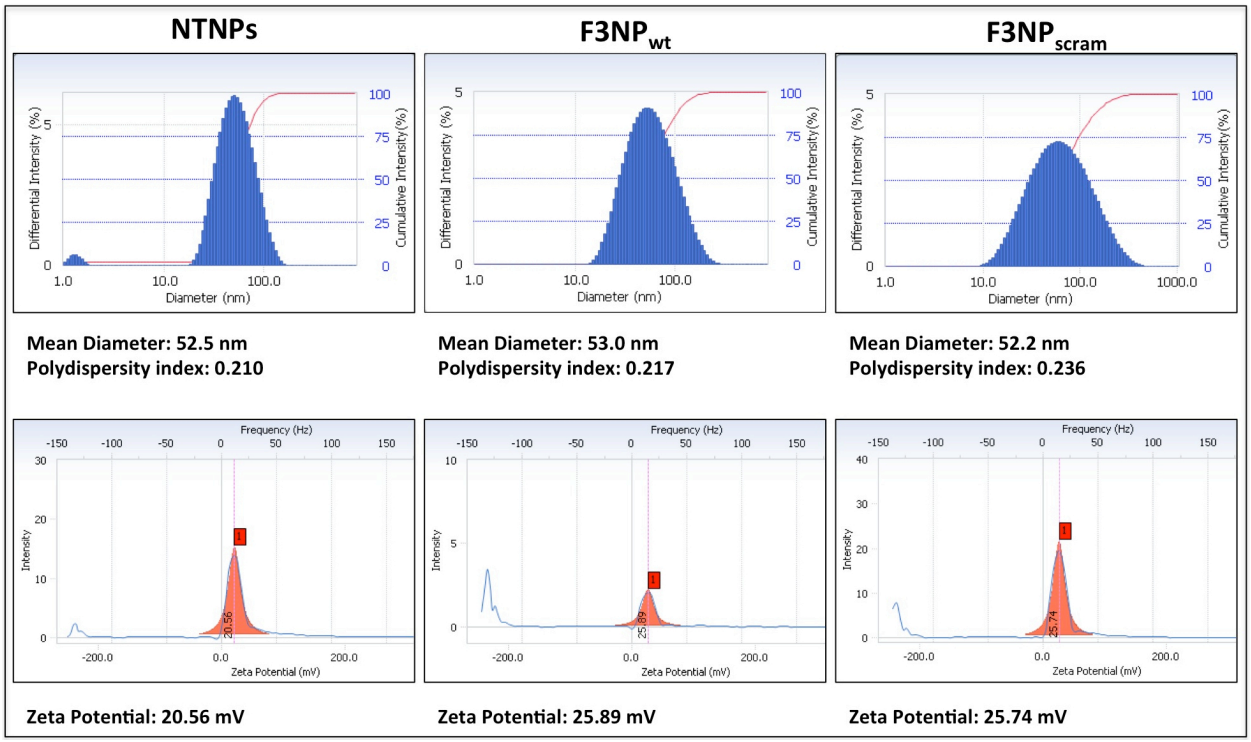

Fig. A4.1 Hydrodynamic diameters (above) of the NTNPs, F3$_{wt}$NP and F3$_{scram}$NP as determined by dynamic light scattering based on 1 mg/mL suspensions of the respective NPs prepared in 10 mM phosphate buffered saline (PBS, pH 7.2). Zeta potentials (below) of the NTNPs, F3NP$_{wt}$ and F3NP$_{scram}$ based on 1 mg/mL suspensions of the respective NPs prepared in dH_2O.

A4.2 Raw data of phosphoproteomic MAPK Arrays obtained for the Untreated Control, $F3_{wt}$ Peptide, NTNPs, $F3_{wt}$NP, and $F3_{scram}$NP treatments of MDA-MB-435 cells

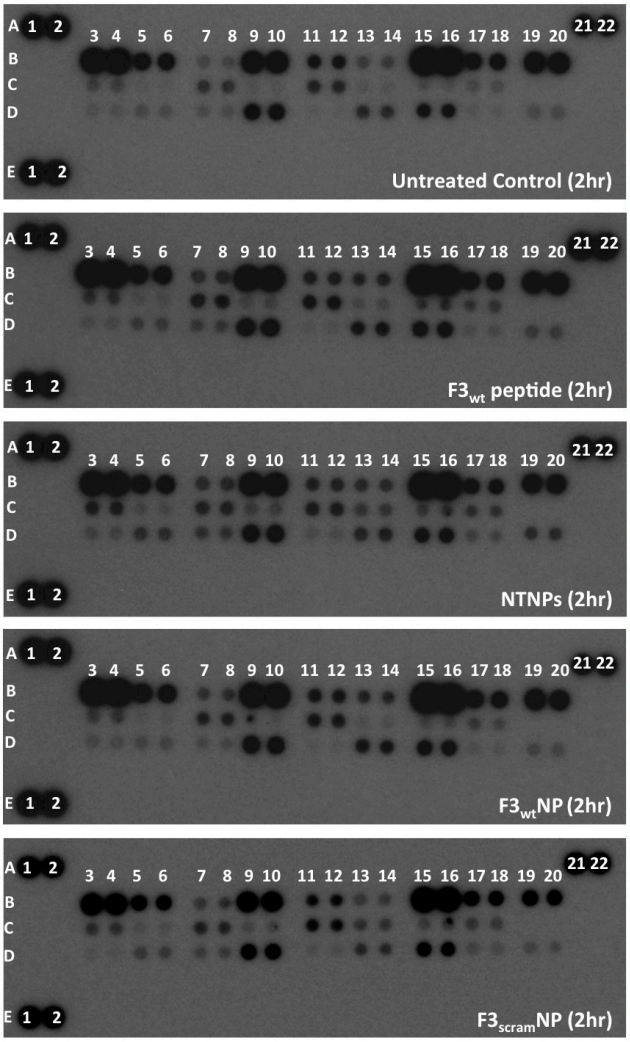

Coordinate	Target	Phosphorylation Site Detected
A1, A2	***Positive Control***	-
A21, A22	***Positive Control***	-
B3, B4	Akt1	S473
B5, B6	Akt2	S474
B7, B8	Akt3	S472
B9, B10	Akt pan	S473, S474, S472
B11, B12	CREB	S133
B13, B14	ERK1	T202/Y204
B15, B16	ERK2	T185/Y187
B17, B18	GSK-3α/β	S21/S9
B19, B20	GSK-3β	S9
C3, C4	Hsp27	S78/S82
C5, C6	JNK1	T183/Y185
C7, C8	JNK2	T183/Y185
C9, C10	JNK3	T221/Y223
C11, C12	JNK pan	T183/Y185, T221/Y223
C13, C14	MKK3	S218/T222
C15, C16	MKK6	S207/T211
C17, C18	MSK2	S360
D3, D4	p38α	T180/Y182
D5, D6	p38β	T180/Y182
D7, D8	p38δ	T180/Y182
D9, D10	p38γ	T183/Y185
D11, D12	p53	S46
D13, D14	p70 S6 Kinase	T421/S424
D15, D16	RSK1	S380
D17, 18	RSK2	S386
D19, D20	TOR	S2448
E1, E2	***Positive Control***	-

Fig. A4.2 Images of phosphoproteomic MAPK membrane arrays developed by chemiluminescence using Kodak Biomax MS autoradiography films following probing with whole cell lysates of untreated MDA-MB-435 cells, or MDA-MB-435 cells treated with $F3_{wt}$ Peptide (0.22 mg/mL), NTNPs (1 mg/mL), $F3_{wt}$NP (1 mg/mL), or $F3_{scram}$NP (1 mg/mL) for 2 hours at 37 °C, 5% CO_2 humidified atmosphere.

A4.3 Fold changes in the levels of phosphorylated proteins in response to the various treatments relative to the untreated control MDA-MB-435 cell

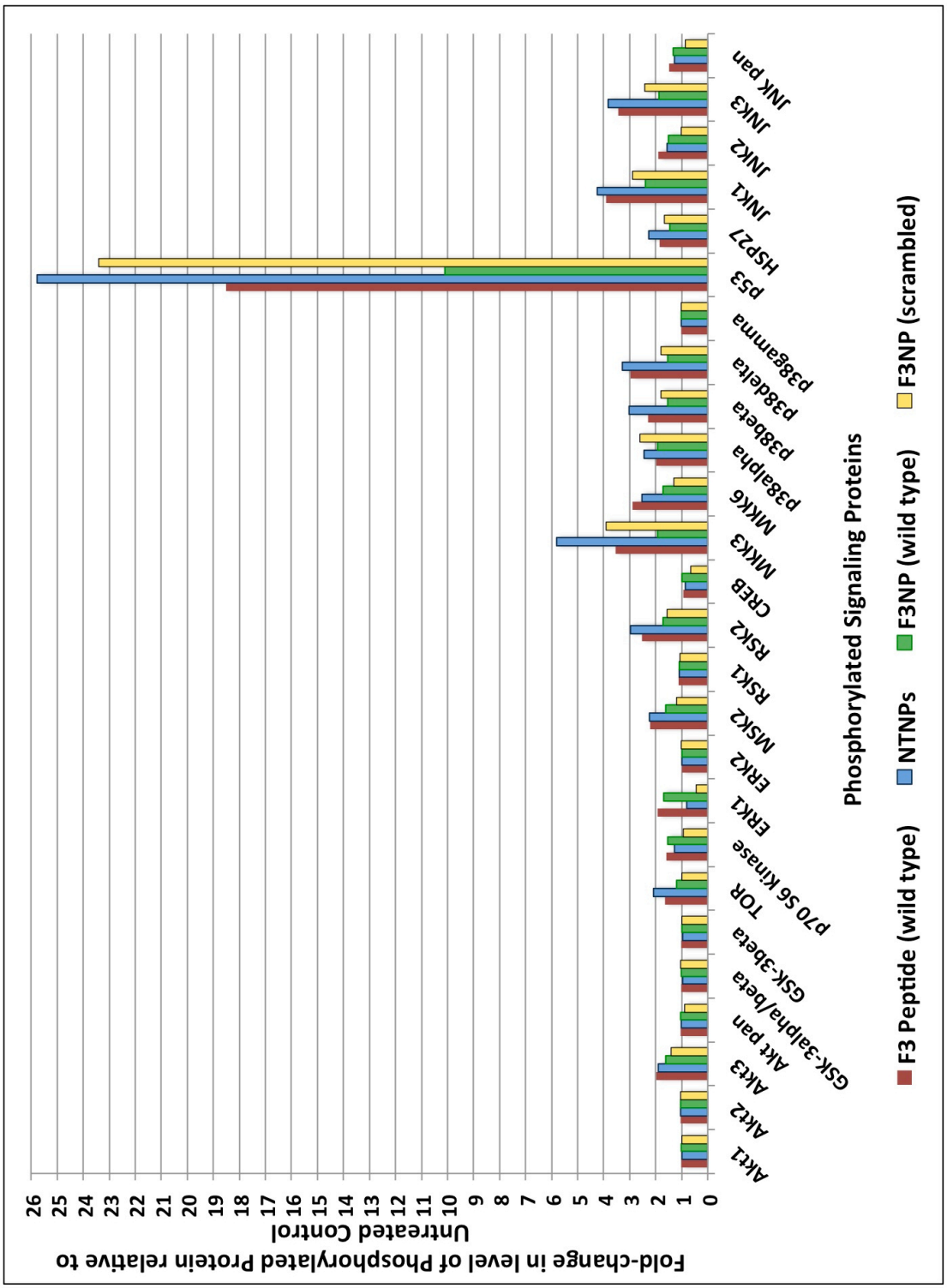

Fig. A4.3.1 Column chart depicting fold increases and decreases in the levels of phosphorylated signaling proteins determined by the phosphoproteomic arrays (Fig. A4.2) in response to the various treatments relative to the untreated control MDA-MB-435 cells.

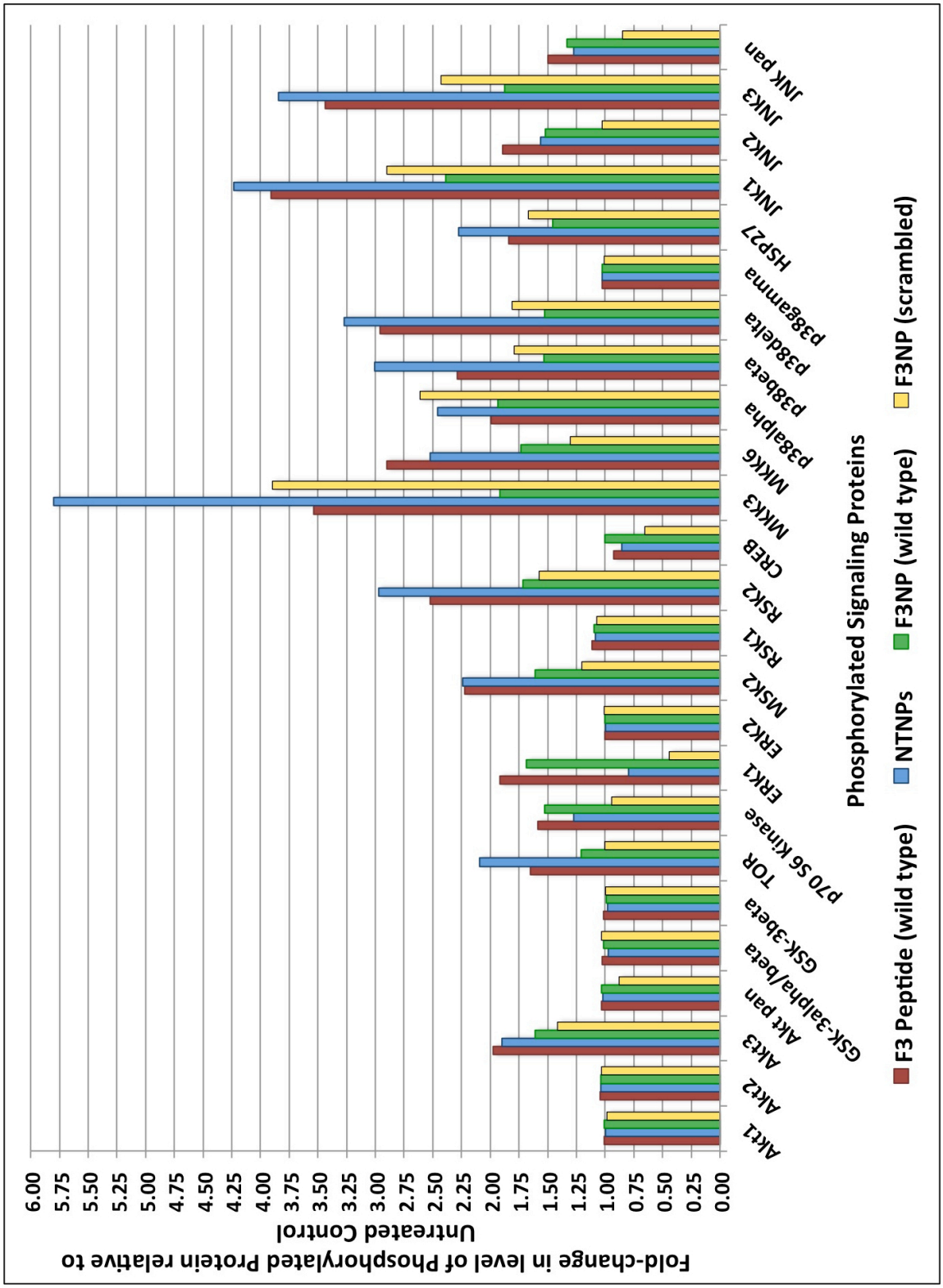

Fig. A4.3.2 Column chart depicting fold increases and decreases in the levels of phosphorylated signaling proteins determined by the phosphoproteomic arrays (Fig. A4.2) in response to the various treatments relative to the untreated control MDA-MB-435 cells. The values for phosphorylated p53 have been omitted to present the fold changes in phosphorylation levels of the other signaling proteins more clearly.

A4.4 Linear correlation strengths between phosphorylated MAP2K (MKK3/MKK6) levels and phosphorylated p38 MAPK levels

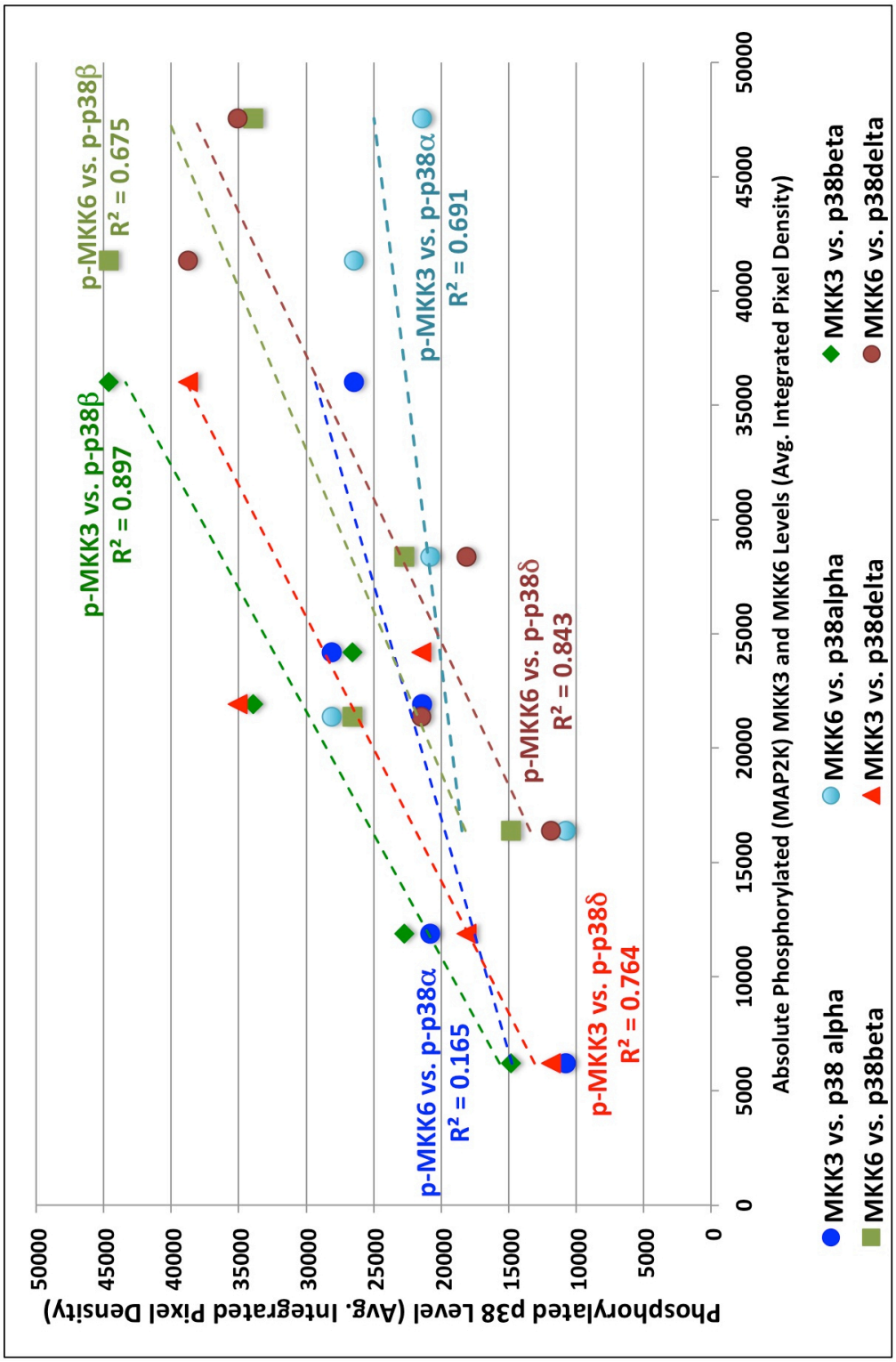

Fig. A4.4.1 Linear correlation strengths between the levels of phosphorylated MKK3 (MAP2K), phosphorylated MKK6 (MAP2K) and the levels of phosphorylated p38α, p38β and p38δ MAPKs. Data points for each curve were obtained from the untreated control, $F3_{wt}$ peptide, NTNPs, $F3_{wt}$NP and $F3_{scram}$NP treatments (2 hours post-delivery).

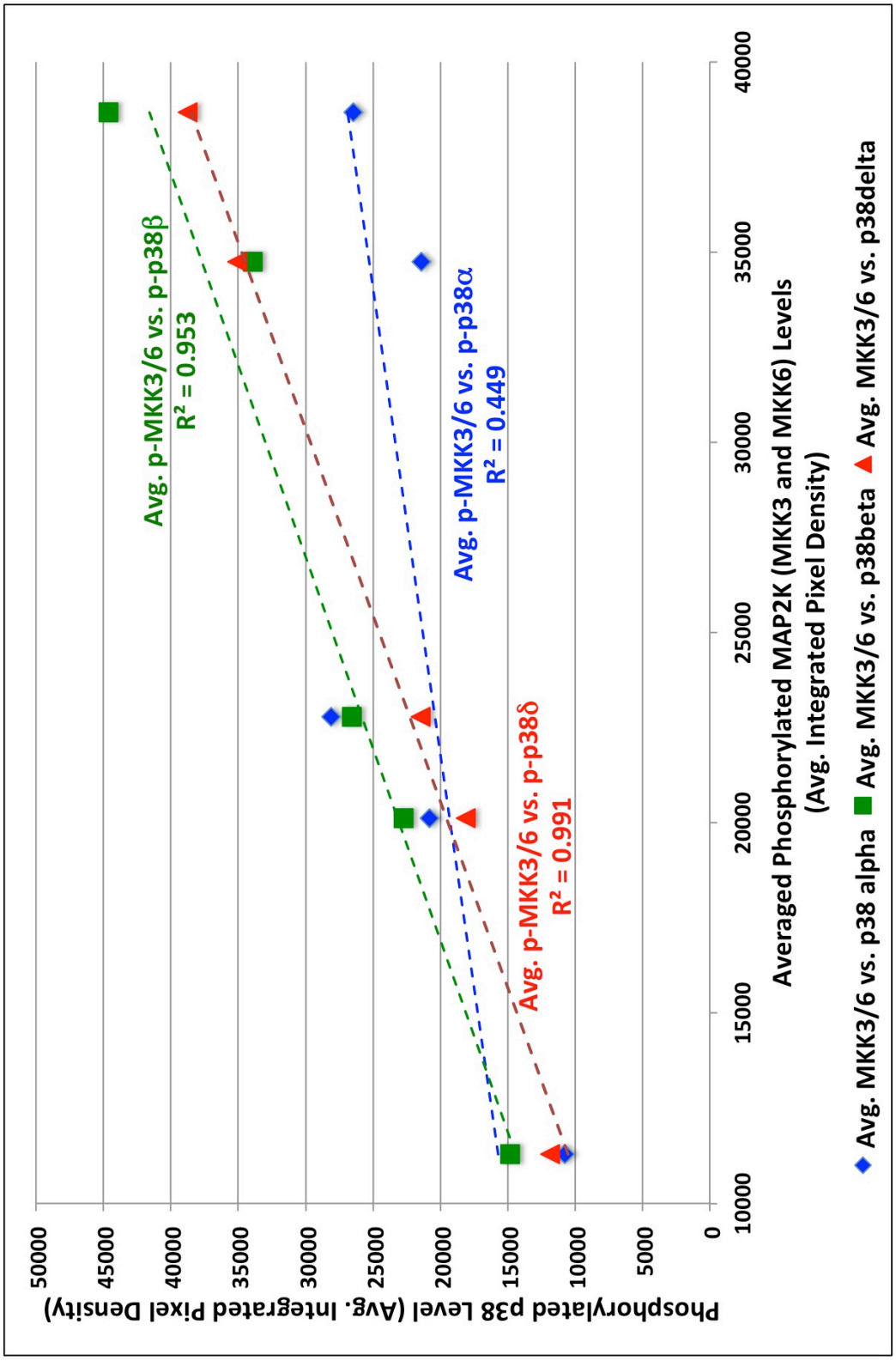

Fig. A4.4.2 Correlations between the levels of average MAP2K (MKK3 and MKK6) and the levels of phosphorylated p38α, p38β and p38δ MAPKs. Data points for each curve were obtained from the untreated control, $F3_{wt}$ peptide, NTNPs, $F3_{wt}$NP and $F3_{scram}$NP treatments (2 hours post-delivery).

Chapter 5

Future Directions

5.1 Long-term intracellular trafficking studies

The intracellular trafficking study in Chapter 3 revealed that while the NTNPs exhibited a time-dependent increase in colocalization with LAMP1 protein (reminiscent of accumulation within lysosomes), this was not the case for the F3NPs. Instead, we observed distinct F3NP-laden endosomes within the perinuclear space that were devoid of LAMP1 proteins. Future studies will focus on determining the precise identity of the subcellular compartments within which the F3NPs are contained. Possible compartments include the Golgi network, and the endoplasmic reticulum. The presence of the Rab7 GTPase on endosomal membranes is known to ensure their delivery to lysosomes, whereas Rab9 GTPase mediates the trafficking of late endosomes to the Golgi network.[1] Hence, one possible experiment is to employ fluorescent Rab7, and Rab9 constructs, and chase the intracellular trafficking of the F3NPs relative to these GTPase proteins. Furthermore, immunocytochemistry studies beyond 6 hours are necessary to determine the subcellular localization of the F3NPs over long periods of time, as this has important implications for *in vivo* drug delivery. In addition, the F3-targeted NPs employed in this study were based on a surface ligand (F3 peptide) density that elicited saturated cellular sequestrations (binding and uptake) characteristics in both the 9L and MDA-MB-435 cell lines. Future studies

will focus on determining the minimum surface ligand (F3 peptide) density necessary to yield the multivalency effect, and thus confer lysosome-evasive properties to the F3NPs.

The pentavalent HB-19 pseudopeptide, a specific antagonist that binds the C-terminal tail of nucleolin,[2] was shown to suppress the growth of tumor cells and angiogenesis. It will also be interesting to investigate how this multivalent HB-19 pseudopeptide influences the intracellular trafficking of the PAA-NPs, relative to the F3-targeted PAA-NPs.

5.2 MAPK cell signaling studies

Based on our observations from the p38 ELISA and phosphoproteomic arrays, the NTNPs, as well as the F3 peptide alone, elicited significantly higher levels of phosphorylated p38β and p38δ MAPK isoforms than the $F3_{wt}$NPs. Given that the p38 MAPKs directly phosphorylate EEA1 and caveolin1, this observation provides a signaling mechanism to explain the differential intracellular trafficking of the NTNPs and $F3_{wt}$NPs. Future studies will focus on confirming if the NTNPs do indeed elicit greater phosphorylation of EEA1 at Thr-1392, and Caveolin-1 at Tyr-14 than the F3NPs. If this is indeed the case, then subsequent experiments will seek to determine which p38 MAPK isoform is responsible for mediating the phosphorylation of EEA1 and Caveolin-1 through the use of selective inhibitors.

With respect to the JNK pathway, future studies will focus on determining the phosphorylation status of the MAP2K enzymes, MKK4 and MKK7 that directly phosphorylate JNK1-3, so as to gain a better understanding of the JNK1-3 phosphorylation profiles we observed in this study. Furthermore, the phosphorylation status of p53 tumor suppressor protein at Thr-81 will also be determined. This is necessary to elucidate if the p38 and JNK MAPKs are indeed acting synergistically to induce growth arrest in response to the NTNPs and $F3_{scram}$NPs.

With respect to the ERK pathway, studies of the phosphorylation status of the N-terminal and C-terminal domains of RSK1 and RSK2 will also be performed. This is necessary to determine (i) the level of direct phosphorylation elicited by ERK1/2 at the C-terminal domains of RSK1/2, and (ii) if that translates into similar levels of phosphorylation at the N-terminal domains of RSK1/2. Ultimately, this will provide a holistic understanding of the activation status of the RSK1 and RSK2 proteins in response to activation of the ERK pathway by the F3 peptide and $F3_{wt}$NPs. Similar studies will be performed to with respect to the Akt1-3 isoforms, as well as p70S6k, so as to determine the actual activation status of these proteins in response to the various treatments, and thus the implications they have for cell survival.

In addition, the differential p-ERK/p-p38 ratios elicited by the various treatments were remarkable observations. It is therefore necessary to determine if the p-ERK^{high}/ p-$p38^{low}$ signaling ratio elicited by the $F3_{wt}$NPs translate into cellular proliferation, and if the p-ERK^{low}/p-$p38^{high}$ signaling ratios elicited by the NTNPs and $F3_{scram}$NPs translate into apoptosis. This will be confirmed by performing extended duration treatments with the various NPs and $F3_{wt}$ peptides, followed cellular proliferation and apoptosis assays.

Last, with respect to the NTNPs interactions with cell surface receptors, we also aim to characterize the composition of the protein corona that forms around the positively charged NTNPs, and further determine the protein-receptor interactions that mediate the internalization of the NTNPs. Moreoever, we will also determine if the treatment of MDA-MB-435 cells with the $F3_{wt}$NP translates into stronger recruitment of FAK to the sites of binding, than with the $F3_{wt}$ peptides alone.

References

1. P. Barbero, L. Bittova, and S. R. Pfeffer, *J. Cell Biol.*, 2002, **156**, 511–8.

2. D. Destouches, D. El Khoury, Y. Hamma-Kourbali, B. Krust, P. Albanese, P. Katsoris, G. Guichard, J. P. Briand, J. Courty, and A. G. Hovanessian, *PLoS One*, 2008, **3**, e2518.